NORTHWESTERN UNIVERSITY

Plasmonic Lattice Metasurfaces by Predictive Computational Design

A DISSERTATION

SUBMITTED TO THE GRADUATE SCHOOL
IN PARTIAL FULFILLMENT OF THE REQUIREMENTS

for the degree

DOCTOR OF PHILOSOPHY

Field of Materials Science and Engineering

By

Jingtian Hu

EVANSTON, ILLINOIS

March 2019

ABSTRACT

Plasmonic Lattice Metasurfaces by Predictive Computational Design

Jingtian Hu

Plasmonic metasurfaces are leading the development of next-generation optical devices with unprecedented compactness and functionality. In contrast to bulk refractive optics, these planar surfaces manipulate light with rationally designed subwavelength building blocks. This thesis focus on how emerging materials and design methods advance the field of metasurfaces. Chapter 1 reviews the existing metasurfaces based on noble metals and their design by wave-optics principles. This chapter also introduces our metasurface design strategy by evolutionary algorithms, which achieved a wide range of optical responses simply by tuning the arrangement of a single gold nanohole on a discrete square lattice.

Chapter 2 describes the realization of metasurfaces based on subwavelength hole arrays in films of single-crystalline titanium nitride, an unconventional plasmonic material that exhibits superb mechanical strength and high-temperature stability. A multiobjective fitness function was developed for our evolutioanry algorithm to produce a variety of three-dimensional light profiles with controllable intensities at the light spots. I also demonstrate a simple, efficient technique to prototype these optical designs in large-area by combining focused ion beam milling and wet chemical etching.

Chapter 3 applies the evolutionary approach to design achromatic metalenses based on subwavelength plasmonic nanoparticles. Lattice metalenses consisting of a single type of nanoparticle could operate at any wavelengths in the visible to near-infrared regime by tailoring the surface plasmon resonance. The algorithm realized efficient multiobjective optimization and produced achromatic lenses at up to three wavelengths using multiple different nanoparticle shapes.

Chapter 4 demonstrates a reconfigurable metalens system for visible-range imaging based on arrays of coupled plasmonic nanoparticles. These lenses manipulated the wavefront and focused light exciting surface lattice resonances that were tuned by patterned polymer blocks on single-particle sites. Predictive design of the dielectric nano-blocks by our evolutionary algorithm created a range of three-dimensional focusing responses. I developed a simple and scalable technique for erasing and writing the polymer nanostructures in a single step using nanoscale embossing. This reconfigurable materials platform enables tunable focusing and offers prospects for highly adaptive compact-imaging.

Acknowledgements

I would first like to express my greatest gratitude toward Professor Teri W. Odom for advising me in the past five years. As a passionate, creative, and diligent scientist, she has been always the example I want to learn from. As an advisor, she is critical, rigorous but always supportive to every student and grants me tremendous freedom in pursuing new research projects. She is the mentor who introduced me to the field of nanophotonics and help me along the way towards becoming an independent researcher.

I want to thank Dr. Mark Huntington whose guidance is vital to my thesis work. I appreciate former and current members of the Odom group for maintaining a positive research atmosphere around me. I would also like to acknowledge my thesis committee members Professor Chris Wolverton, Professor Lincoln Lauhon, and Professor Wei Chen for dedicating their time to reviewing my thesis and defense.

I would like to acknowledge the collaborators in all my projects for their constructive input. I would also like to thank the research facilities at Northwestern, including NUFAB, EPiC, and Keck-II that fortuitously come together to enable top-class research. I want to thank the department administrators, especially Lindsay Haukebo, who have provided endless support throughout my graduate career.

Lastly, and most importantly, I want to thank my family for their love and support throughout the past 27 years and on into the future. In the hardest years of my life when everyone questioned my ability, my parents always trust me and constantly encouraged me to tackle all the challenges with an optimistic attitude. They also supported me financially to study abroad for the world-class academic environment.

List of abbreviations

AFM atomic force microscopy

Ag silver

Al aluminum

ALD atomic layer deposition

Au gold

CCD charge coupled device

Cr chromium

DRIE deep reactive ion etching

EBL electron beam lithography

FDTD finite-difference time-domain

FIB focused-ion beam

FWHM full-width at half-maximum

LEA Lattice evolution algorithm

LSP localized surface plasmon

NA numerical aperture

NIR near-infrared

NP nanoparticle

PDMS polydimethyl siloxane

PEEL photolithography, etching, e-beam deposition, and lift-off

PMMA polymethyl methacrylate

SANE solvent-assisted nanoscale embossing

SEM scanning electron microscopy

Si	silicon
SLR	surface lattice resonances
SPP	surface plasmon polariton
TE	transverse electric
TiN	titanium nitride
TiO_2	titanium dioxide
TM	transverse magnetic
UV	ultraviolet
2D	two-dimensional
3D	three-dimensional

Table of Contents

List of Tables

List of Figures

CHAPTER 1

Introduction to Optical Metasurfaces

This chapter introduces the concept of optical metasurface and reviews how optical components evolve from traditional bulk optics to the early diffractive optics and eventually to the planar metamaterials. I will discuss the physics and design principles of existing metasurface devices based on electrodynamics and wave optics as well as the major challenges in the design, fabrication, and materials perspectives. Lastly, our previous work on designing metasurfaces with a computational method based on the genetic algorithm will be introduced. This heuristic approach can solve for a range of complex optical by tailoring the arrangement of a simple lattice units – a nanohole, for example – on a square grid, and will be used and further developed in later chapters.

1.1. Miniaturization of Optical Devices

Compact optical elements are becoming important in realizing portable devices ranging from thin camera lenses to miniaturized microscopes. Conventional optical devices including eye-glasses, cameras, and beam splitters consist of refractive elements such as lenses and prisms. The processing technology of these optical components, however, are typically restricted to millimeter scale and cannot achieve ultrathin architectures similar to the Si-based electronics devices. For applications where small size and light weight are required, earlier researchers developed diffractive optics, which achieved a remarkable reduction in thickness but also have complex three-dimensional (3D) features that increased fabrication difficulty and cost tremendously. By exploiting the wave-optics principles at the subwavelength scale, optical metasurfaces have been developed to have not only sub-micron thickness, but also planar device designs that enables simple fabrication based on nanoscale lithography procedures developed in the Si industry.

1.1.1. Wave-optics theories in refractive optics

In classical formulations, light is represented by a wave that propagates in both vacuum and dielectric media in the direction orthogonal to the oscillations of electric and magnetic field components.[1] Light propagation can be described by the differential equation which I refer to as the wave equation:[1]

$$\nabla^2 u - \frac{1}{c^2}\frac{\partial^2 u}{\partial t^2} = 0 \tag{1.1}$$

where $\nabla^2 = \frac{\partial^2}{\partial x^2} + \frac{\partial^2}{\partial y^2} + \frac{\partial^2}{\partial z^2}$ is the Laplacian operator, $u = u(\boldsymbol{r}, t)$ is the wave equation, $\boldsymbol{r}$ is the position vector, t is time, and c is the speed of light which, in a medium with refractive index n, is defined as:[2]

$$c = \frac{c_0}{n} \tag{1.2}$$

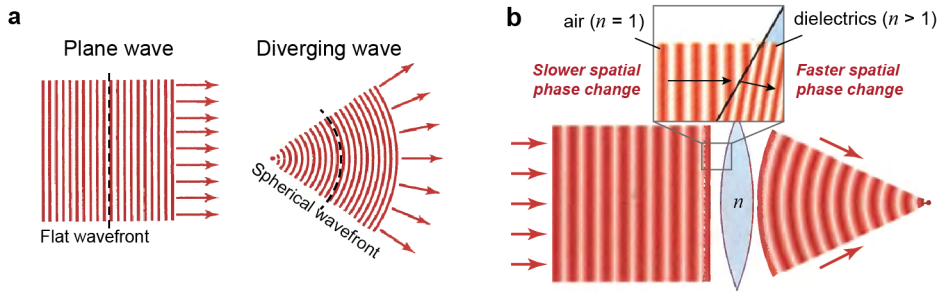

Figure 1.1. Manipulate light flow by wavefront engineering. (**a**) Light rays propagate in the orthogonal direction of the wavefront surfaces. (**b**) Refractive lenses produce a paraboloidal wavefront to focus light by the gradual phase delays accumulated while propagating in a medium with higher index than air ($n = 1$). Figure reproduced from Saleh and Teich.[1,2]

where c_0 is the speed of light in vacuum. The solutions to the wave equation (Equation 1.1) can be expressed generally as a complex function:[1]

$$u(\boldsymbol{r}, t) = \alpha(\boldsymbol{r})\exp(j\omega t)\exp(j\phi(\boldsymbol{r})) \tag{1.3}$$

where α is the amplitude, ω is the angular frequency, and ϕ is the phase of the wave in the range $0-2\pi$. At a given time t, the amplitude of the light wave is a function of the position vector $u(\boldsymbol{r}) = \alpha(\boldsymbol{r})\exp(j\phi(\boldsymbol{r}))$ and the surfaces of equal phase (solutions to $\phi(\boldsymbol{r}) = \text{constant}$) are referred to as the **wavefront**. Light always propagates in the direction of wavefront normal $\nabla\phi(\boldsymbol{r})$. **Figure 1.1a** shows schematically two examples of light waves where the plane wave has wavefronts consisting of uniform, infinite surfaces, while the converging/diverging beam exhibits spherical wavefronts.

Refractive optical components including lenses and prisms control the light propagation by tuning the wavefront phases of the optical rays that pass through them. These parts are made of transparent materials with a refractive index $n > 1$ where the spatial phase variation is faster than in vacuum (air). **Figure 1.1b** shows the focusing of a plane-wave beam by a convex lens. The lens has a gradient thickness varying in the radical direction and light rays at different distance from the lens axis undergo a different effective propagation length in the high-index medium. Due to the accumulated phase delay, the lens produces a spherical wave-front profile that concentrates light to the focal point.

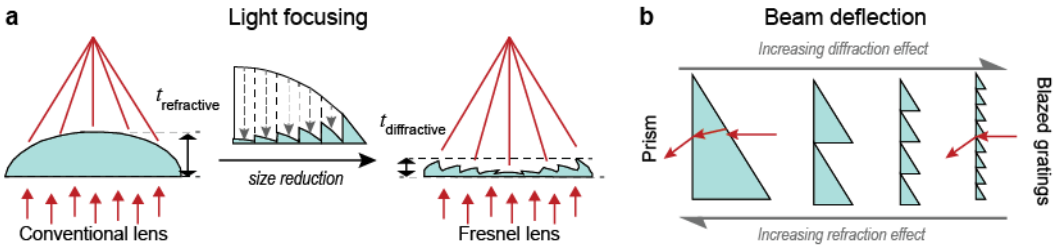

Figure 1.2. Diffractive optics can maintain a smaller thickness compared to refractive counterparts for any targeted device size. (**a**) Scheme depicting how light focusing is achieved by Fresnel lenses designed based on the conventional lenses. (**b**) Scheme depicting the working principles of diffractive gratings as alternatives to prisms in beam deflection. Figure (a) is reproduced from Miller *et al.*[3] and Sierra *et al.*[4] Figure (b) is reproduced from Sinzinger and Testorf.[5]

1.1.2. Demonstrations of compact diffractive optics

With a large thickness, conventional refractive optics are unsuitable for applications that require large-area light manipulation, including lighthouse illumination, green house lighting, and solar cell light collection,[4,15] because of their heavy weight. Diffractive optics have been developed to maintain a small, constant thickness regardless of the overall footprint of the design. **Figure 1.2a** shows how thin Fresnel lenses can be obtained from the conventional spherical lenses. Because the wavefront phase in Equation 1.3 is a periodic function in $0-2\pi$, a smooth surface with gradual thickness (light path length) variation is not required to produced a continuous spherical wavefront for light focusing. Therefore, the same focusing response could be achieved from a lightweight device by removing rectangular blocks of the dielectric materials from the refractive lens while projecting the curved surface structures to the substrate. The resulting lens designs not only have advantages of portability, but can also exhibit smaller spherical aberrations than tranditional lenses.[3] The same strategy can be applied to beam-deflection using diffractive gratings as replacements to prisms. **Figure 1.2b** shows schematically the design of blazed gratings based on prisms by iteratively scaling down the structure into half of the size and while doubling the density of the units in a periodic grating arrangement. The resulting blazed gratings, however, rely more on the diffraction in directing the light flow and may produce light beams at unwanted angles by high-order diffraction.[5]

The major disadvantage of diffraction optics is that their unit structures with continuously varying thickness are difficult to fabricate. For example, a process based on electron-beam lithography (EBL) using a 200-nm beam only achieved gratings with a 5-μm periodicity and the produced structures exhibited surface defects that degraded the diffraction efficiency and focal tightness.[16] Another technique based on laser lithography showed improved surface roundness but the minimum groove sizes realized were 3 μm because the laser beam size was larger than 700 nm due to the diffraction limit.[17] Even with recent developments in nanofabrication methods, the complex features in these diffractive optics cannot be made in nanoscale thickenss with a cost-effective and scalable method.

1.1.3. Subwavelength light manipulation on a flat binary surface

The fabrication challenges of the conventional diffractive optics can be tackled by replacing the units having gradually varied height with designs having a two-level height profile that allow one-step patterning by well-established lithography methods. **Figure 1.3** shows schematically how grating building blocks with a triangular out-of-plane cross-section can be replaced by isolated units at a constant height. The triangular cross-section is first subdivided into trapezoids and approximated by rectangular posts with different heights. The multilevel gratings can be patterned by planar nanofabrication methods in multiple cycles of resist-coating, pattern writing, materials deposition, and lift-off steps. This procedure, however, is not only slow in patterning speed, but also constrained by stringent alignment requirements between each lithography pattern and deposition. If the subdivided units have sizes below the wavelength of the light, this grating can be replaced by arrays of **subwavelength** phase elements that have the same height but different in-plane sizes and shapes. These planar optical surfaces with rational-designed building blocks – **metasurfaces** – can be made in a single fabrication step.

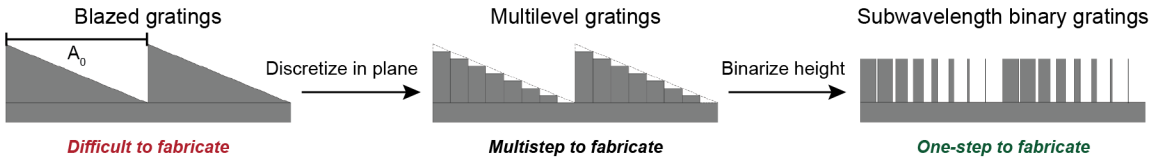

Figure 1.3. Planar optical metasurfaces enables one-step fabrication. Scheme depicting the evolution from traditional diffractive optics to flat metasurface designs. Figure is reproduced from Yang *et al.*[6]

1.2. Design Principles of Metasurfaces

Metasurfaces can not only function as compact replacements of conventional optical elements (such as lenses and prisms) but also realize optical responses not possible in existing refractive components. This section reviews the materials systems and design process of optical metasurfaces for applications including beam deflection, light focusing, and optical holography and discusses the major challenges of existing approaches that will be addressed by the thesis projects.

1.2.1. Versatile beam deflection on a flat surface

I will start the introduction of metasurfaces with a simple example continuing on the previous discussions on blazed gratings but with more detailed nanoscale design principles. **Figure 1.4a** shows a scanning electron microscopy (SEM) image of the V-shaped Au nanoparticles (NPs) where the 8 highlighted units form the super-cell that replaces the function of a period in the blazed gratings[7] To deflect an incidental plane wave light into an arbitrary output angle, I need to transform the original wavefronts which are parallel to the substrate to inclined planes by the subwavelength antennas. **Figure 1.4b** shows the wavefront phase profiles of plane-wave light before and after passing through the individual Au NPs. With the same thickness, these plasmonic NPs could induce abrupt wavefront phase delay tailored by their size and shape. From left to right in the super-cell, the 8 antennas induced gradually increasing phase changes in the $0 - 2\pi$ range at a step of $\pi/4$. The overall wavefront exhibited a gradient phase profile in the far-field and the beam was therefore deflected into the direction orthogonal to the wavefront.

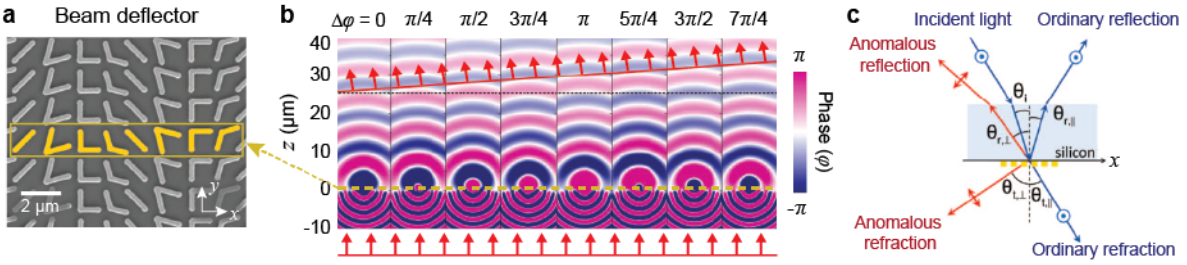

Figure 1.4. Arrays of V-Shaped plasmonic antennas can deflect light to arbitrary angles. (**a**) Scanning electron microscopy (SEM) images showing a representative metasurface beam deflector for the wavelength range λ = 5-10 μm (**b**) Finite-difference time-domain (FDTD) calculations of the scattered electric field for the individual antennas in (a).(**c**) Scheme depicting the concepts of anomalous refraction and reflection that can be achieved by a transparent substrate with this metasurfaces patterned on one side. This figure is reproduced from Yu *et al.*[7]

The wavefront tuning process can also be used for tuning the reflection angle. **Figure 1.4c** shows schematically the control of reflection and refraction angles on a transparent substrate with these beam-deflecting metasurface patterns. Besides the beam steering responses of prisms and mirrors, these metasurfaces can also achieve anomalous properties not possible by conventional devices, including negative refraction and reflection of electromagnetic radiations in the wavelength range of $5-10\ \mu m$.[7] Operation in the near-infrared (NIR) range (λ = 1000-1900 nm) was demonstrated using V-shaped phase elements with smaller sizes and spacings.[18] Beam steering in the reflection configuration was also extended to the visible range using long Ag and Al resonators in triangular shapes as super-cells.[19,20] These designs simplified the fabrication requirements significantly by replacing complex V-antennas with a single triangular slab.

1.2.2. Metalenses for light focusing and imaging

Planar lenses can be designed for light focusing based on metasurface design principles. To obtain a focal point, the phase elements must produce a spherical wavefront phase profile defined as:[8]

$$\phi(r) = \frac{2\pi\sqrt{r^2+f^2}}{\lambda} \tag{1.4}$$

Figure 1.5a shows a microlens based on V-shaped nanohole units which are the Babinet-inverse structures of the NPs in the previous section. Because of the difficulties in fabricating these V-antennas, the experimental lens units deviated from the ideal structures in simulation and the measured focusing profile shoId noisy background. These lens designs Ire low in efficiency and therefore not suitable for imaging. **Figure 1.5b** shows a high-efficiency dielectric metalens for imaging in the visible range. This lens focused circularly polarized light by high-aspect-ratio nanofin TiO_2 units (height h = 600 nm) fabricated by a procedure based on EBL, atomic-layer deposition (ALD), and directional dry etching.[9] These metalenses achieved high resolution imaging of microscale patterns in the 1951 USAF resolution chart with high numerical aperture (NA = 0.8) at wavelengths in the λ = 480-620 nm range. Polarization insensitive metalenses were also achieved with TiO_2 posts with cylindrical shape for visible wavelengths.[21]

Metalenses exhibited aberrations in light focusing similar to conventional refractive optics. Spherical aberrations, for example, are the defocusing effects observed when the incident angle increased and can be a prominent issue in microscope objectives with high-NA and lenses for wide-angle cameras. Although single-layered metalenses cannot avoid spherical aberrations without compromising other focusing performances, metalens doublets have achieved lensing with the minimum spherical aberrations. A metalens doublet was demonstrated for wide-angle photography at λ = 850 nm by patterning a correction metasurface on the other side of the substrate with the focusing lens.[22] Compared to refractive lenses, metalenses (or diffractive lenses in general) typically exhibit larger chromatic aberration aberration where focal length changes when focusing light at different wavelengths. By engineering the dispersion responses of the metasurface elements, achromatic focusing was first demonstrated in the NIR range,[23] and then at visible wavelengths[24] for circularly polarized light.

1.2.3. Other applications of metasurfaces

The ability to realize complete control over the wavefront phase at subwavelength resolution opens up tremendous opportunities to control light.[25]. For example, a quarter-wave plate that could transform linearly polarized light to circularly polarized light was achieved by arrays of V-shaped antennas for the

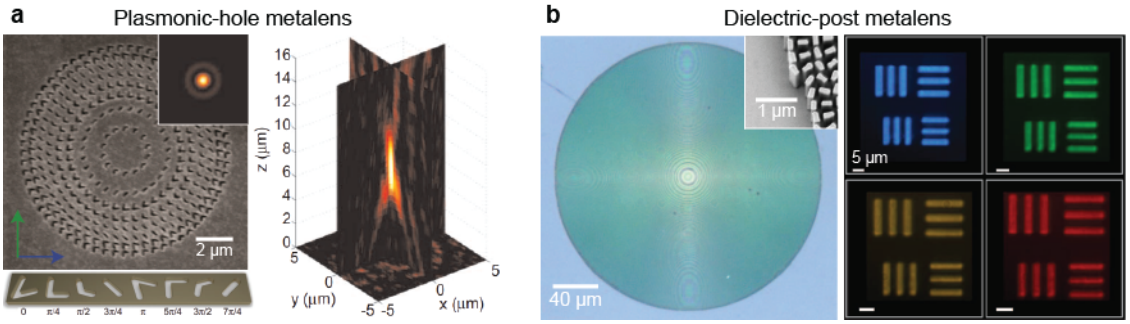

Figure 1.5. Metalenses for light focusing and imaging in the visible wavelength range (**a**) Light focusing by metalens consisting of V-shaped nanoholes on a Au film. (Left) SEM image depicting the structure of the plasmonic metalens. Inset (5×5 μm^2) shows the simulated focal point profile at $\lambda = 531$ nm. (Right) Measured three-dimensional (3D) light profile of a focal point at $z = \mu m$ above the lens surface.(**b**) A dielectric metalens based on TiO_2 for imaging in the visible range. The optical images Ire measured from the 1951 USAF resolution test chart at wavelengths of 480, 530, 590, and 620 nm. Figure (a) is reproduced from Ni *et al.*[8] Figure (b) is reproduced from Khorasaninejad *et al.*[9]

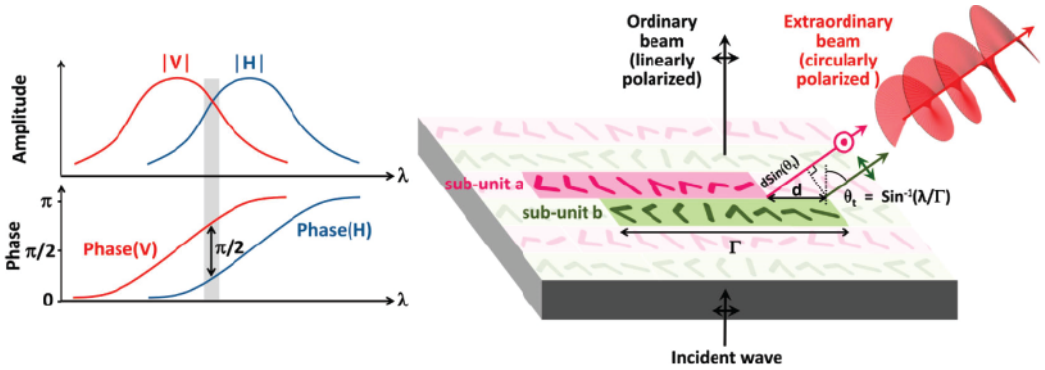

Figure 1.6. Metasurfaces can realize versatile polarization conversion Scheme showing how circularly polarized light could be generated by two beams with orthogonal polarization and $\pi/2$ phase difference. Figure reproduced from Yu *et al.*[10]

wavelength range $\lambda = 5$-12 μm.[10] This design was based on alternating two periodic rows of NP supercells, where the rows generate two waves with equal amplitudes and orthogonal linear polarization angles but with a $\pi/2$ phase difference by spatial arrangement (**Figure 1.6**). Conversion to all six polarization angles was demonstrated by arrays of Al nanorods using a similar strategy.[26]

Metasurfaces also realized holographic displaying of complex images. **Figure 1.7** shows demonstrations of plasmonic metasurface holograms using two types of Au phase elements as the building blocks.

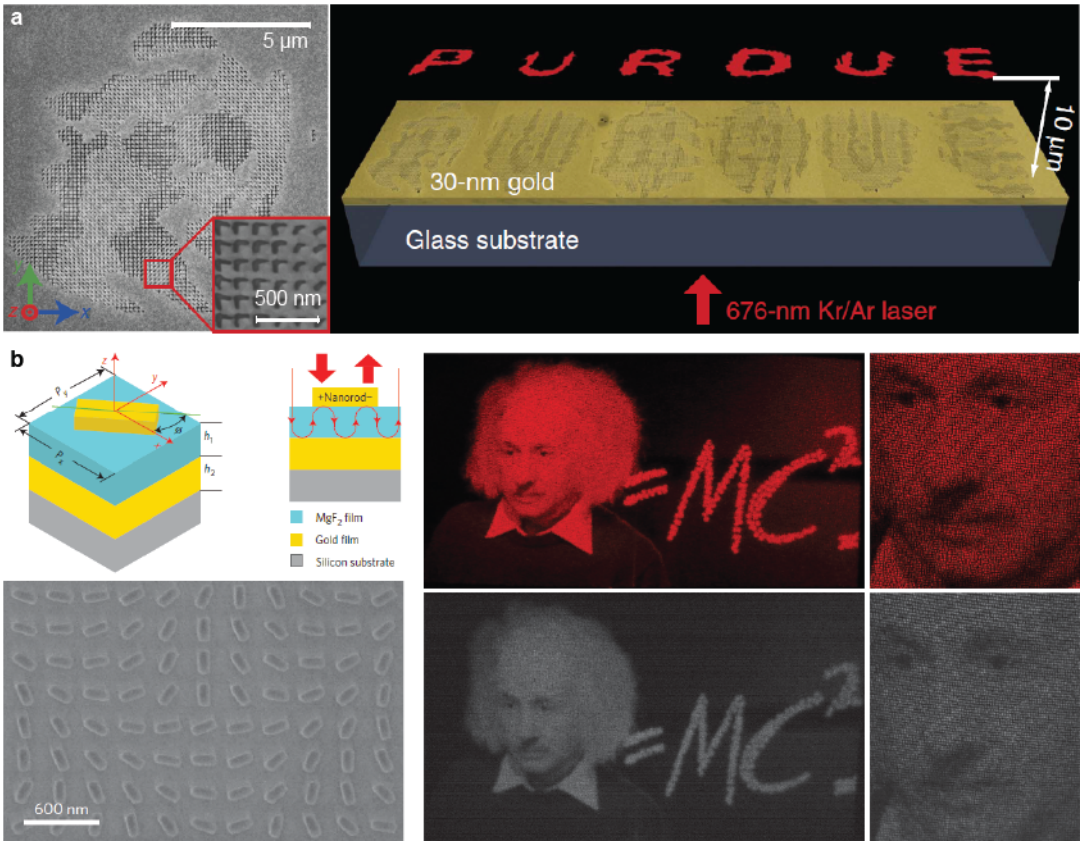

Figure 1.7. Metasurfaces for optical holography. Metasurface holograms consisting of (**a**) V-shaped phase elements (holes) in transmission configuration and (**b**) nanorods on a gold film with a gap in reflection mode. Holograms operated at 676 nm in (a). Holograms in (b) Ire obtained at (upper right) 633 nm and (loIr right) 780 nm. Figures reproduced from Ni *et al.*[11] and Zheng *et al.*.[12]

Optically encoded information Ire programmed in a Au film with only 30 nm thickness (Figure 1.7a).[11] The reflection mode metasurface not only functioned at multiple wavelengths in the visible and NIR range, but also exhibited up to 80% efficiency (Figure 1.7b).[12] Colored holograms Ire also accomplished by superimposing Si nanoblocks with three different sizes to tailor independently red, green, and blue light, respectively.[27]

1.3. Evolutionary Algorithms for Metasurface Design

Fundamentally, metasurfaces can outperform refractive optical elements because their ability to tune the wavefront at subwavelength scale offers tremendous freedom in the control over light. The advances in numerical electromagnetic modeling methods such as finite-difference time-domain simulations also enable prediction of optical properties from complex nanostructures that cannot be modeled accurately by analytic approaches. However, most existing metasurfaces are still designed based on wave-optics principles developed from conventional optics. We believe that these wavefront principles (such as beam steering requires a linear gradient-phase wavefront, and light focusing requires a spherical wavefront) are restricting the potential of metasurfaces which can only be fully exploited by novel design strategies combining the numerical modeling techniques, optimization algorithms, and potentially machine learning methods. This section introduces our previous progress on designing metasurfaces with a genetic-algorithm based approach developed by Dr. Mark Huntington. The thesis work developed this algorithm further and the details of the actual implementation will be described in later chapters.

1.3.1. Design challenges for binary nanohole lattice optics

We aim to explore the digital design of planar optics assuming the minimum knowledge about wave-optics. In contrast to previously discussed metasurfaces that consist of phases elements with a variety of different size, shape, and orientation, the algorithm started with the simplest design unit – a circular nanohole. The target optical responses was obtained only by deciding whether to open a hole on a square grid of, for example, 33×33 lattice points. **Figure 1.8** shows the digital representations of nanohole lattice metasurfaces structures, where 1 denotes an open hole and 0 denotes a closed hole. Although the metasurface structure was simplified significantly by limiting the choice of phase elements to two, there were still $2^{33\times33}$ possible configurations on this design area, and the size of this computation problem could not be solved by exhaustive searching approaches that enumerated the all possibilities.

Referenced work: M. Huntington, L.J. Lauhon, and T. W. Odom, "Subwavelength lattice optics by evolutionary design" Nano letters **2014**, *14* (12), 7195-7200, DOI: 10.1021/nl5040573

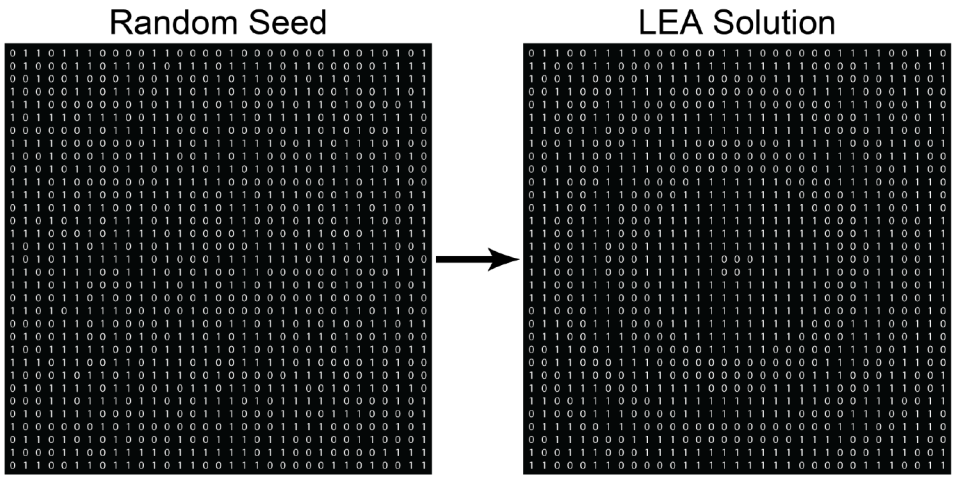

Figure 1.8. The design problem in binary subwavelength lattice optics. Schemes showing (left) random initial configurations of metasurfaces and (right) an optimized metasurface design resembling Fresnel lenses encoded in binary strings. Figure reproduced from Huntington *et al.*[13]

Fortunately, structures encoded as binary strings – digital genetic materials represented by DNA of 0s and 1s – can be optimized efficiently by the **genetic algorithm**, a heuristic method that starts with a population of random guesses and identifies the optimal solution iteratively in a process mimicking the evolution of species by natural selection. In each generation, the genetic algorithm evaluates all candidate structures including the initial random guesses by a fitness function $\boldsymbol{F}$ defined based on the desired properties. The next generation is constructed based on the previous one where strings with larger fitness functions have a larger chance to survive and duplicate. To apply the genetic algorithm to our lattice optics design, however, we still need an efficient method to calculate the optical properties from the encoded strings and a definition of fitness function to evaluate the performances quantitatively.

1.3.2. Lattice evolution algorithm to design lattice lenses

The lattice evolution algorithm (LEA)[13] was developed to solve for the structures of binary lattice optics by combining electromagnetic simulations and the genetic algorithm. **Figure 1.9** summarizes the procedures of the algorithm. Similar to other evolutionary algorithms, the LEA was initialized with a 600-member population of candidate nanohole lattices encoded as strings of 0 and 1 with randomly

generated sequences. In each optimization iteration, the current population was evaluated by the fitness function to be defined (step 1) and sorted in the order of decreasing fitness values (step 2). The new generation of the population was created by combining the binary strings of the previous generation (step 3). In this combination process, preference was given to members of the population with higher fitness. The cycle continued until the LEA reached a convergence condition (step 4), which we designated as when the the fittest member in the population did not change for 30 generations.

The far-field wavefront profiles were first calculated by point-source simulations [28] based on Huygens-Fresnel principles [29] which approximated each open nanohole as an independent dipole that generated a spherical wave. [13] FDTD simulations were used to model the designs with improved accuracy when materials properties and unit sizes/shapes were important for the targeted optical responses. To increase the efficiency of the LEA, we first stored all of the complex field information in memory. Then, we could calculate the 3D optical profiles by adding different combinations of complex fields instead of simulating the entire field for each lattice structure. To obtain a single focal point the fitness function is defined as:

$$F(\Delta f) = \frac{I}{\Delta f + c} \tag{1.5}$$

where F was the fitness value, I was the intensity at the desired focal point, Δf was the deviation between the desired and actual focal points, and c was the a positive constant (10^{-5}) which avoided the singularity when $\Delta f = 0$.

We tested the algorithm on a 33×33 lattice of nanohole with diameter $d = 150$ nm on a 180-nm thick Au film for light focusing at a near-infrared wavelength $\lambda = 690$ nm. **Figure 1.10** shows two representative designs of the lattice lenses with the focal lengths $f = 4$ and 10 μm optimized by LEA based on the electric fields calculated by point-source simulations. The corresponding optical profiles were measured from the lens structures fabricated using focused-ion beam (FIB) milling by scanning confocal microscopy in comparison with results calculated by electromagnetic simulations. The focal points were observed at exactly the predicted positions with slightly increased background noise and larger full-width at half-maximum (FWHM).

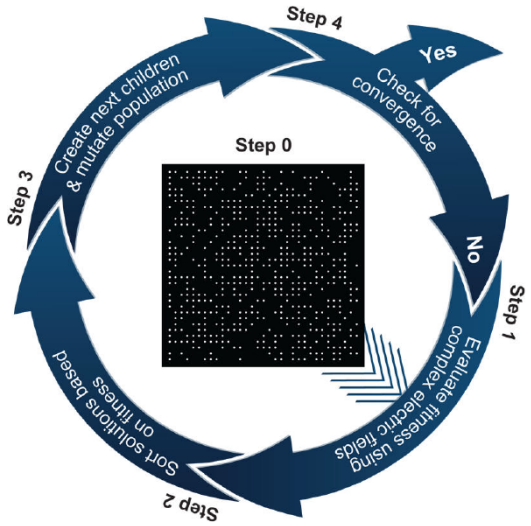

Figure 1.9. Evolutionary design methods can be used to design lattice metasurfaces with unique focal properties. Scheme depicting the four steps involved in the lattice evolution algorithm (LEA). Step 0 is a randomly arranged lattice. Figure reproduced from Huntington *et al.*[13]

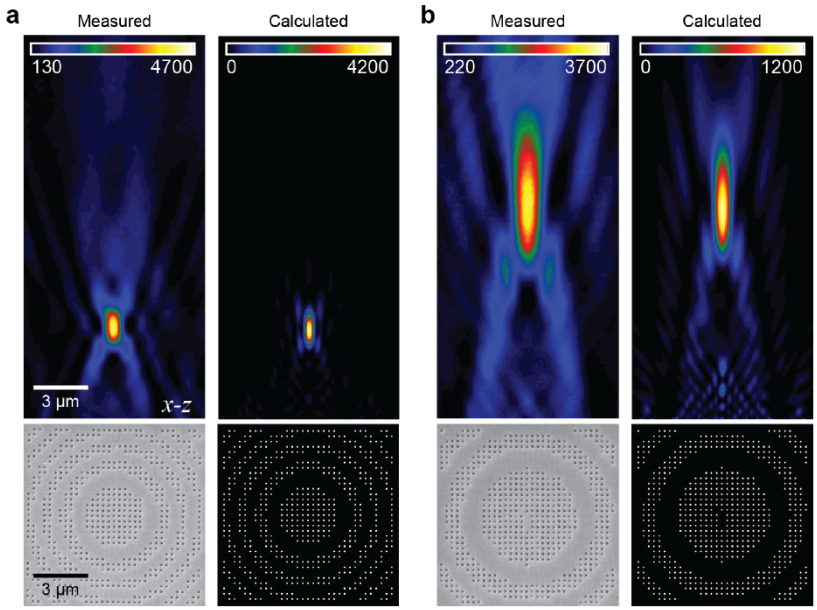

Figure 1.10. Measured data matches simulated results for lattice lenses with a single focal point. SEM images of the lattice structures (lower left) and identical simulated structure (lower right) for (**a**) $f = 4$ μm and (**b**) $f = 10$ μm. Confocal microscopy field data (upper left, $\lambda = 690$ nm) has the same profile as the corresponding data simulated using the point-source approximation (upper right) for both (a) $f = 4$ μm and (b) $f = 10$ μm. Figure reproduced from Huntington *et al.*[13]

1.3.3. Multifocal lensing and dynamic focusing by polarization state

LEA can also achieve multi-level phase control using nanoholes with different sizes and shapes using optical fields calculated by FDTD simulations. We tested multiphase designs using circular nanoholes with d = 100, 150, and 200 nm. To represent the different hole sizes in the LEA, we added a second binary digit to the binary string so that each position on the 2D grid now had one of the four values: 00 (closed hole), 01 (d = 100 nm), 10 (d = 150 nm) or 11 (d = 200 nm). This extra tunability in phase control enabled focusing to multiple foci simultaneously. Multiple focal points can be achieved using a compound fitness function:

$$F = \sum_{i=1\ldots n} \frac{F_i}{F_{i,\max}} \tag{1.6}$$

where n was the total number of light spots, F_i was the fitness value calculated for the specific structure at the ith focal point using Equation 1.5, and $F_{i,\max}$ was the maximum fitness value achieved by the current generation at this focal point.

Figure 1.11 shows the lattice metasurfaces designed to concentrate light at five distinct locations. Prime numbers of focal points were tested to illustrate that these solutions were not a result of diffraction from Talbot effect. Figure 1.11a demonstrates that a nanohole lattice with a single phase element could create 3D optical profile with five light spots arranged in a ringe structure. For metasurfaces, phase control over adjacent unit structures is critical to observe anomalous far-field optical properties.[30]. In contrast, the LEA-designed lattice optics can generate different optical profiles without phase contraints on neighboring lattice elements. Figure 1.11b indicates that the LEA can also manipulate light into holographic T shapes with improved efficiency by additional phase elements. These measured light profiles also matched well with the optical fields calculated by FDTD simulations.

The LEA could be used with nanoscale elements with different shapes using FDTD simulations. We used elliptical holes that transmit up to 100 times more light when the polarization is perpendicular to the major axis of the hole.[28,31] Therefore, elliptical nanoholes could be effectively opened and closed by tuning the polarization state. In these case, each of the grid point can take one of the three values:

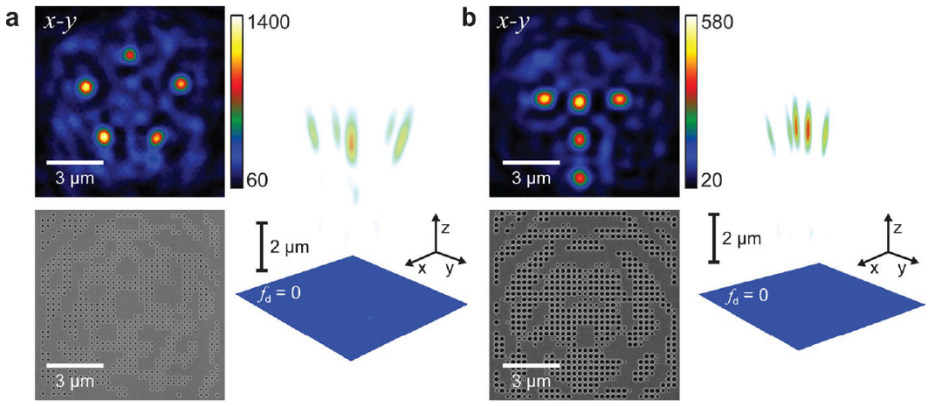

Figure 1.11. Lattice metasurfaces can generate arbitrary light profiles in 3D. SEM images of lattice structures (lower), 2D confocal microscopy slices at the focal plane (upper, $\lambda = 690$ nm) and 3D volume profile (right). (**a**) Five focal points at $f = 7$ μm from single phase elements. All focal points had a constant distance ($r = 3$ μm) from the center of the lattice. (**b**) Five focal points at $f = 7$ μm from three phase units in a T shape with 1-μm separation between points. Figure reproduced from Huntington *et al.*[13]

00 (closed hole), 01 (vertical ellipse), or 10 (horizontal ellipse). The enhanced transmission by plasmon resonance of the elliptical hole ($r_{minor} = 70$ nm, $r_{major} = 250$ nm) was at $\lambda = 770$ nm, so we designed and measured our devices for this wavelength. **Figure 1.12** shows the switching between two focal points at $f = 7$ μm by switching the polarization states. Under unpolarized light, both foci were observed.

1.4. Summary

The emerging metasurfaces can not only replace traditional refractive optics in light focusing and beam steering in planar ultra-compact architectures, but also open up new strategies to manipulate light with their ability tailor the wavefront at subwavelength scale. Novel design method based on evolutionary algorithms explored only a small portion of the possible designs by restricting the choice of phase elements to 2-4 nanohole types, but already achieved a range of optical responses not possible by conventional optics.

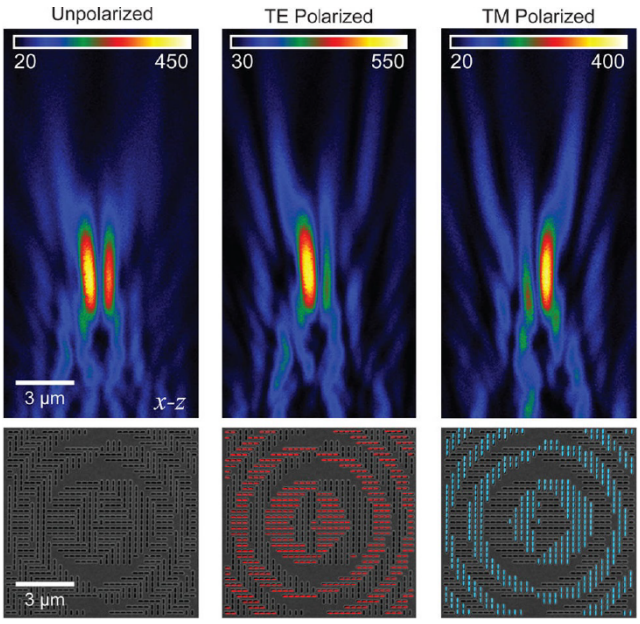

Figure 1.12. Lattice optics can exhibit dynamic optical profiles based on polarization of incident light. Polarization-sensitive lattice metasurfaces with dynamic focal shift ($f = 7$ μm and $x = \pm 0.5$ μm, $y = 0$). (Lower) SEM images of the lattices and (upper, $\lambda = 770$ nm). Holes active under TE and TM polarization are indicated in red and blue, respectively. Figure reproduced from Huntington *et al.*[13]

CHAPTER 2

Evolutionary Design and Prototyping of Single-Crystalline Titanium Nitride Metasurfaces

This chapter describes the design and prototyping of single-crystalline titanium-nitride plasmonic metasurfaces based on subwavelength hole arrays. The lattice evolution algorithm with a new multi-objective fitness function was developed to produce a variety of 3D light profiles with balanced intensities at the light spots. I also demonstrated a simple, efficient technique to prototype these lattice designs in large-area titanium nitride films by combining focused ion beam milling and wet chemical etching. Multi-level phase control was achieved by tuning nanohole size, and multi-point focusing with arbitrary light spot patterns was realized. Using anisotropic nanohole shapes, the titanium-nitride lattice lenses could exhibit dynamic tuning of the focal profiles by changing the polarization of incident light.

Referenced work: J. Hu, X. Ren, A. N. Reed, Thaddeus Reese, D. Rhee, B. Howe, L. J. Lauhon, A. Urbas and T. W. Odom, "Evolutionary Design and Prototyping of Single Crystalline Titanium Nitride Lattice Optics." *ACS Photonics* **2017**, *4*, 606—612. DOI: 10.1021/acsphotonics.6b00955.

2.1. Materials and Design Challenges in Plasmonic Metasurfaces

In the previous chapter, we introduced plasmonic metasurfaces as a class of planar devices that control light based on subwavelength structures. Metasurface architectures are typically determined by arranging subwavelength units on a 2D surface to produce the desired phase profiles based on wave-optics principles. With features less than 100 nm in thickness, plasmonic metasurfaces have shown attractive functionalities ranging from broadband beam steering[18,19] to optical holography.[11,12] Their flat structures can be potentially integrated in optoelectronic devices to realize on-chip applications.[32] Traditional plasmonic materials including Ag and Au, however, are not compatible with silicon-based processing techniques used in the semi-conductor manufacturing.[33] For example, metals including Au, Ag, Cu, and Al exhibit undesirable diffusion into substrate materials (for example, Si) at elevated temperatures and degrade device performance. Also, nanostructures based on these metallic materials have limited mechanical strength[33] and lack the high-temperature stability[34,35] required for operation in extreme conditions.

2.1.1. Plasmonic metasurfaces based on singe-crystalline titanium nitride

Titanium nitride (TiN) is emerging as an unconventional plasmonic material for applications at NIR wavelength range because of its hight mechanical strength,[33,36] superb heat stability,[34,37] and potential CMOS compatibility.[33,38,39] This seminconducting material not only exhibit a Au-like dielectric function, but also allows tuning of optical properties by doping. However, studies of TiN metasurfaces have been limited to single phase elements[39] or periodic arrays of identical units;[34,37,38] subwavelength control over the phase profile has not been achieved. One major reason is that existing patterning techniques[37,40] for TiN films cannot realize the nanoscale features needed to tune precisely the wavefront.[39] Also, methods based on lithography on resist, nitrides deposition, and lift-off can only produce TiN nanostructures with low crystallinity and high non-radiative losses that limit the device efficiency.[37] Therefore, the development of TiN metasurfaces requires both improvements in prototyping methods an simplification in the design of the phase-element structures.

2.1.2. Advantages of lattice evolution algorithm

We developed the LEA as an efficient approach to design nanohole metasurfaces in a Au film.[13] In contrast to the conventional metasurfaces design based on analytically determined phase profiles, LEA aims to optimize directly desired optical properties such as light spot patterns and intensities, where the targeted response was represented by a fitness function F and a genetic algorithm was used to find the physical structure with the maximum fitness value. LEA can converge consistently to the same optimal fitness level starting from a population of random structures. The simple design units also granted easy fabrication process that could be potentially extended to pattern TiN metasurfaces.

In contrast to exhaustive approaches[41] and search methods including Monte Carlo, evolutionary algorithms are more advantageous at solving more than one criteria simulataneously.[42,43] The ability to carry out multiobjective optimization has enabled the design of lattice optics that could exhibit multiple focal spots arranged arbitrarily in3D space with each focal spot regarded as an objective.[13] However, while the positions were well predicted and demonstrated experimentally, the intensities at the focal points were often unbalanced because the form of the fitness function Equation 1.6 was based on function transformation principles,[42] which offers limited control over each focal point. In addition, the entire LEA method was implemented in a single function with a *procedure-oriented programming* style that makes user customization and future development difficult.

2.2. Object-Oriented Lattice Evolution Algorithm for TiN Metasurfaces

This section shows the design of TiN lattice optics by an object-oriented lattice evolution algorithm (OLEA). Implemented in an object-oriented programming style, this method encapsulated the majority of code contents into different C++ classes and users only needed specify parameters including focal positions, polarization, and wavelengths in a simple main function. The organized code also allowed maintenance at ease, where functions in different modules could be tested and upgraded separately, so that the program can potentially integrate new functionality quickly.

The multiobjective optimization method used an inverse-form ftiness function that enabled precise tuning of the intensity at each focal spot. Materials properties were accounted for by inputing dielectric functions of TiN into FDTD simulations of the nanohole units. We also used FDTD simulations of the optimized lenss to show that the designs were remarkably tolerant to structural defects that could be introduced in the fabrication process.

2.2.1. Optical characterization and modeling of TiN in preparation for OLEA calculations

The electronic and optical properties of TiN could vary with stoichiometry, surfaces roughness, and crystallinity determined by the choices of substrate and growth condition. **Figure 2.1a** shows the atomic force microscopy (AFM) image of the surface of a 54-nm TiN film grown on sapphire substrate by controllably unbalanced reactive magnetron sputtering at 600 °C in a low vacuum environment (pressure $P = 0.02$ Torr, 1:1 N_2:Ar).[44] This process using 100-W target power achieved a rapid growth rate (0.1 nm/s) and a low film roughness ($R_a < 0.1$ nm). **Figure 2.1b** depicts the X-ray diffraction pattern where the thickness fringes indicated a near-perfect crystallinity of the TiN films. **Figure 2.1c** shows the dielectric functions of TiN film (used in FDTD simulations) in comparison with a Au film measured by ellipsometry. Our TiN samples could support surface plasmons in the regime $\lambda > 550$ nm, where the real part of the prmittivity ϵ' was negative. This specific TiN exhibited higher plasmonic losses than Au in the wavelength range of 600-1100 nm because of its larger imaginary part of permittivity.

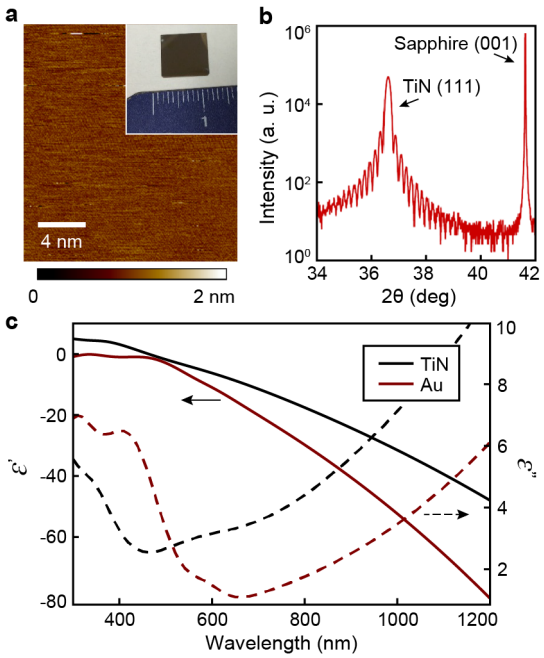

Figure 2.1. Controllably unbalanced reactive magnetron sputter deposition can produce high-quality TiN film. (**a**) Atomic force microscopy (AFM) image of the TiN film showing a smooth surface with roughness $R_a = 0.1$ nm. The inset shows a photo of the sample with a size around 1 cm.(**b**) X-ray diffraction (XRD) data of TiN with thickness fringes demonstrating exceptional film quality.(**c**) Dielectric properties of TiN in comparison with Au over wavelengths in the visible to near-infrared measured by ellipsometry.

Figure 2.2a shows the transmission spectrum for periodic arrays of circular and elliptical nanoholes in a TiN film calculated by FDTD simulations using experimentally measured dielectric constants. Circular nanoholes ($d = 200$ nm, $a_0 = 300$ nm) showed a surface plasmon polariton (SPP) resonance at a wavelength $\lambda = 800$ nm. the anisotropic nanoholes exhibited polarization dependent linear properties, where the transmission of incident light polarized along the shorter axis could be up to 2 times larger than those polarized along the longer axis. The spectra with light polarized along the shorter axis showed a red-shift in the SPP that increased with the aspect ratio of the nanoholes. **Figure 2.2b** shows a cross-section of the near-field enhancement around the TiN nanoholes, where a higher aspect ratio contributes to larger field intensity. Similar to LEA procedures described in the previous chapter, the electric field components of light transmitted through a single nanohole (in a periodic array) were exported from these

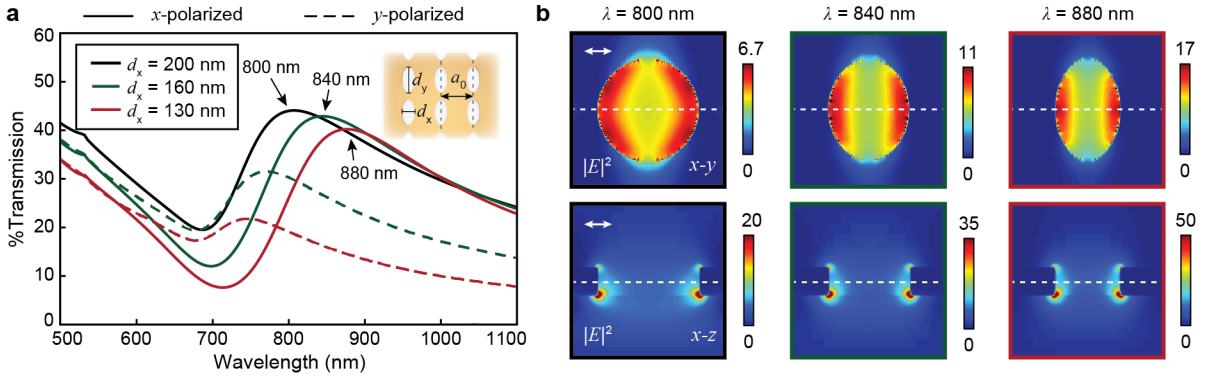

Figure 2.2. Surface plasmon polariton (SPP) resonance wavelength and intensity can be tuned by nanohole size and shape. (**a**) Transmission spectra calculated by finite-difference time domain (FDTD) simulations for periodic array of circular (d = 200 nm) and elliptical (d_1 = 200 nm, d_2 = 160, 130 nm) nanoholes. (**b**) Near-field intensity cross-sections in (upper) x-y and (lower) x-z planes for the three nanoholes extracted at their SPP resonance wavelength.

FDTD simulations at the targeted lensing wavelengths, projected into a 3D far-field region, and then exported into text data files for OLEA calculations.

2.2.2. OLEA design of TiN metasurfaces

Figure 2.3 depicts the design procedures of TiN metasurfaces in our evolutionary algorithm. Similar to the original LEA, the OLEA started with a population of random structures represented by binary strings of 0 and 1. Then, the method iteratively evaluated the far-field optical profiles of the strings in the current population and constructed the next generation by giving the fitter structures larger chances to survive and duplicate.[13] The algorithm terminated and exported the optimized lattice structures the the fitness value was constant for 30 generations.[13] To account for materials properties, we measured the complex dielectric constants of TiN by ellipsometry Figure 2.1 and imported the dielectric function into the FDTD models.[45–47] Then we calculated and exported the electric field components of the transmitted light to the selected nanohole units before OLEA design.(Figure 2.2) To expedite the fitness evaluation step, the OLEA calculated the optical profiles by adding the field components contributed by each lattice unit directly.[13]

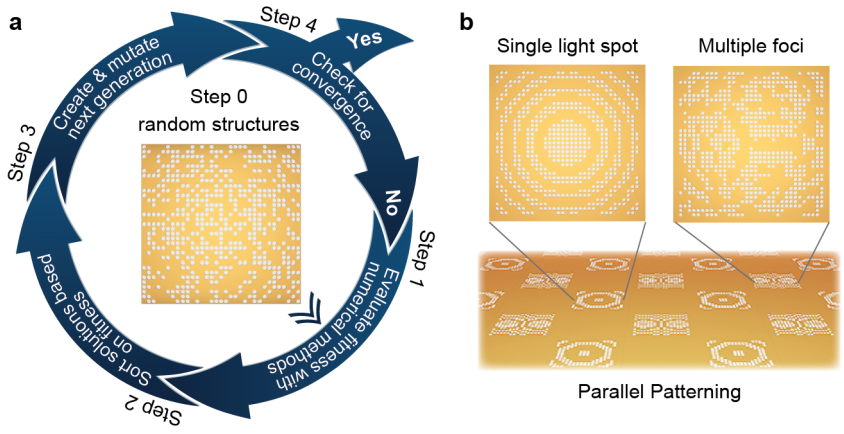

Figure 2.3. Scheme depicting the evolutionary design process and the optimized structures patterned by our prototype technique.

Our preliminary OLEA calculations were based on 33×33 lattices ($a_0 = 300$ nm) of a single phase element: a circular nanohole (diameter $d = 200$ nm). This TiN nanohole array showed a SPP resonance at $\lambda = 800$ nm, where enhanced optical transmission (EOT) was maximized (Figure 2.2). Therefore our metasurface designs targeted the operation wavelength $\lambda = 800$ nm to achieve the optimal transmission efficiency (fraction of optical power transmitted through the lattice). For a single foal point, the fitness function was still defined as Equation 1.5:

$$F(\Delta f) = \frac{I}{\Delta f + c} \tag{2.1}$$

Again, F was the fitness value, I was the intensity at the desired focal point, Δf was the deviation between the desired and actual focal points, and c was a positive constant. **Figure 2.4** shows the schemes of TiN nanohole lattices for focal distances ranging from $f = 3$ to 10 μm. As expected, focal points broadened as the focal length increased (when the NA decreased). The depth of focal was also the smallest for $f = 3$ μm.

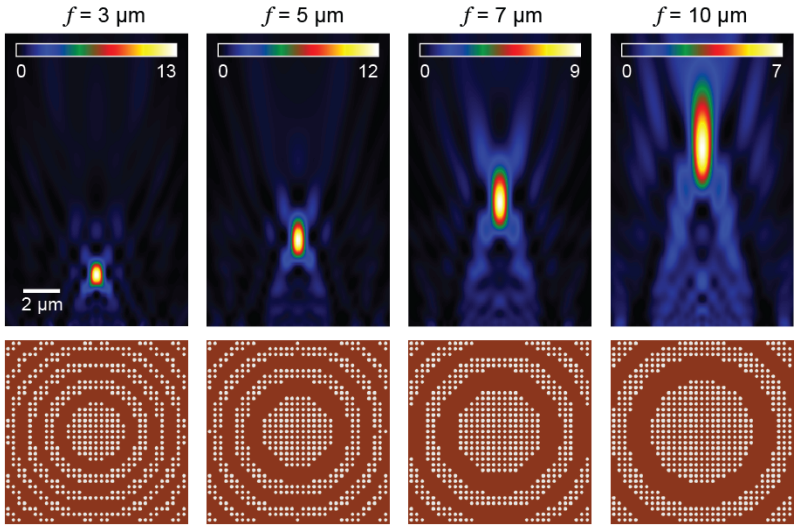

Figure 2.4. OLEA can design single-focal TiN metalenses. (lower) Schemes depicting the TiN nanohole lattice structures optimized for focal lengths f = 3, 5, 7, and 10 μm and (upper) the corresponding optical profiles calculated by FDTD simulations at λ = 800 nm. The lattice designed had a footprint of 10 μm × 10 μm and 33 × 33 array with a_0 = 300 nm. TiN hole size d = 200 nm.

2.2.3. Inverse-form fitness function for multiobjective optimization

Our previous LEA could solve for multiple focal points with controlled 3D arrangements using a generalized F[13] Equation 1.6 based on function transformation principles:

$$F = \sum_{i=1\ldots n} \frac{F_i}{F_{i,\max}} \tag{2.2}$$

where n was the total number of light spots, F_i was the fitness value calculated for the specific structure at the ith focal point using Equation 1.5, and $F_{i,\max}$ was the maximum fitness value achieved by the current generation at this focal point. However, the optical intensity at the focal points optimized using this function were often unbalanaced and could not be tailored independently. This lack of control was common in optimization problems with multiple conflicting objectives where there will be multiple or even an infinite number of Pareto optimal solutions; increasing the performance at one criterion cannot be achieved without decreasing others.[48–50] In our design process, the specific Pareto solutions obtained from OLEA calculations depended on how we defined the overall fitness function F as a function of the

fitness values at each focal point. **Figure 2.5a** shows the map of the combined fitness functions from two focal points using the linear summation defined in Equation 1.6 which showed no preference to the solutions with balanced individual fitnesses ($F_1 = F_2$) as long as their linear sum remained the same. Consequently, the calculations conduced with this Equation 1.6 were prone to converge to a solution satisfying only one criterion. We adopted an alternative fitness function having the inverse form:

$$F^{-1} = \sum_{i=1\ldots n} {F_i}^{-1} + \frac{1}{2}\sum_i \sum_j |F_i - F_j|/(F_i + F_j)^2 \tag{2.3}$$

where both F_i and F_j took values from F_1–F_n, the fitnesses for each desired focus. The inverse form favors maximizing all objecties at the same time because its value is limited by the smaller of all fitness values. Also, the difference term $|F_i - F_j|/(F_i + F_j)^2$ further biases the function output towards the solutions with even performances because this term lowers the overall fitness value whenever F_i and F_j are different. This difference term is divided by the $(F_i + F_j)^2$ to so that each nomralized term will be bounded in magnitude by $1/|F_i + F_j|$. To demonstrate how this inverse-form function solved the Pareto problem, we compared the inverse fitness function with the direct summation in the same a two-criterion optimization problem with Figure 2.5a. In this specific example, Equation 2.3 was defined as:

$$F^{-1} = {F_1}^{-1} + {F_2}^{-1} + |F_1 - F_2|/(F_1 + F_2)^2 \tag{2.4}$$

where F_1 and F_2 are the fitness values for the two criteria, respectively. **Figure 2.5b** shows the overall fitness calculated by inverse summation including the cross difference terms. In contrast to the direct fitness forms, optimizations using the inverse fitness function were biased towards the balanced objective values because the inverse fitness evaluated (by Equation 2.4) along contours of constant $F_1 + F_2$ always took the maximum value at the diagonal line. Therefore, the OLEA calculations using Equation 2.4 preferred the solution space around the $F_1 = F_2$ line more than others and were more likely to reach output with balanced optical intensity at the two foci.

Figure 2.6 depicts the multifocal lattice structures of TiN nanoholes optimized using the direct and inverse forms of fitness functions and the corresponding far-field profiles calculated by FDTD. Both

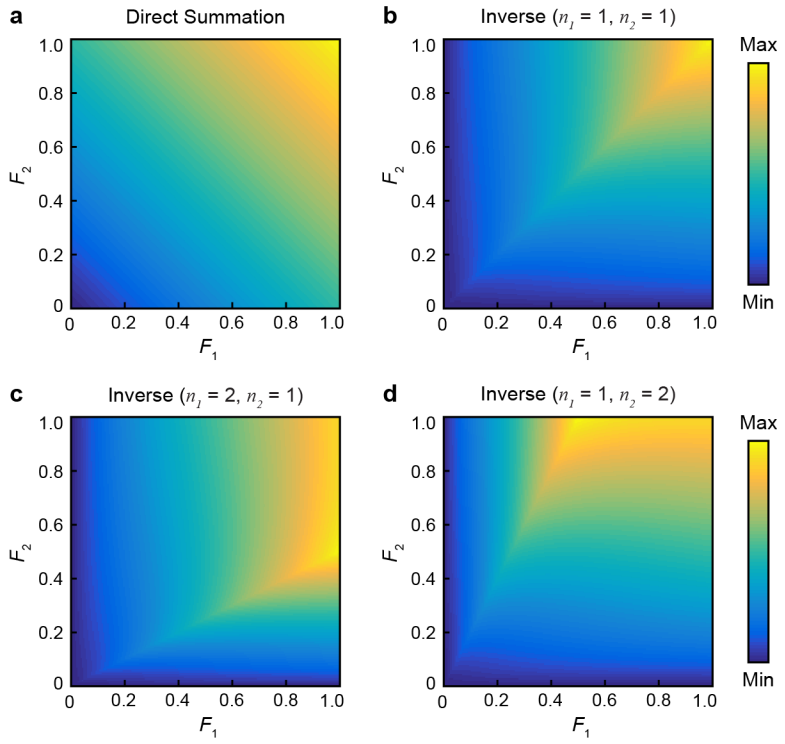

Figure 2.5. Overall fitness value as a function of the performances at two criteria calculated using (**a**) direct summation (Equation 1.6), (**b**) inverse summation including the cross difference term (Equation 2.4), (**c-d**) inverse fitness function with different normalization factors n_1 and n_2 (Equation 2.5).

fitness functions (Equations 1.6, 2.3) produced the desired focal points with similar intensities when the spots were placed at similar distances from the lattice center (Figure 2.6a). Conversely, obtaining the same focal intensity at very different heights from the lens surface was challenging because numerical aperture (NA) decreases with increasing focal distance. Multifocal lenses designed by the traditional fitness function (Equation 1.6) produced stronger light spots at shorter focal distances (Figure 2.6b,c, left). In contrast, all OLEA calculations using the inverse fitness function converged to solutions with balanced focal intensities (Figure 2.6b,c, right).

Independent tuning of optical intensity at each focal point was further achieved by a generalized form of this inverse function:

$$F^{-1} = (F_1/n_1)^{-1} + (F_2/n_2)^{-1} + |F_1/n_1 - F_2/n_2|/(F_1/n_1 + F_2/n_2)^2 \tag{2.5}$$

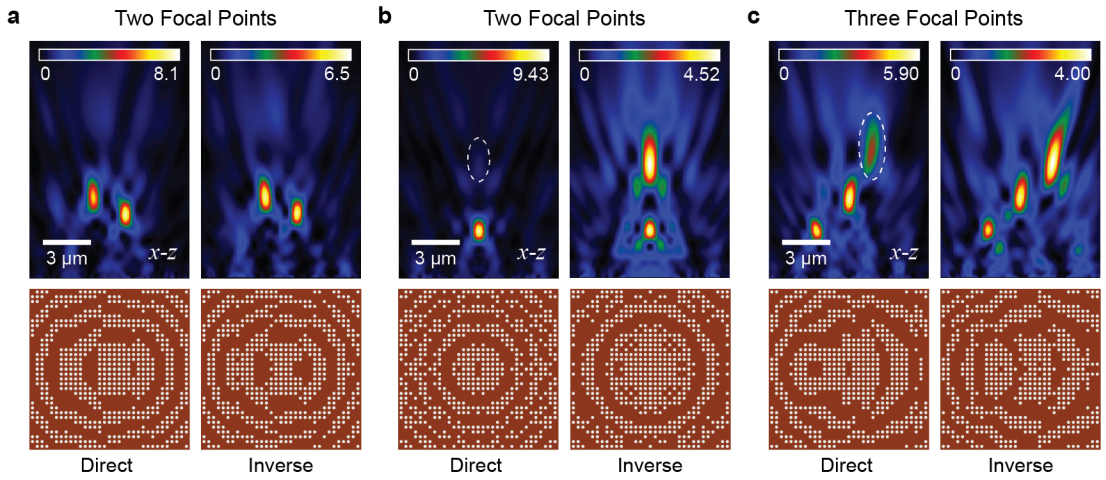

Figure 2.6. Calculations using the inverse fitness function can produce balanced intensity at all light points. Schemes of lattice lenses optimized based on the (lower left) direct and (lower right) inverse forms and (upper left and right, respectively) the corresponding far-field light profiles. (**a**) Two focal points at $x = \pm 1$ μm, $y = 0$, and $z = 4,\ 5$ μm. (**b**) Two focal points at $x,\ y = 0$, and $z = 3,\ 7$ μm. (**c**) Three focal points at $x = -1,\ 0,\ +1$ μm, $y = 0$, and $z = 4,\ 5,\ 6$ μm. x-z maps of optical intensity were calculated by FDTD simulations at $\lambda = 800$ nm. Lattice spacing $a_0 = 300$ nm. Nanohole diameter $d = 200$ nm.

By normalizing with different constants (n_1 and n_2), the relative magnitude of the fitness values corresponding to each focal point could be adjusted. Therefore, the overall fitness lanscape could be arbitrarily biased to F_1 (**Figure 2.5c**) and F_2 (**Figure 2.5d**) by tuning these normalization constants. **Figure 2.7** shows that the distribution of the optical power can be tailored between two focal points placed at both similar and very different heights from the lens surface. The optimized nanohole patterns could be very different based on the choice of n_1 and n_2 values, but the focal point profiles produced were consistently similar except for the intensity change. Overall, this proposed objective function enabled improved control over individual criteria compared to traditional fitness functions in multiobjective optimization problems. This advance could be beneficial for designing metasurfaces holograms with control not only over the light pattern but also the optical intensity distribution. Evolutionary design allows tailoring of optical patterns and intensities to achieve complex far-field light profiles that cannot be determined analytically by conventional wave-optics principles.

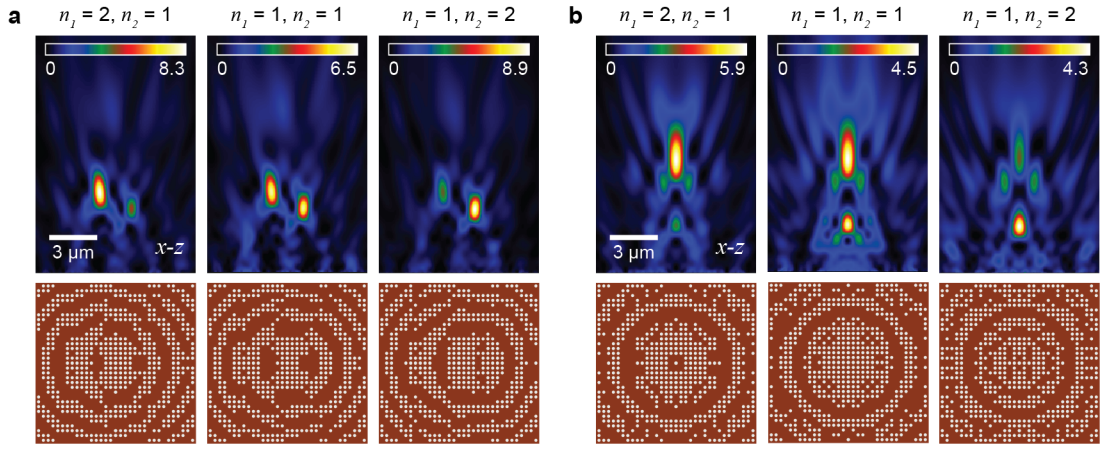

Figure 2.7. Inverse fitness function can be generalized to tune the focus intensity. Schemes of lattice lenses designed using different normalization factors (n_1 and n_2) and the corresponding focal profiles for (**a**) Two focal points at $x = \pm 1$ μm, $y = 0$, and $z = 4,\ 5$ μm. (**b**) Two focal points at $x,\ y = 0$ and $z = 3,\ 7$ μm.

2.2.4. Design robustness to structural imperfections

The nanohole lattices that could be realized experimentally typically deviated from the ideal structures predicted by the simulations. Therefore, it is important to show that the performance of OLEA-designed metasurfaces can tolerate structural defects and that the prototyping process will not require stringent control over nanohole size and shape. We tested the sensitivity of the TiN metasurface performance to imperfections with FDTD calculations. **Figure 2.8** shows the x-z optical profiles calculated for (left) optimized lattice structures, (middle) lattice structures with 20% random bits, and (right) lattices with $\pm 30\%$ random variation in nanohole sizes. The defective lattices exhibited negligible degradation in focusing intensity and light spot patterns and indicated that our TiN metasurface designs can tolerate imperfections.

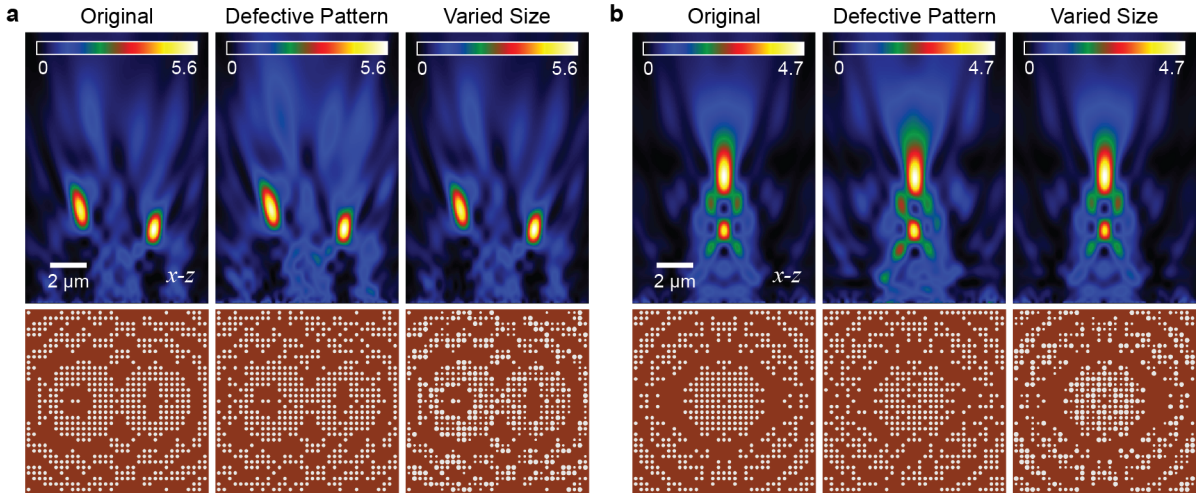

Figure 2.8. The performances of TiN metasurfaces are insensitive to imperfections in lattice patterns and nanohole sizes. (lower) Schemes and the (upper) corresponding x-z optical profiles calculated by FDTD simulations for (left) original optimized lattices, (middle) defective structures with 20% random lattice sites, and (right) lattices with up to ±30% variations in nanohole size. TiN lattices lenses (33 × 33) optimized to focus two focal points at (**a**) $x = \pm 2$ μm, $y = 0$, and $z = 4,\ 5$ μm and (**b**) $x,\ y = 0$ and $z = 4,\ 7$ μm.

2.3. Scalable Prototyping and Experimental Characterization of TiN Lattice Metasurfaces

This section shows a simple technique for parallel production of TiN lattices by (1) using ion-beam milling to define the lattice pattern in a sacrificial materials on top of single-crystalline TiN and (2) selective wet etching of TiN to transfer the pattern. This method was 10-times faster than direct FIB milling and demonstrated the capabilities of tuning the nanohole sizes and shapes. Scanning confocal measurements showed confirmed that the prototyped TiN lattice lenses exhibited the same OLEA-designed optical responses with FDTD simulations.

2.3.1. Masked-etching method for TiN metasurface fabrication

The masked-etching method developed for prototyping nanohole metasurfaces on TiN films was based on a combination of FIB milling and wet etching. **Figure 2.9a** depicts the procedure using a thin Cr layer as an etch mask. Again, single-crystalline epitaxial TiN films were prepared by reactive magnetron sputtering[44] on sapphire substrates (Figure 2.1). A 5-nm Cr film layer was deposited on the TiN films by

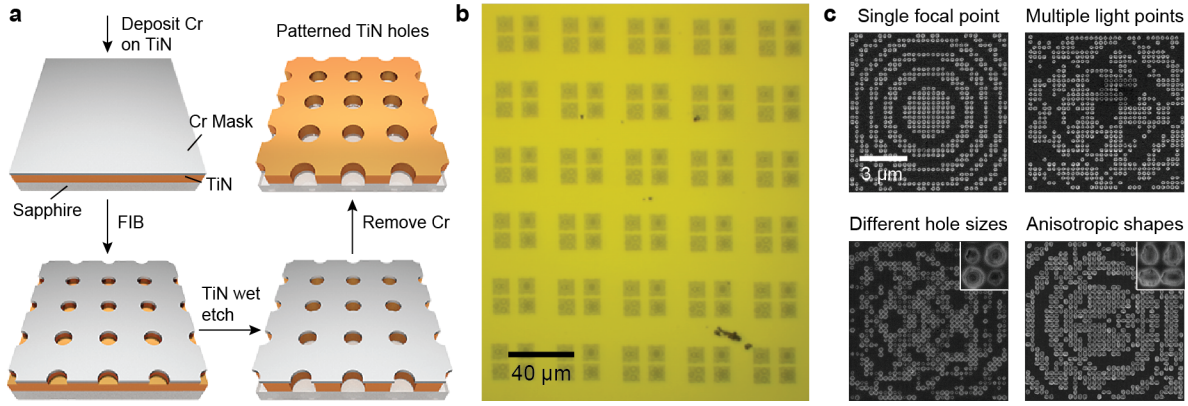

Figure 2.9. Prototyping of TiN lattices over large areas can be achieved by combining ion beam milling with wet etching. (**a**)Scheme of the prototyping technique that combines focused ion beam (FIB) milling and wet etching. (**b**) Optical microscopy image showing 120 lattices patterned in 30 min.(**c**) SEM images of nanohole lattices patterned on TiN with different hole arrangements, sizes, and shapes. Sizes of the two insets in the lower images are 600 nm.

thermal evaporation and patterned with FIB using the patterning files converted from optimized lattices. The design of FIB patterns will be described in details in next subsection. TiN etchant was used to etch the exposed TiN areas so that the pattern on Cr masks was transfered to the TiN layer. Finally, the Cr hole-mask layer was removed by Cr etchant. **Figure 2.9b** shows the optical microscopy image for an array of 120 lattice lenses that can be prototyped in 30 min. In comparison, direct FIB milling in TiN with the same current conditions required over 5 h to pattern the same area.

In comparison, our masked-etching method avoided oversputtering of the sapphire substrate, and the resulting patterns avoided the tapering of FIB nanoholes due to the Gaussian profile [51] of ion beams. To characterize the nanohole shapes produced by the masked-etching process, we made the inverse replicates of nanoholes by molding polyurethane (PU) on the TiN patterns. **Figure 2.10** depicts the PU post arrays cured from TiN nanoholes comopared with the structures generated by direct FIB milling. Characterization of the PU patterns showed that nanoholes produced by our prototype method exhibited flatter bottoms (no etching into the sapphire substrate) and steeper walls than the FIB-milled holes. Also, the direct milling approach required more than 6 times longer processing ties which resulted in severe beam drift, indicated by the undersirable elliptical nanohole shapes.(Figure 2.10)

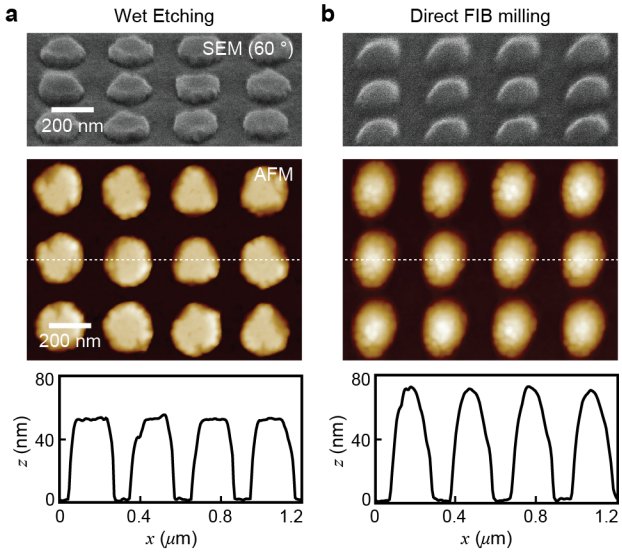

Figure 2.10. Comparison of nanoholes shapes made on TiN by our prototyping method and direct FIB milling by polyurethane (PU) molding. (Upper) angled SEM images at 60°, (middle) AFM maps, and (lower) AFM cross-sections of PU patterns molded from TiN nanoholes made by (**a**) our masked-etching technique and (**b**) direct FIB milling. The ion beams were at a voltage of 30 kV and a current 93 pA in both methods.

2.3.2. Ion-beam pattern designs for size and shape control

Figure 2.9c shows a variety of TiN metasurface structures that can be patterned on a single substrate. Although wet etching is an isotropic process, lattice optics with different hole sizes (Figure 2.9c, lower left) and anisotropic hole shapes (Figure 2.9c, lower right) can be produced by tuning the FIB milling patterns and wet etching times. The ion-beam milling was conducted using the FIB instrument FEI Helios Nanolab. **Figure 2.11a** demonstrates how nanoholes with different sizes and shapes have been encoded to discrete exposure patterns and written to stream files by a MATLAB script.[13] These patterns used a 20-nm spacing for circular holes and a 17-nm spacing for ellipses. To define the patterns on a 5-nm Cr mask, these stream files were executed with 2000 passes with a 5-ms beam dwelling time at 93 pA and 30kV. Typically, a lattice pattern contained 8000 exposure points and could generated in 15 seconds. **Figure 2.11b** shows the transfer of nanohole sizes and shapes from the Cr layer to TiN film after a TiN

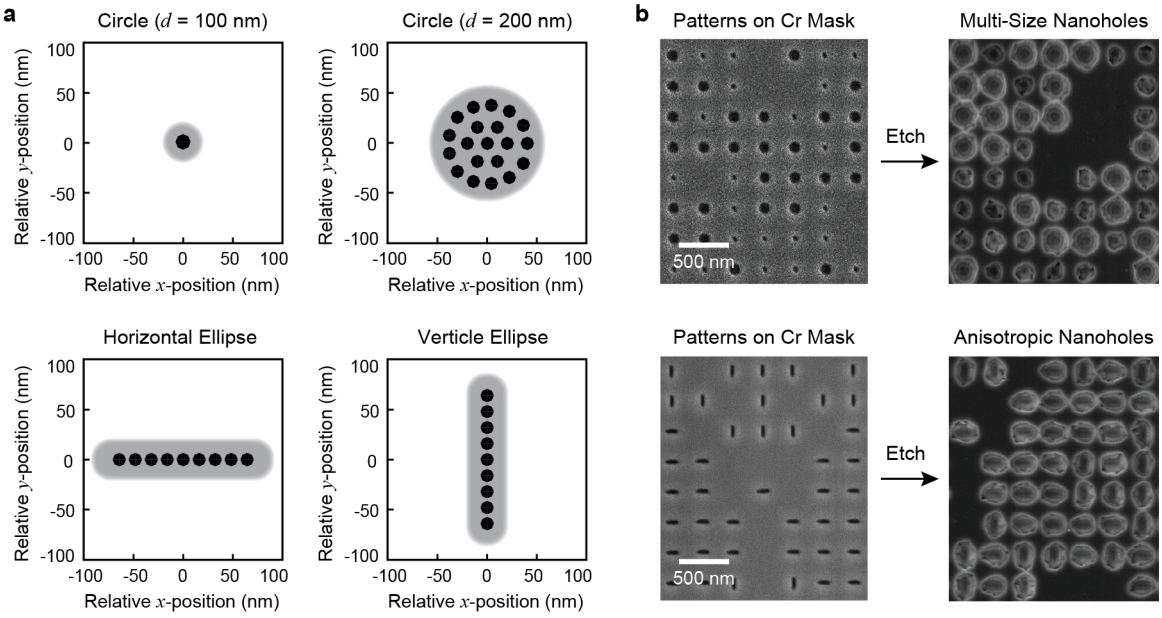

Figure 2.11. TiN nanoholes with different sizes and shapes can be achieved by controlling FIB exposure pattern and wet etching time. (**a**) FIB exposure patterns written in stream files that can create Cr etch masks to generate different TiN nanohole sizes and shapes. (**b**) SEM images of milled nanoholes in (left) the 5-nm Cr mask layers and (right) the TiN nanoholes produced by wet etching.

etching of 5 min at room temperature and a Cr etching of 1 min. During the isotropic etching proces, the nanohole diameters expanded by around 110 nm in both x and y directions.

2.3.3. Scanning confocal microscopy measurements of focal points by TiN metalenses

Figure 2.9c depicts structures of the multifocal metasurfaces produced by our parallel approach and their focusing profiles characterized by scanning confocal microscopy[28,52] using a laser source (λ = 800 nm). These lattices could balance optical intensities at all light spots despite the change in NA at different focal distances. The focal intensities obtained in experiment were *ca.* 3 times lower than that predicted in simulations. We believe that imperfections in the patterning process can result in irregular nanohole shapes as well as increase optical losses. These factors were different from the variation in hole size and arrangements we simulated by FDTD Figure 2.8. For example, the redeposition common to serial ion beam milling[51,53] may have contributed to nanohoe shapes that deviated from perfect circles or ellipses

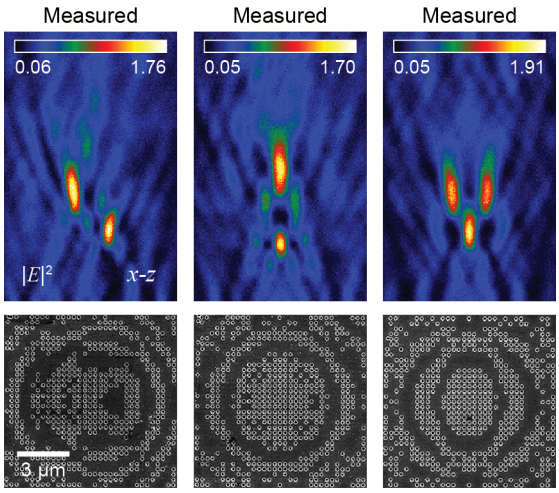

Figure 2.12. TiN lattices with a single hole size can simultaneously focus light to multiple regions. (lower) SEM images of TiN lattice optics and (upper) the corresponding confocal microscopy images ($\lambda = 800$ nm). The lattices were optimized to produce (left) two focal points at $x = \pm 1$ μm, $y = 0$, and $z = 4,\ 6$ μm; (middle) two focal points at $x,\ y = 0$, and $z = 3,\ 7$ μm; (right) three focal points at $x = 0, \pm 1$ μm, $y = 0$, and $z = 4,\ 6$ μm. $a_0 = 300$ nm and $d = 200$ nm.

in the Cr layer (Figure 2.11b); these defects could be subsequently transferred to the TiN film by wet etching (Figure 2.10a).

Both the OLEA design and the fabrication method can be extended to any desired square (rectangular) regions and lattice spacings. **Figure 2.13** demonstrates the flexibility of OLEA in achieving larger lattice sizes by designing a 49×49 array (15 μm $\times$ 15 μm) with the same spacing ($a_0 = 300$ nm). With a larger lattice footprint, the patterned TiN lattice metasurfaces could produce at least four different focal points with drastically different focal distances ($f = 4$, 6, and 10 μm).

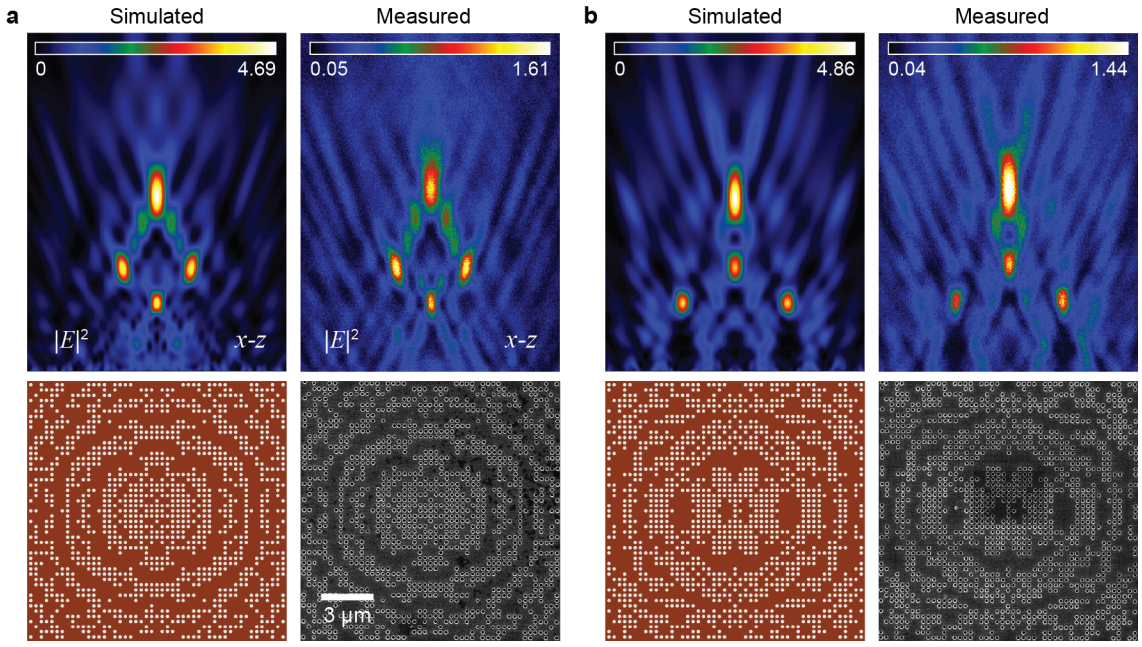

Figure 2.13. Object-oriented lattice evolutionary algorithm (OLEA) can design TiN metasurfaces with flexible lattice sizes. (lower left) Schemes and (lower right) SEM images of TiN lattice optics and the corresponding x-z optical profiles (upper left) calculated by FDTD simulations and (upper right) measured by confocal microscopy. TiN lattices lenses (49×49) optimized to focus four focal points at (**a**) $x = 0,\ \pm 2\ \mu$m, $y = 0$, and $z = 4,\ 6,\ 10\ \mu$m and (**b**) at $x = 0, \pm 3\ \mu$m, $y = 0$, and $z = 4,\ 6,\ 10\ \mu$m. The optical profiles were measured and calculated at $\lambda = 800$ nm. $a_0 = 300$ nm and $d = 200$ nm.

2.4. TiN Metasurfaces for Multiphase and Polarization Sensitive Responses

This section describes the OLEA design of TiN metasurfaces for multilevel and polarization sensitive phase control over the wavefront. Using optical fields calculated by FDTD simulations, the algorithm could solve for multiphase metasurfaces with different nanohole sizes and produce complex optical patterns in 3D with up to five different light spots. We also showed dynamic tuning of the focal profile by changing the polarization of the incident light using anisotropic TiN nanohole shapes. All these designs could be fabricated by the masked-etching method in the previous section and we believe that this optimize-and-prototype platform we established here can contribute to expanding metasurface designs to a wide range of applications requiring unconventional materials systems.

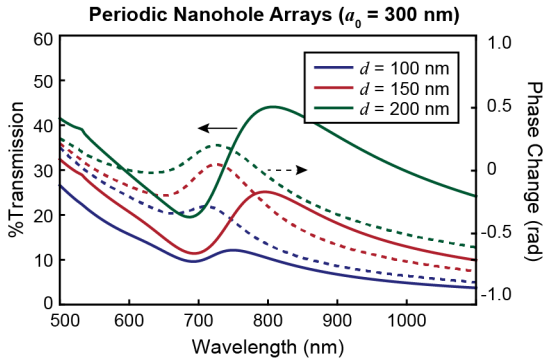

Figure 2.14. Multi-level intensity and phase control can be achieved by tailoring the nanohole sizes. Transmission spectra (solid line) and phase change at different wavelengths (dashed line) calculated by FDTD simulations for periodic array of circular nanoholes with diameters $d = 100$, 150, and 200 nm.

2.4.1. Multiphase metalenses by tuning nanohole sizes

Metasurfaces made from multiple phase elements can achieve improved diffraction efficiency compared to those having a single lattice unit because the inclusion of extra elements enabled additional control over the phase profile. Nanohole lattice lenses using a single hole size, in contrast, primarily operated by intensitiy manipulation[13] while control over the phase profile was less optimized.[28] **Figure 2.14** shows the different phase changes that can be obtained from nanohole arrays with constant spacing ($a_0 = 300$ nm) by tuning hole sizes ($d = 100$, 150, and 200 nm). The phase coverage by the three hole sizes was only around $\pi/4$ so the TiN lenses were not comparable to the state-of-art dielectric metalenses[9] in terms of their efficiency. However, we will show that this extra tunability can enable new design capabilities for the OLEA.

The OLEA is flexible on using any number of phase elements as the lattice units. To obtain lattice lenses with the three hole sizes shown in Figure 2.14, we exported the electric field components of the light transmitted through each of the nanohole and input these data to OLEA before optimization started. **Figure 2.15** shows the multiphase lattice structures designed using these three units and the corresponding far-field profiles calculated by FDTD simulations. To simplify the data collection process, we used the OLEA to solve for focal spots on $z = 5$ μm plane above the TiN surfaces. The calculated focal points exhibited balanced intensities in all the three patterns. We expect that further extension of

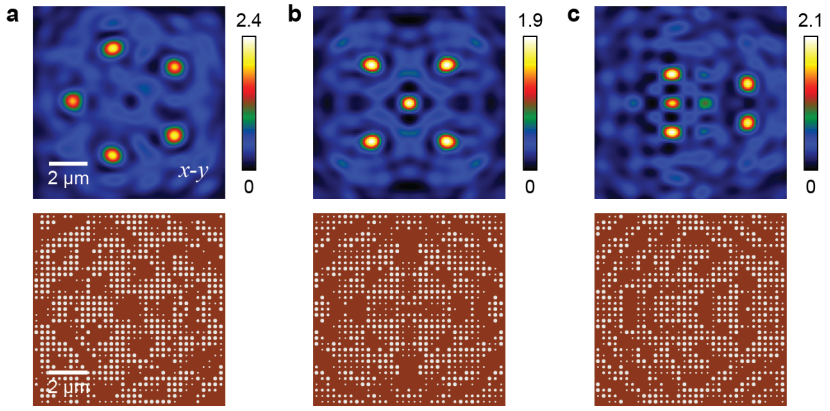

Figure 2.15. Lattice metasurfaces with three phase elements can realize a range of optical profiles. (upper) Simulated optical profiles at $z = 5$ μm, and (lower) schemes for the corresponding multiphase TiN lattice lenses designed for obtaining (**a**) five focal points arranged 3 μm from the center, (**b**) focal points at $x = \pm 2$ μm, $y = \pm 2$ μm and one focal point at the center, and (**c**) points at $x = -1$ μm, $y = 0, \pm 1.5$ μm and two points at $x = 3$ μm, $y = \pm 1$ μm.

phase coverage to the $0 - 2\pi$ range can help improve the focal intensity and decrease the background optical power.

Experimentally, we demonstrated a 2-level phase control using two hole sizes: $d = 100$ and 200 nm (represented by 01 and 10, respectively). **Figure 2.16** depicts the multiphase lattices designed for five focal points, which were situated on the $z = 5$ μm plane for simplicity in experimental imaging. The $x - y$ light profiles measured by confocal microscopy (Figures 2.16a,b, upper right) for the prototyped structures were in good agreement with 3D patterns of light spots calculated by FDTD simulations and visualized by Paraview (Figures 2.16a,b, left). Therefore, the accuracy of our masked-etching patterning technique was verified. As expected, the light intensities at the measured foci were lower than those produced by 2- or 3-foci metasurfaces because the optical power was distributed over a larger number of spots. To improve the focusing efficiency further, we can in theory include an arbitrary number of phase elements in the OLEA because the method can automatically adjust the digits used to represent each lattice site based on the number of element types. In reality, designs using three nanohole sizes (Figure S9-10) were difficult to fabricated because size control with a precision of 50 nm was challenging with wet etching. Finer size tuning could be achieved by directional dry etching techniques using chlorine

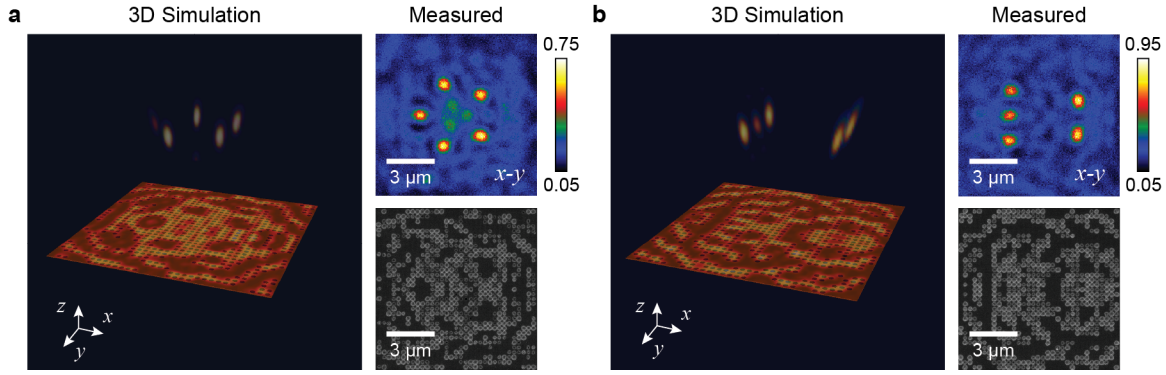

Figure 2.16. The design-prototype technique can realize multiphase metasurface structures. (left) Simulated 3D foci pattern with near-field electric field intensity, (upper right) measured optical profiles at $z = 5$ μm, and (lower right) SEM images for the corresponding multiphase TiN lattice lenses designed for obtaining (**a**) five focal points arranged 2 μm from the center and (**b**) three points at $x = -1$ μm, $y = 0, \pm 1.5$ μm, and two points at $x = 3$ μm, $y = 1$ μm.

plasma.[54] Pritzker Nanofab facilities at University of Chicago, for example, have a inductively coupled plasma etching with chlorine gases.

2.4.2. Anisotropic nanoholes for polarization selective responses

The OLEA could also solve for structures with optical responses tunable by the polarization of incident light by using anisotropic nanohole shapes. We used elliptical hole shapes (major axis $d_1 = 200$ nm, minor axis $d_2 = 160$ nm) that could transmit *ca.* two times more light when polarization was perpendicular to the major axis of the hole (Figure 2.2) The change in nanohole shape shifted the SPP resonance from 800 to 850 nm, where the EOT effect was now maximized. In this design, each lattice site was represented by two binary numbers, with 00, 01, and 10 denoting a closed hole, a vertical ellipse, and a horizontal ellipse, respectively. The OLEA calculated optical profiles for each polarization direction separately and maximized the focal points in both profiles using the overall fitness function Equation 2.3. **Figure 2.17** shows confocal measurement results for optimized TiN lattices of anisotropic nanoholes with incident light in different polarization states. This metalens realized tunable focal points along the optical axis (Figure 2.17a), where the x-polarized light was focused 7 μm above the lattice plane and the y-polarized light to 3 μm. We also showed the shift of light point in both x- and z-directions by switching

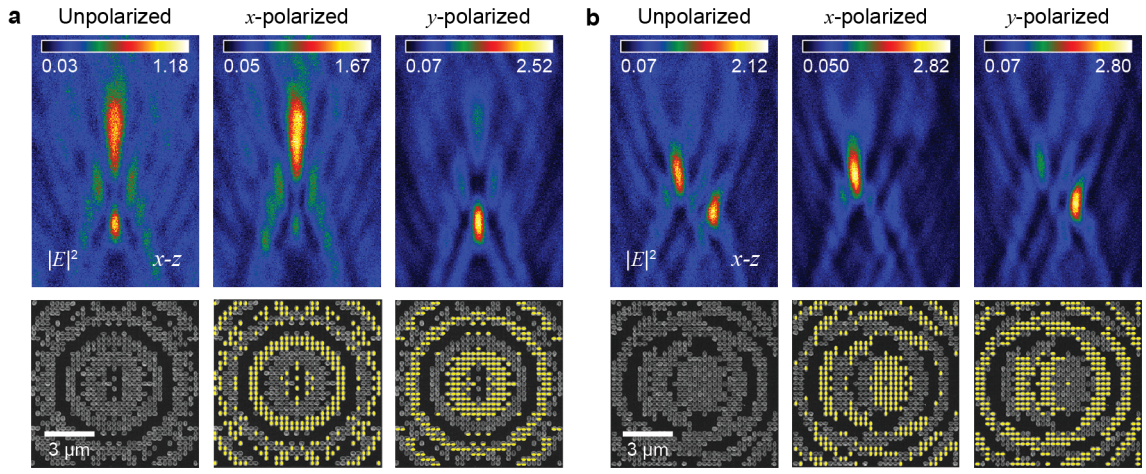

Figure 2.17. TiN lattice lenses can exhibit dynamic optical profiles based on polarization of incident light. Polarization-sensitive TiN lattices with dynamic focal points on $y = 0$ plane at (**a**) $f = 7$ μm while excited in x direction and $f = 3$ μm while excited in y direction, and (**b**) $x = -1$ μm, $z = 6$ μm while excited in x direction and $x = 1$ μm, $z = 4$ μm while excited in y direction. (lower) SEM images of lattice lenses and (upper) confocal microscopy data ($\lambda = 800$ nm). The polarization-sensitive lattices were measured with (left) unpolarized, (middle) x-polarized, and (right) y-polarized light. Nanoholes excited are indicated in white for polarized light, while all holes allow light transmission under unpolarized light.

the polarization state (Figure 2.17b). The measured profiles closely matched the responses predicted by FDTD simulations and verified that our design-and-prototype strategy could use anisotropic element shapes in TiN lattices (**Figure 2.18**). With the ability to account for unit cell shapes, we believe that OLEA can be expanded to design metasurfaces using more complex phase-element structures, such as V-shaped and cross-shaped nanoantennas, for a wider range of applications, including beam steering and negative refraction.

2.5. Summary of OLEA Design of TiN Metasurfaces

In summary, I demonstrated a computational approach and prototyping technique to realize metasurfaces for wavelengths in the near-infrared range with unconventional plasmonic materials. With an inverse-form fitness function designed for multiobjective optimization, the evolutionary method achieved the design of nanohole lattices that could produce arbitrary far-field light patterns with independently tunable intensities. Our masked-etching process could rapidly prototype optimized lattice structures on

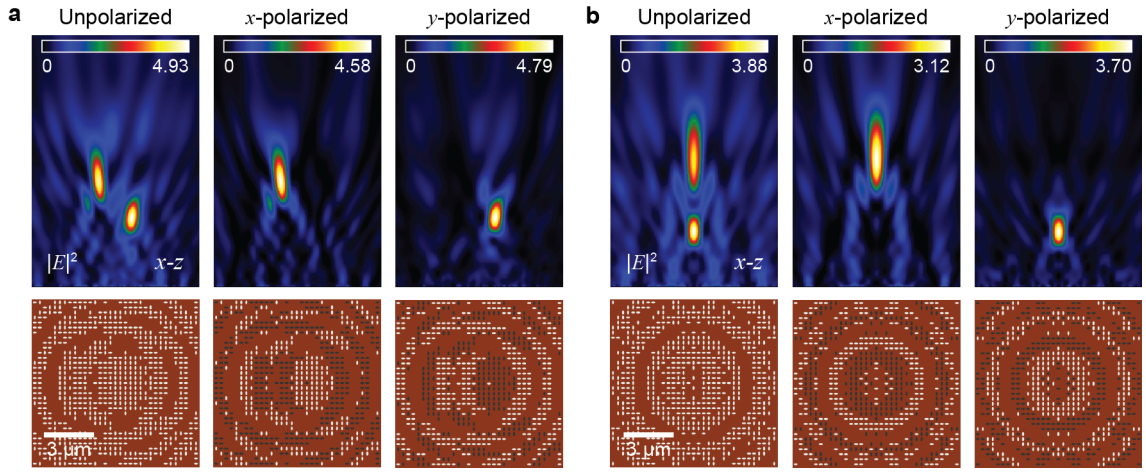

Figure 2.18. TiN lattice lenses can exhibit dynamic optical profiles based on polarization of incident light. Polarization-sensitive TiN lattices with dynamic focal points on $y = 0$ plane at (**a**) $x = -1$ μm, $z = 6$ μm while excited in x direction and $x = 1$ μm, $z = 4$ μm while excited in y direction and (**b**) $f = 7$ μm while excited in x direction and $f = 3$ μm while excited in y direction. (lower) Schemes of lattice lenses and (upper) optical profiles calculated by FDTD simulations ($\lambda = 800$ nm). The polarization-sensitive lattices were measured with (left) unpolarized, (middle) x-polarized, and (right) y-polarized light. Nanoholes excited are indicated in white for polarized light while all holes allow light transmission under unpolarized light.

single-crystalline TiN thin films. I further showed that the design and patterning of TiN metasurfaces with multiple phase elements could produce complex light point patterns. Lattice optics using anisotropic nanohole shapes enabled reversible tuning of optical responses by controlling the polarization state of incident light. I expect that evolutionary design of TiN nanostructures will lead to advances in integrated optoelectronics and durable miniaturized optical metal devices for high temperature operation.

2.6. METHODS

2.6.1. Finite-difference time-domain simulations

FDTD calculations based on commercial software (FDTD Solution, Lumerical Inc.,) were used to simulate the linear properties (far-field and near-field) of TiN nanoholes. The optical constants of TiN were taken from ellipsometry measurements[45] and imported to the materials database of Lumerical FDTD. A uniform mesh size of 2 nm (6 nm) was imposed on TiN nanoholes in simulations for a single nanohole (33×33) lattice structures). The electric fields in x-y direction were recorded and exported by a frequency-domain monitor. The exported fields were imported as a single-wavelength source into a 15 μm $\times$ 15 μm $\times$ 22 μm simulation with a uniform mesh size of 50 nm to calculate the far-field light profiles.

2.6.2. Fabrication of TiN nanohole arrays

Single-crystalline TiN films with 54 nm thickness were deposited on sapphire substrates by magnetron sputtering in 1:1 N_2/Ar environment at 600 $^{\circ}C$ and 0.02 Torr.[44] The patterns of TiN nanoholes were prepared by a combined process of FIB milling and wet etching. A 5-nm Cr layer was deposited on TiN samples by thermal evaporation. Then lattice structures were cconverted to ion beam exposure patterns and written in stream files by MATLAB.[13] The Cr layer was processed by FIB with stream files at a voltage of 30 kV and a current of 93 pA usinga constant exposure time of 5 ms. The patterns were then transferred into TiN by a wet etching of 5 min using Trasene TiN etch at room temperature. The Cr mask layer was removed selective by Transene Cr etch.

2.6.3. Confocal measurements of TiN lattice lenses

A confocal scanning optical microscope (WITec alpha-300) was used to measure the light profiles generated from plane-wave light incident on the lattice lenses.[13] A fiber-coupled super continuum laser (Koheras SuperK Power Plus) with an acousto-optic tunable filter (AOTF, Koheras Spectrack Dual NIR + 4xVIS) and collimator (Thorlabs F280FC-780) were used to generate the collimated incident beam. A polarizer (Thorlabs 10GL08) was used when linearly polarized light was required. The lenses were

measured in air by 100× air objective (Nikon Plan Fluor, NA = 0.90), and transmitted photons were collected by a photomultiplier tube (PMT, Hamamatsu Photonics H8259-01). The PMT tube based on silicon had low sensitivity beyond 820 nm, so the light profiles were measured at $\lambda = 800$ nm for circular holes ($d = 100$ nm, 200 nm) and $\lambda = 820$ nm for elliptical holes ($d_1 = 200$ nm, $d_2 = 160$ nm). The scan resolution was 50 nm using an integration time of 0.01 s/pixel for all measurements.

CHAPTER 3

Plasmonic Lattice Lenses for Multi-Wavelength Achromatic Focusing

This chapter describes an evolutionary approach to design flat multi-wavelength achromatic lenses based on subwavelength plasmonic nanoparticles. Our lattice evolution algorithm achieved desired optical responses by tuning the arrangement of the phase units on a discrete square lattice. Lattice lenses consisting of a single type of nanoparticle could operate at any wavelength in the visible to near-infrared regime (540-1000 nm) by tailoring the localized surface plasmon resonance. When the unit cells were expanded to anisotropic particle shapes, the planar optics could selectively focus light depending on the polarization of incident light. Finally, the algorithm realized efficient multi-objective optimization and produced achromatic lattice lenses at up to three wavelengths (λ = 600 nm, λ = 785 nm, and λ = 980 nm) using multiple different nanoparticle shapes.

Referenced work: J. Hu, C. Liu, X. Ren, L. J. Lauhon, and T. W. Odom, "Plasmonic Lattice Lenses for Multi-Wavelength Achromatic Focusing." *ACS Nano* **2016**, *10*, 10275—10282. DOI: 10.1021/acsnano.6b05855.

3.1. Chromatic Aberrations in Planar Optics

This section introduces the issue of chromatic aberrations in diffractive lenses, where the focal points are broadened in multicolor light beams because the focal lengths are changing with the wavelength of incident light. We will also review existing demonstrations of achromatic lenses and discuss how the our evolutionary algorithm with multiobjective optimization capabilities can potentially achieve achromatic designs over several wavelengths.

3.1.1. Diffractive optics with chromatic aberrations

Diffractive optics are advantageous over their refractive counterparts in a range of applications because of their smaller volume, lighter weight, and lower cost.[55] For example, Fresnel lenses introduced in previous chapters are frequently used instead of biconvex lenses in solar power collection,[55,56] maskless lithography,[57] and projection display illumination.[58] Miniaturized systems can also be realized by replacing bulk optical components with planar alternatives for advances in optical interconnects[59] and integrated optoelectronic systems.[57] However, conventional diffractive lenses consist of concentric annular sections with curved surfaces that are difficult to fabricate at sub-micron scales because of the 3D features. In addition, large chromatic aberrations restrict their performance to a single operational wavelength.[60] Although chromatic aberration can be suppressed at multiple wavelengths by spatial multiplexing,[61–63] this strategy has only been applied to centimeter-scale lenses.

In previous chapters, we reviewed metasurfaces as an emerging class of flat optics[30] that can manipulate light via subwavelength phase elements. These planar structures have been engineered with interesting properties such as anomalous reflection[64] and controlled birefringence[65] and have shown promising results in subwavelength imaging,[9] spectroscopy,[66] and holography.[11,12] In contrast to traditional diffractive lenses, metasurface elements have a constant thickness that considerably simplifies the fabrication. Their 2D structures are determined by (1) calculating the phase change required at each location to obtain the far-field property from analytical equations; and (2) structuring each building block to produce that wavefront change.[30] Chromatic aberration has been suppressed in metasurfaces for one-dimensional (1D) focusing at three wavelengths in the telecommunication range,[67] where the phase elements were

selected to induce the same phase change at the three wavelengths by exhaustively searching through all possible combinations of geometric parameters. In general, however, a brute-force approach is less desirable compared to methods based on search heuristics that have advantages in computational speed [41,68] and can potentially achieve achromaticity in problems that require more design variables, including lenses for high resolution 2D imaging [9] and waveplates that enable complete phase/polarization control. [25]

3.1.2. Lattice evolution algorithm for designing achromatic metalenses

Previously, we reported the lattice evolution algorithm (LEA) as an efficient approach to design flat optics based on subwavelength hole arrays in a gold film. [13] In contrast to metasurface design by analytical equations, LEA represents the desired optical property by a fitness function and uses a genetic algorithm to find the structure with the optimized fitness value. The algorithm constrains the phase units to a 2D square lattice, which simplified the optimization problem to the choice of opening or closing a hole at each grid point. Because evolutionary algorithms allow multiobjective optimization, [42,43] a large variety of optical responses were realized from the same grid area simply by tuning the arrangement of nanoholes, including multi-point focusing in 3D and dynamic switching of focal point with incident polarization. A disadvantage of nanohole unit cells, however, is that they only allow the transmission of light within a limited wavelength range that depends primarily on the lattice spacing. [13] Also, the transmission efficiencies (fraction of optical power transmitted through the lattice) of nanohole lattices were limited to 10% - 20%, [13] lower than particle-based metasurfaces. [9,12]

3.2. Single-Phase Metalens Designs for Visible to Near-Infrared Wavelengths

This section describes the design of metalenses based on a single type of plasmonic NP, where the operating wavelength is determined by the localized surface plasmon (LSP) wavelength. The LEA used finite-difference time-domain (FDTD) simulations to calculate the optical fields from each NP and realized metalenses that could operate over a wide wavelength range(λ = 540-1000 nm) by tuning the size and shape of the lattice units. Using rod-shaped NPs as the building units, the lattice lenses exhibited selective focusing based on the incident polarization.

3.2.1. FDTD simulations for plasmonic nanoparticles

We tailored light at different wavelengths using plasmonic NPs with matching LSP wavelengths. Therefore, simulation methods were required to predict the plasmon resonances of NPs based on their size and shape. **Figure 3.1** summarize the simulation setups to study isolated particles or finite-numbers of particles and periodic structures. The total-field scattered-field (TFSF) source was used to calculate the optical spectra from a single particle or 5×5 particle arrays (Figure 3.1a). For this setup, perfectly matched layers (PMLs) were used in $\pm x$, $\pm y$, $\pm z$ directions and 2-nm mesh was used for Au NPs. The electric fields recorded by the total field monitor was imported as a source in the larger FDTD model with 50-nm mesh size (Figure 3.1c). To be used by LEA, these field data were exported in separated files for the six components: the imaginary and real parts of Ex, Ey, and Ez. To calculate the transmittance of lattice lenses, a plane wave source with periodic boundary condition (PBC) in x-y directions and PMLs in the z direction (Figure 3.1b). We used 6-nm mesh size for the particle lattices and a 2D monitor to record the transmitted electric fields. To calculate the light profiles focused by lattice lenses, we imported the fields as a source in the FDTD set-up and the 3D monitor recorded the light intensity in the entire simulation (Figure 3.1c).

The Au NPs induced both an intensity and a phase change in the transmitted light near the LSP resonance. However, the phase change over wavelengths all exhibited Fano line-shapes near the LSP resonance, and the change in phase was trivial compared to the change in intensity. We found that the resonance wavelengths of NP arrays were blue-shifted compared to isolated particles because of coupling

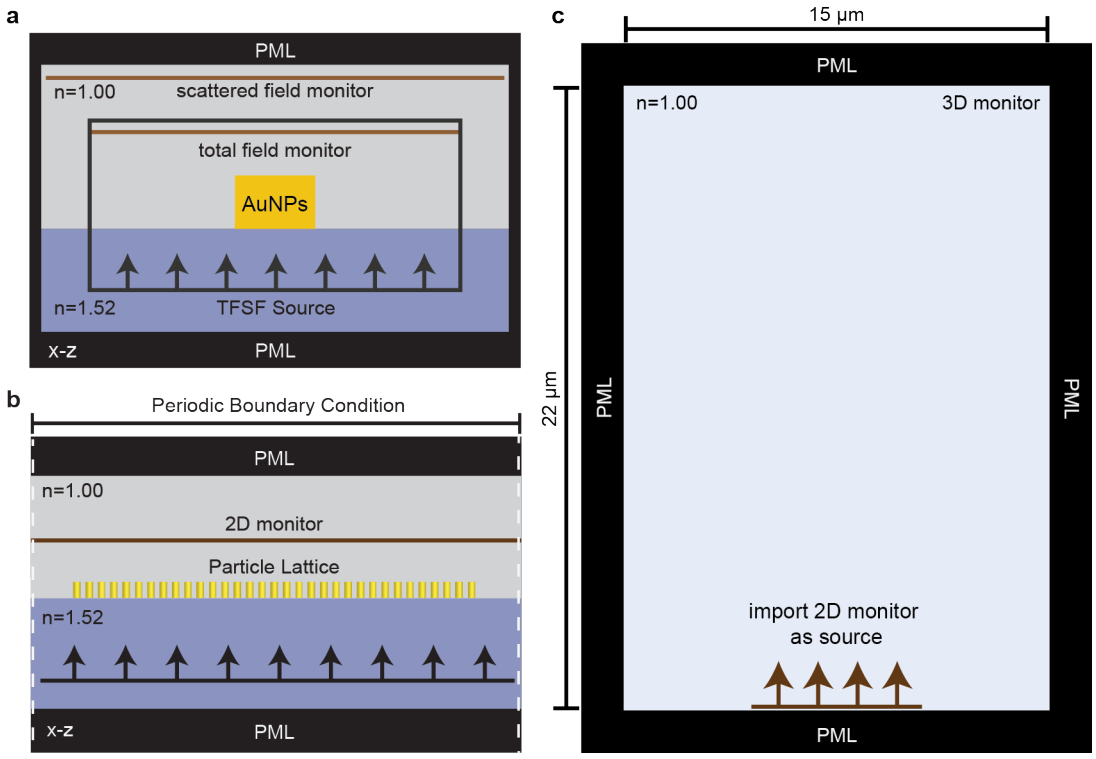

Figure 3.1. Schemes depicting the FDTD simulation setups. (**a**) Near-field calculation of transmission through a single NP or 5×5 array of NPs using a total-field scattered-field (TFSF) setup. (**b**) Near-field calculation of transmission through a full NP lattice. (**c**) Far-field simulation of how the fields that transmit through nanostructures propagate in the long distances.

between NPs and thus could not be predicted from single-particle scattering spectra. Because the coupling depended in part on the arrangement of NPs, periodic lattices had different resonance wavelengths from lattice lenses. The spectra of 5×5 NP arrays, however, were found to be a close approximation to that of random lattices and optimized lenses and were used to select NP responsesFor fabrication simplicity, we chose three Au NPs with the same height $h = 40$ nm: NP1 (cylinder, radius $r = 50$ nm), NP2 (rod, length $l = 165$ nm, width $w = 60$ nm), and NP3 ($l = 212$ nm, $w = 40$ nm). **Figures 3.2a-b** depict the calculated transmission spectra for the 5×5 arrays and 33×33 random lattices (spacing $a_0 = 300$ nm) of NP1-NP3. These particle arrays had LSP wavelengths at $\lambda = 600$ nm, 785 nm, and 980 nm, respectively, which were selected to match the laser sources on the confocal microscope.

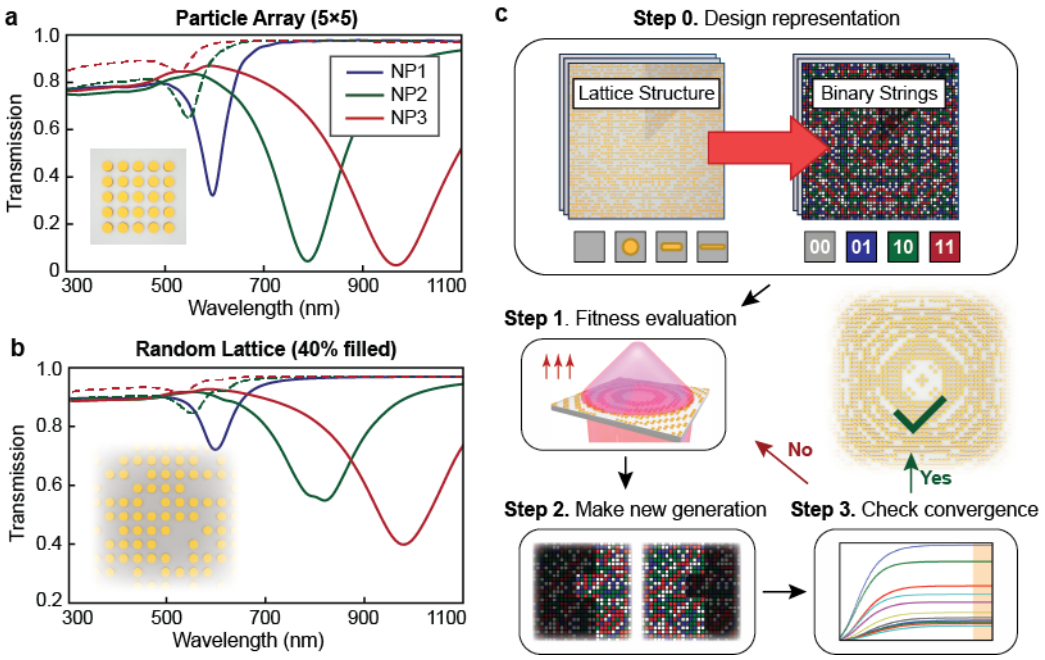

Figure 3.2. Evolutionary algorithms can be used to design Au nanoparticle (NP) lattice lenses with multiple localized surface plasmon (LSP) resonances. Transmission spectra of (**a**) 5×5 arrays and (**b**) 33×33 random lattices of selected lattice elements NP1 (disk), NP2 (rod), and NP3 (rod). (**c**) Scheme describing the steps in the LEA. The dimensions are: radius $r = 50$ nm, lengths $l = 165$ nm and width $w = 60$ nm, and length $l = 212$ nm and $w = 40$ nm for NP1, NP2, and NP3, respectively, with array spacing $a_0 = 300$ nm in (a)(b) and the height $h = 40$ nm. Spectra are calculated by FDTD simulations.

Figure 3.3 shows the FDTD calculated scattering spectra of a single NP and the transmission spectra from a periodic lattice (NP1-NP3). Due to coupling between nanoparticles, the resonance wavelengths of the periodic lattices ($a_0 = 300$ nm) blue-shifted from the LSP depicted by single-particle spectra. We observed increased spectral shift with increasing NP size. The increased coupling can be explained by the decreased separation between particles with a fixed lattice spacing as NP size increased. To increase the efficiency of the calculations, we stored the electric field components extracted from FDTD simulations for NP1-NP3. Instead of simulating the entire lattice structure, we calculated the far-field optical profiles by superimposing the field components transmitted through each lattice point.[13] Unlike traditional metasurface design methods based on wave-front engineering, our numerical approach could

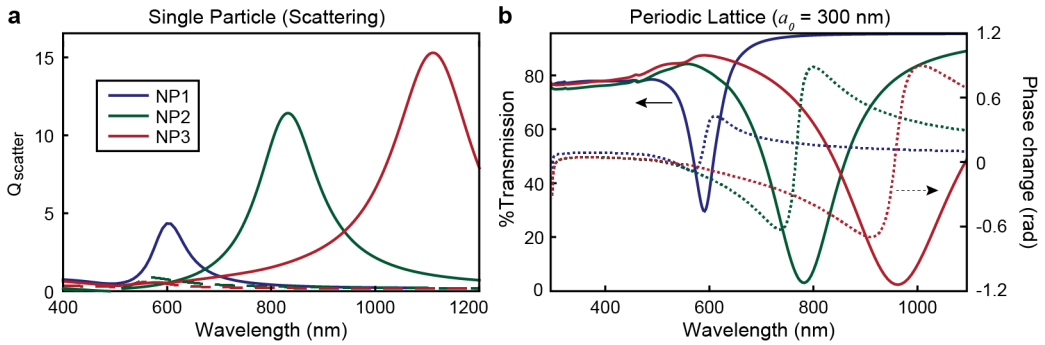

Figure 3.3. The localized surface plasmon resonances of Au NP lattices are shifted due to the coupling between NPs. (**a**) Single particle scattering efficiency and (**b**) Transmission spectra (solid line, left axis) and relative phase change (dotted line, right axis) for periodic lattices of NP1, NP2, and NP3. Scattering efficiency was obtained by the scatter box analysis group in Lumerical using the setup presented by Figure 3.1a. Transmission spectra of periodic lattices were calculated with a setup similar to Figure 3.1b, but using a simulation size $a_0 = 300$ nm with only one particle in the simulation. The phase changes were obtained by subtracting the phase of transmitted light through NPs by the phases at the same location without the NPs.

account for abrupt phase and intensity changes by the plasmonic NPs by explicitly using the real and imaginary components of the electric fields.

3.2.2. LEA calculations for a single focal wavelength

Figures 3.2c summarizes the main three steps of the LEA after initialization with a population of random structures. First, the LEA evaluated a fitness function by calculating the far-field profile of lattices in the current population (step 1). The next generation was then created by giving the fitter structures a larger probability to survive and duplicate (step 2). Third, convergence criteria were checked and terminated if they were satisfied (step 3).[13] Since the specific objective in this work is to achieve achromatic focusing at a single focal point, we could speed up the calculations by imposing an eight-fold symmetry on the lattice structure. We used FDTD simulations with the setup in Figure 3.1 to select the NPs so that the LSP resonance of their lattice matched the desired working wavelength of the lenses. We also calculated the electric components of the transmitted light from each NP and stored them for LEA calculations.

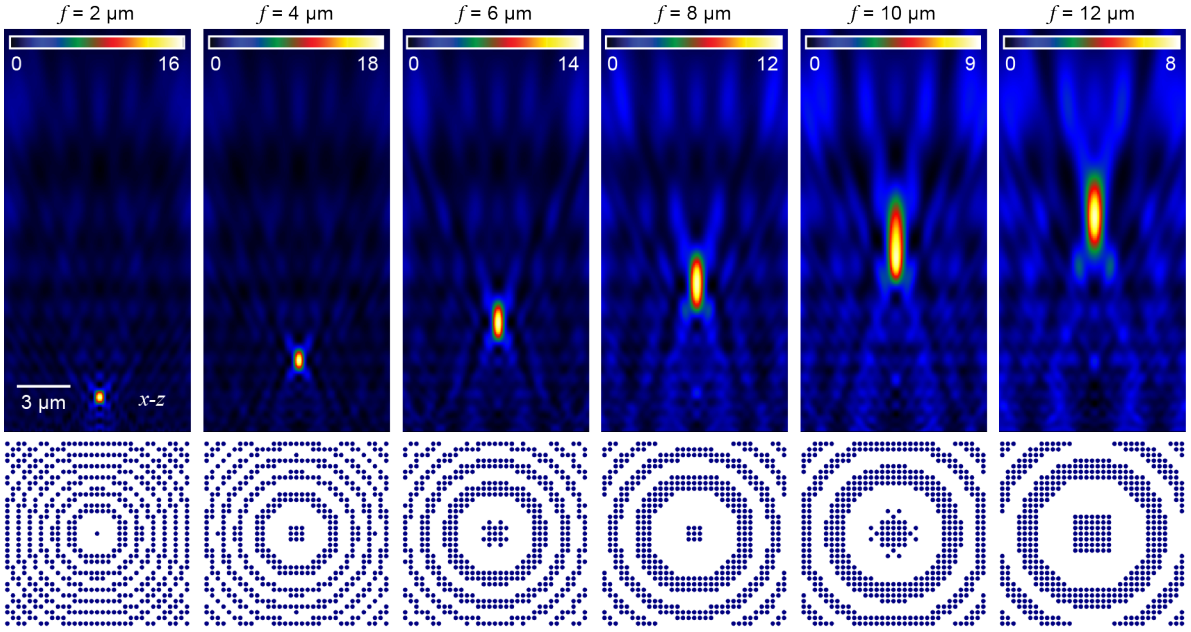

Figure 3.4. Lattice lenses with different focal distances designed by LEA. The focal distance f can be tuned from 2 to 12 μm at wavelength $\lambda = 600$ nm simply by changing the arrangement of the particles on a 10 μm $\times$ 10 μm grid with spacing $a_0 = 300$ nm. The phase element used was NP1, a Au nanodisk with height $h = 40$ nm and radius $r = 50$ nm.

The first LEA calculations focused on a single phase element and lattice consisting of 33 $\times$ 33 elements on a 10 μm $\times$ 10 μm square array to compare with lattice lenses based on nanoholes.[13] Again, the fitness function was defined as Equation 1.5:

$$F(\Delta f) = \frac{I}{\Delta f + c} \tag{3.1}$$

where F was the fitness value, I was the intensity at the desired focal point, Δf was the deviation between the desired and actual focal points, and c was a positive constant.

Figure 3.4 shows the preliminary NP lattice lenses designed for $\lambda = 600$ nm and the corresponding focal point profiles calculated by FDTD simulations. The calculations using this fitness function could produce focal distances up to 12 μm that were comparable to nanohole metalenses with the same footprint.[28,69] For an operating lens wavelength $\lambda = 600$ nm, the FWHM of the focal points increased and the intensity decreased as the focal distance increased (numerical aperture NA decreased). Meanwhile, the

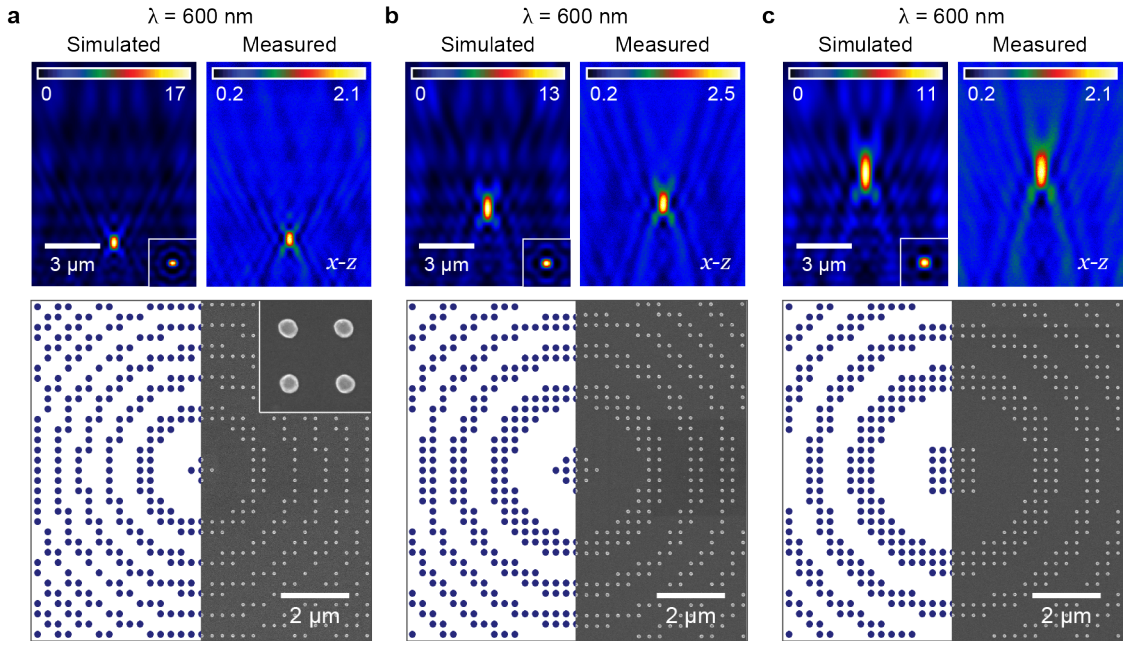

Figure 3.5. Lattice lenses made of NP1 can focus light at its LSP resonance wavelength. (upper left) Simulated and (upper right) measured light profiles are shown for (lower) each lattice structures optimized for a focal distance of (**a**) $f = 3$ μm, (**b**) $f = 5$ μm, and (**a**) $f = 7$ μm. Insets of upper profiles: x-y cross-sections (3 μm $\times$ 3 μm) depicting the light intensity map at focal planes. The box size of the inset (lower) in (a) is $\lambda = 600$ nm. Intensity values are normalized by the incident beam.

depth of the focusing significantly increased with focal length, similar to diffractive lenses reported.[13,28] We concentrated on focal lengths from 3 to 7 μm because their high numerical aperture (NA) between 0.85 and 0.58 cannot be easily accessed with refractive microlenses.[70] The optimized structures were fabricated by EBL on a glass substrate coated with 2-nm Ti as a conduction layer. Confocal scanning optical microscopy[52] was used to map the 3D optical fields of the lenses.

Figure 3.5 depicts the configurations of disk-shaped NP1 lattices and the corresponding far-field profiles optimized for three different focal lengths ($f = 3$, 5, and 7 μm) at $\lambda = 600$ nm. The focal length and intensity patterns in all measured profiles matched the computational prediction. The LEA results were also validated by the resemblance of the NP configurations in the lattice lenses to Fresnel lenses.[69] **Figure 3.6** shows the deleterious effect of the Ti film needed in the EBL process on the performance of the lenses. The Ti introduced prominent plasmonic losses that reduced the scattering efficiency of

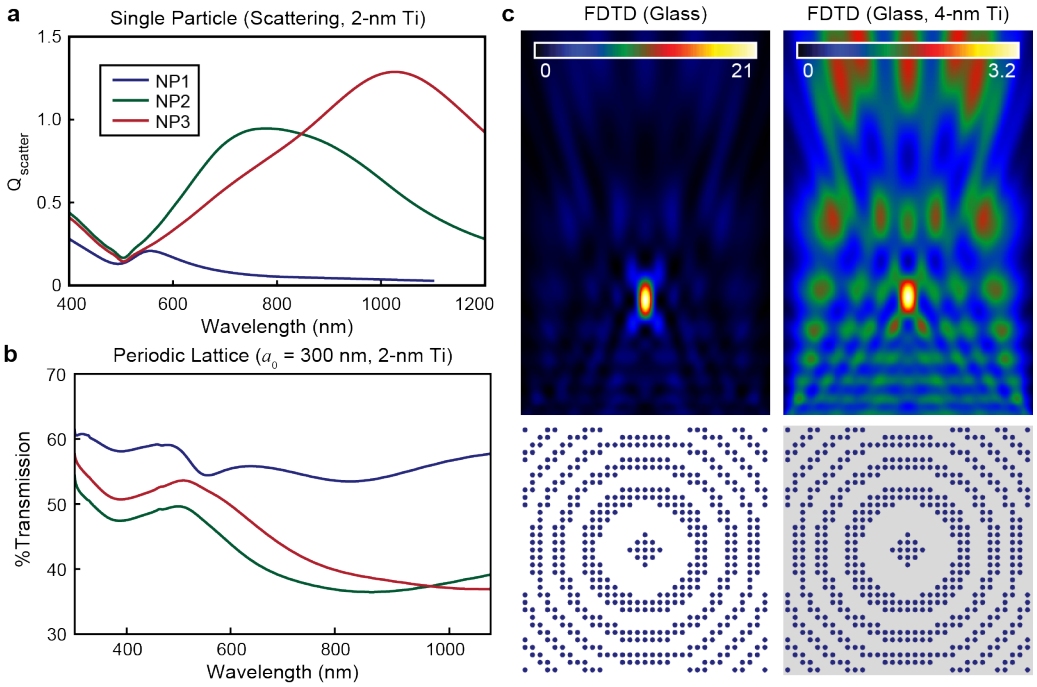

Figure 3.6. Ti conduction layer lowers the quality of LSP resonances and the performance of lattice lenses of NPs. (**a**) Transmission spectra from periodic lattice and (**b**) single particle scattering efficiency of NP1-NP3 on a glass substrate with 2-nm of Ti layer. (**c**) Calculated FDTD light profile for the same lattice lens on (left) glass and on (right) glass with 4 nm conduction layer. Full lens simulations used 4-nm of Ti layer since the simulation size did not allow $>$ 4 nm mesh size.

the NPs (Figure 3.6a-b) and resulted in a more than 6-fold decrease in focusing intensity (Figure 3.6c). Therefore, the measured light profiles had lower focusing efficiency and higher background noise compared to simulations primarily due to fabrication limitations and not the inaccuracy of the design process. This deleterious effect could be alleviated by either depositing Ti on top of the electron-beam resist or using variable pressure EBL.[71]

3.2.3. Nanorod lattice units for polarization selective focusing

Lattice optics consisting of anisotropic plasmonic nanostructures exhibit polarization-sensitive responses not possible in conventional diffractive optics such as dynamic focal tuning.[13] As a proof-of-concept demonstration, we designed and fabricated nanorod (NR) lattice lenses that selectively focused light

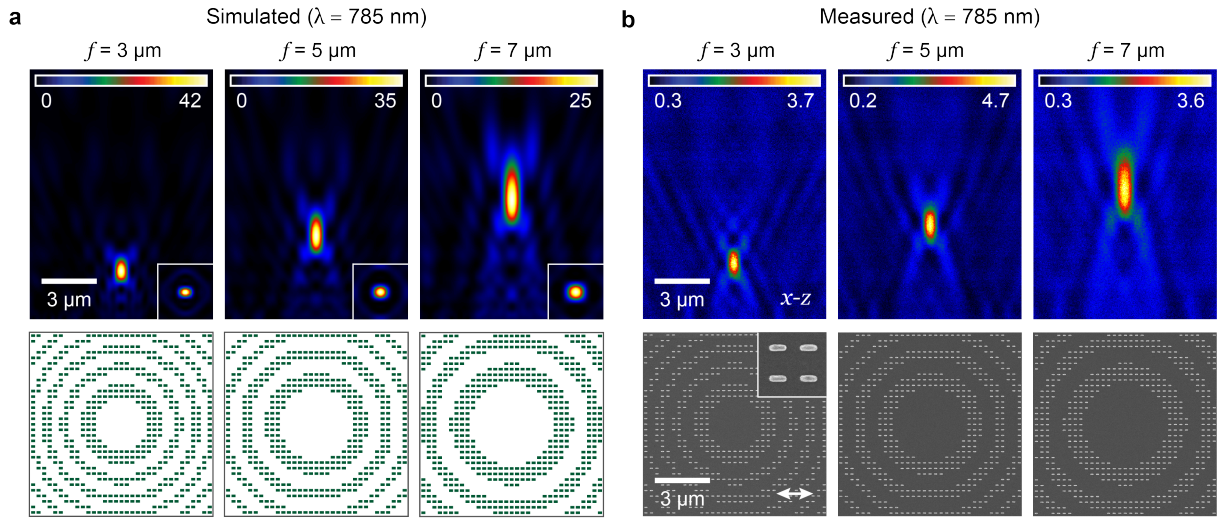

Figure 3.7. Lattice lenses of Au NRs can focus light polarized in the longitudinal direction. (**a**) Schemes of NP2 lattices (lower) optimized for different focal distances at $\lambda = 785$ nm and the far-field profiles (upper) in x-z calculated by FDTD simulation. Insets: x-y cross-sections (3 μm $\times$ 3 μm) depicting the light intensity map at focal planes at $f = 3$, 5, and 7 μm, respectively. (**b**) (lower) SEM images of NP2 lattices shown in (a) and (upper) the focusing profile measured by scanning confocal microscope. Intensity values are normalized by the incident beam.

based on polarization. **Figure 3.7** shows configurations of NP2 lenses for focal lengths of 3-7 μm at $\lambda = 785$ nm and corresponding optical profiles obtained from polarized light. Again, the measured results matched the simulation for all these focal distances, and the spot size increased with focal distance, similar to the trend in NP1 lenses. **Figure 3.8** illustrates that at $\lambda = 785$ nm, these NR lattices only focused transverse-electric (TE) light, where the polarization was aligned with the major axis of the NRs. Transverse-magnetic (TM) polarized light was almost unchanged because the optical scattering by the transverse plasmon mode of the NP2, which had a resonance at 545 nm, was negligible at $\lambda = 785$ nm (Figure 3.2b, Figure 3.3). **Figure 3.9** shows that these lenses could also focus light of $\lambda = 545$ nm polarized in the transverse direction of the NRs. The focus intensity was 5-fold weaker because the scattering efficiency of the transverse plasmon resonance was 10 times lower than the longitudinal mode (Figure 3.3). In addition, the focal lengths observed at $\lambda = 545$ nm were larger than those measured at $\lambda = 785$ nm as expected from chromatic aberration of diffractive optics.[8,60,63]

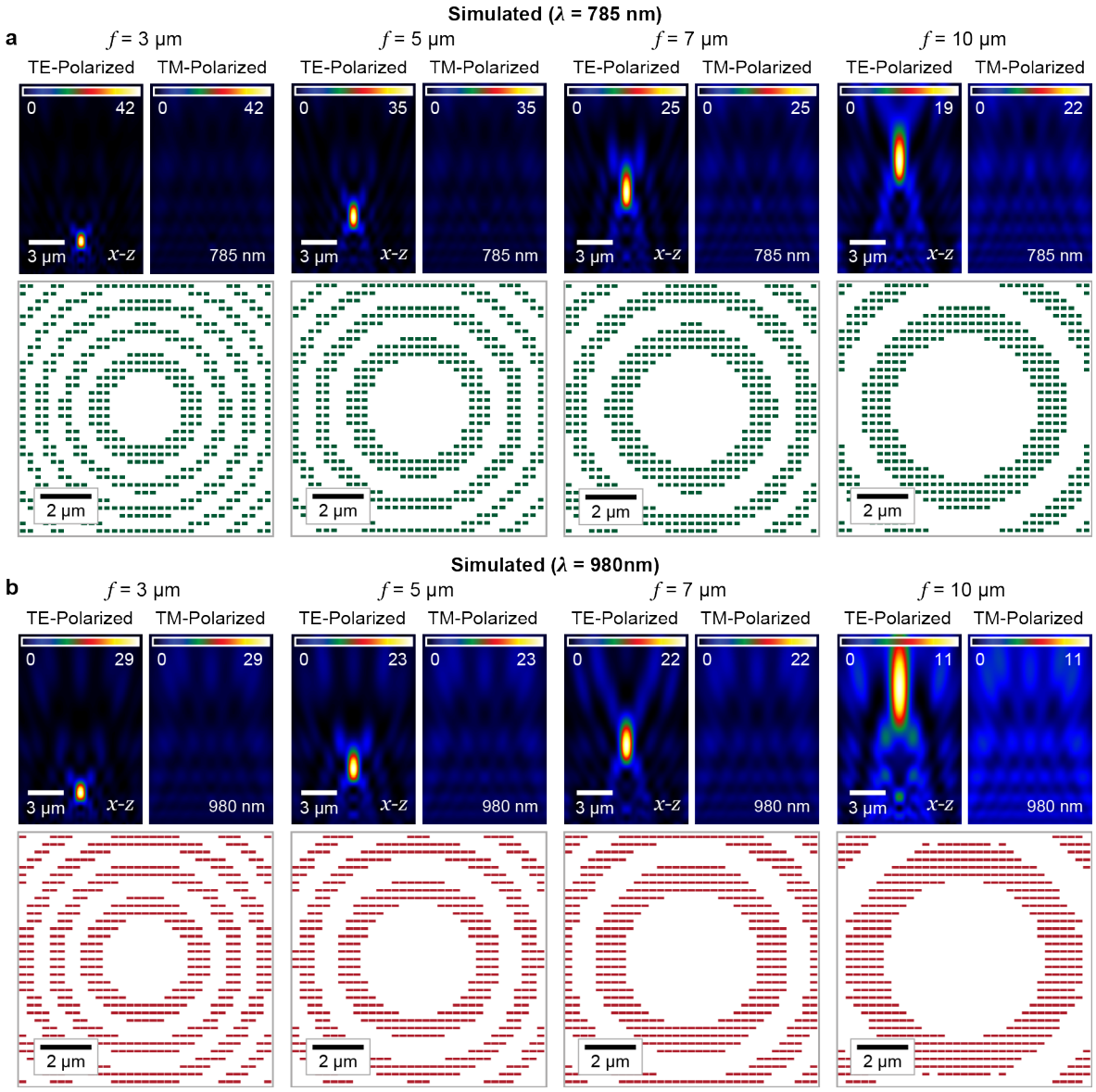

Figure 3.8. Lattice lenses of nanorods (NRs) can selectively focus light polarized in the longitudinal direction. Simulated far-field profiles (upper) and schemes for lattice structures of (**a**) NP2 optimized at $\lambda = 785$ nm and (**b**) NP3 optimized at $\lambda = 980$ nm for focal distances ranging from 3-10 μm excited with different polarization.

We achieved dynamic switching of focusing at a longer wavelength $\lambda = 980$ nm by modulating the polarization in NP3 lattices (Figure 3.8b) with the same algorithm used for NP1 ($\lambda = 600$ nm) and NP2 ($\lambda = 785$ nm) lenses. Around the lower wavelength limit of the Au system, the LEA also solved

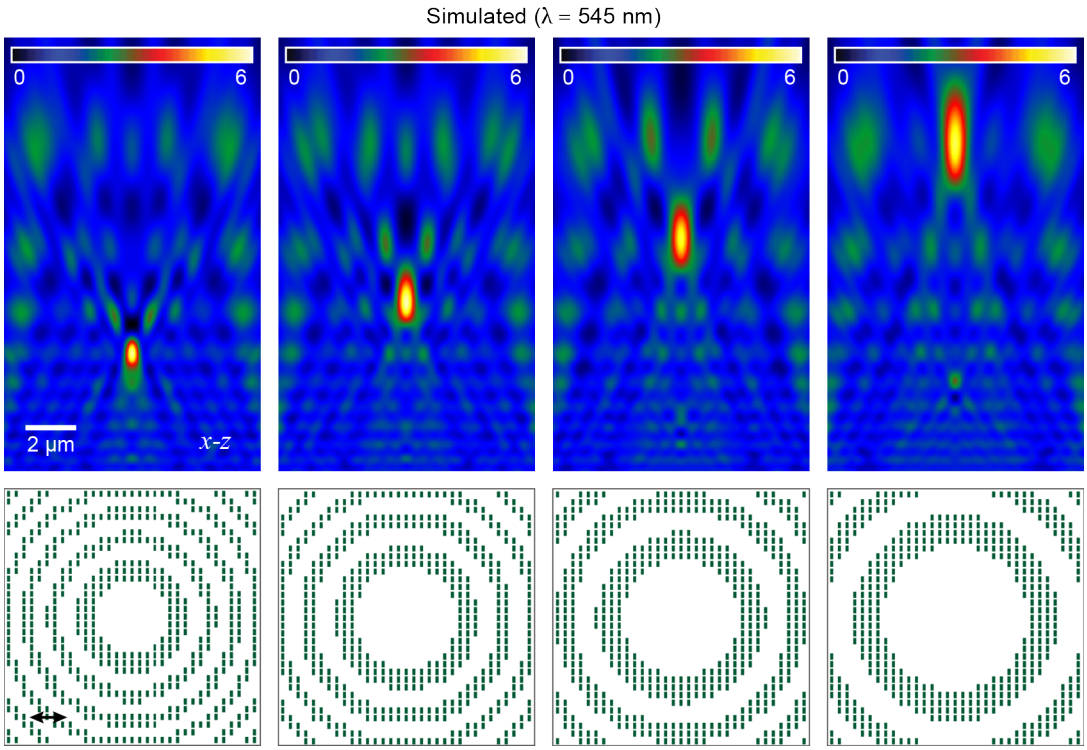

Figure 3.9. Lattice lenses of NP2 designed for longitudinal focusing can also focus light at transverse resonance wavelength. Simulated far-field profiles (upper) at $\lambda = 545$ nm and schemes for lattice structures of NP2 (lower) optimized at $\lambda = 785$ nm. The plane wave source was polarized in the transverse direction of the NP2.

for focal lengths in the 3-10 μm range using the transverse mode of NP2 at $\lambda = 545$ nm (**Figure 3.10**); interband transitions prohibited excitation of LSPs at shorter wavelengths.[72,73] Not surprisingly, the arrangements of NPs optimized for the same focal distance were different at these wavelengths, and similar to macroscopic diffractive lenses, the lattice configurations at shorter wavelengths tended to exhibit denser and thinner annular patterns.[60,63]

3.2.4. Efficiency and FWHM analysis of single-wavelength lattice lenses

Comparison among the optimized lenses of NP1-3 showed that optical intensities at the foci scaled with scattering efficiency of the lattice units (Figure 3.3). The lattice lenses achieved subwavelength focusing with transmission efficiency larger than 60% (**Figure 3.11a**). These structures also showed a two-fold

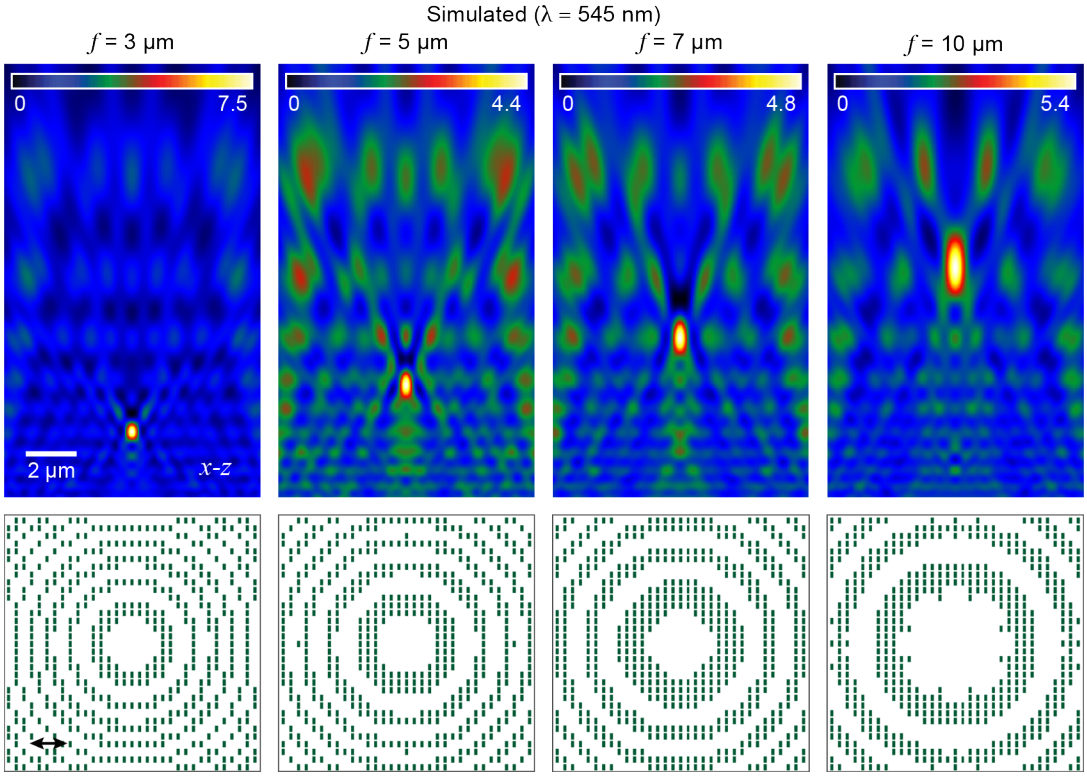

Figure 3.10. LEA can design lattice lenses to focus plane wave light polarized in the transverse direction of NR. (upper) Simulated far-field profiles at $\lambda = 545$ nm and (lower) schemes for lattice structures of NP2 for focal distances ranging from $f = 3$-10 μm

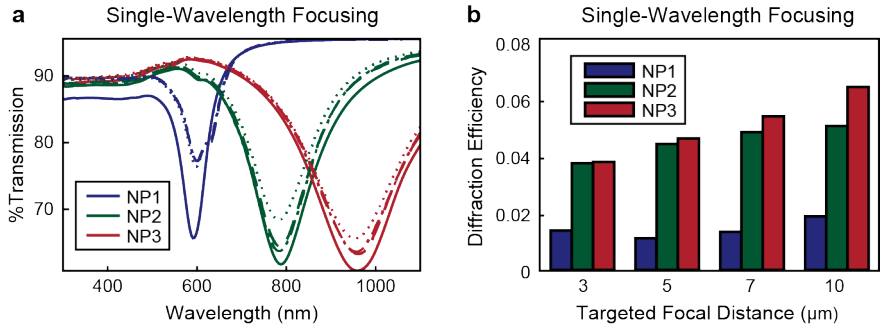

Figure 3.11. Efficiency study of the single wavelength lattice lenses. (**a**) Transmission spectra for lattices of NP1, NP2, and NP3 optimized respectively at $\lambda = 600$, 785, and 980 nm. (**b**) Diffraction efficiency of single focal distance. Transmission spectra from lenses optimized for $f = 3$, 5, 7, and 10 μm are indicated by solid, dashed, dash-dot, and dotted lines, respectively. The spectra were calculated using the setup in Figure 3.1a. The diffraction efficiency was calculated with the setup in Figure 3.1c.

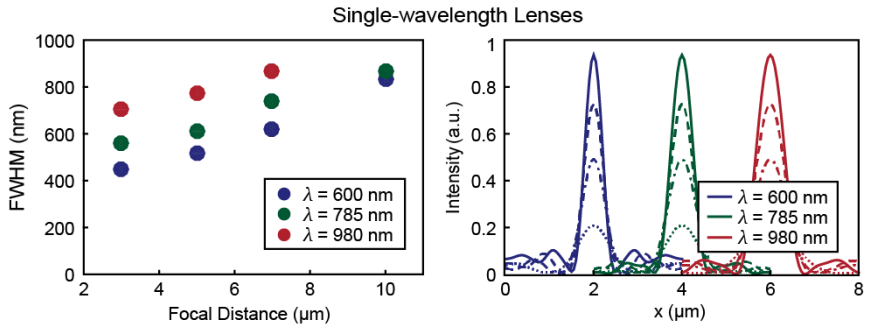

Figure 3.12. Optimized single-wavelength NP lattice lenses can exhibit sub-wavelength focusing. Calculated full-width at half-maximum (FWHM) values and intensity profile across for lattice lenses of single-particle lenses of NP1 for $\lambda = 600$ nm (blue), NP2 for $\lambda = 785$ nm (green), and NP3 for $\lambda = 980$ nm (red). Intensity profiles from lenses optimized for $f = 3$, 5, 7, and 10 μm are indicated by solid, dashed, dash-dot, and dotted lines, respectively.

increase in focus intensity compared to nanohole lattice optics[13] even though the NP diffraction efficiency was 1.5-7% (**Figure 3.11b**). Although the diffraction efficiency (the fraction of transmitted light directed to the focal point) of NP systems was limited, this efficiency can be improved by using a denser lattice and/or incorporating multiple phase elements.

Figure 3.12 shows the FWHM values of the focal points extracted from FDTD simulations for single-shaped lattices. Similar to other diffractive lenses with high NA,[13] these lattice lenses achieved spot sizes below 500 nm, three times smaller than refractive microlenses with similar diameters.[70] With increasing focal distance (decreasing NA), the foci broadened in agreement with the Rayleigh criterion ($d = \frac{\lambda}{2\mathrm{NA}}$) that spot size scaled inversely proportional to the optical NA $= n \sin\theta$.[70] Overall, the NP lenses showed an increase in throughput and a wider operation wavelength range compared to their hole counterparts while preserving the ease of fabrication and adaptive design process.[13] Although the measured efficiencies are lower than dielectric metalenses (because of higher losses in metallic NPs), our plasmonic lattice lenses are more than ten times thinner than dielectric structures,[9] which is an advantage for flat optics. In addition, our evolutionary design strategy provides an alternative approach to realize both plasmonic and dielectric planar lenses based on simple building blocks.

3.3. Multi-Particle Lattice Lenses for Achromatic Focusing

This section describes the design of multiwavelength achromatic metalenses using more than one type of plasmonic lattice units, where each NP unit controls light at the wavelength matching its LSP wavelength. We developed a two-objective LEA that could optimize simultaneously the same focal point at two different wavelengths using lattices with two different NP shapes. Finally, we showed that this evolutionary design strategy could be extended to a larger number of wavelengths and achieved achromatic focusing at three wavelengths.

3.3.1. Inverse fitness function for concurrent design at two wavelengths

Compared to computational methods such as Monte Carlo, evolutionary algorithms are efficient at solving problems with more than one criterion.[42,43] The design of multiwavelength achromatic lenses can be regarded as a multiobjective problem, where achieving the same focal length at each wavelength is considered a single objective. We used the LEA to solve for a structure that focused light to the same focal point but at two different wavelengths by requiring the fitness values calculated for both in Equation 1.5 to be maximized concurrently. In this achromatic design problem, the objective functions conflicted because lattice configurations that favored the focusing at one wavelength typically would lower the performance at the other.[49] Therefore, outputs that simultaneously achieve the same fitness values as the single-criterion solutions have compromised performance at both wavelengths.[8] These compromised results, called Pareto optimal solutions,[48,50] depend on the solutions optimized for each criteria and can be tuned by the definition of the overall fitness. We were interested in specific Pareto solutions that resulted in focusing with the same intensity at the focal distance of the two wavelengths. For evolutionary algorithms, defining the fitness function is the key to realize stable convergence. However, when we carried out LEA calculations using existing multiobjective fitness functions based on function transformations,[42] we could not obtain achromatic solutions. Therefore, we used the inverse-form fitness function F (Equation 2.4) that facilitated balanced performances at both criteria introduced in the

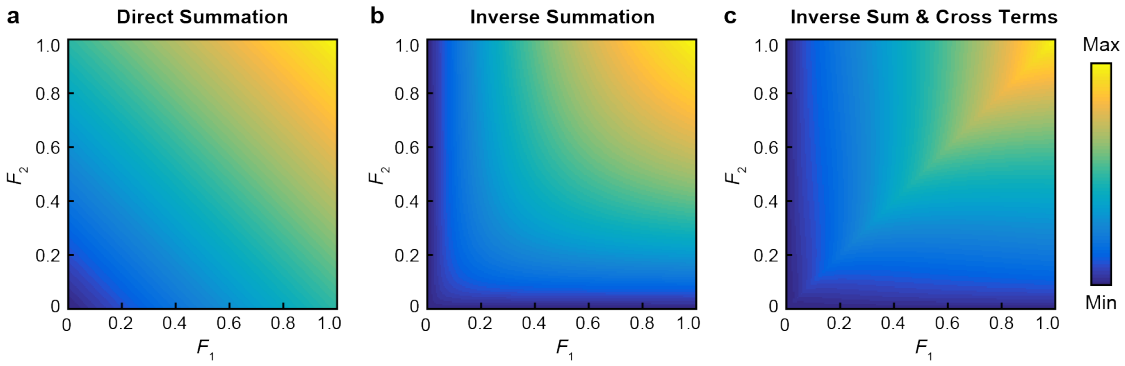

Figure 3.13. Overall fitness value as a function of the performances at two criteria calculated using (**a**) direct summation with Equation 3.3 (**b**) inverse summation with Equation 3.4, and (**c**) inverse summation including the cross difference term (Equation 3.2).

previous chapter as:

$$F^{-1} = {F_1}^{-1} + {F_2}^{-1} + m|F_1 - F_2|/(F_1 + F_2)^2 \tag{3.2}$$

where F_1 and F_2 are, in this design problem, the fitness values calculated at the two wavelengths using Equation 1.5, respectively, and m was an empirical value. Unlike a linear summation, the inverse form is limited by the smaller of the two fitness values and therefore favors maximizing both at the same time. Also, we appended a difference term $|F_1 - F_2|/(F_1 + F_2)^2$ that would lower the overall fitness value whenever F_1 and F_1 were different in order to bias the output of the function towards solutions with even performances at the two wavelengths.After sweeping from 1 to 20, we chose the weight of the difference term m to be 6 to optimize the convergence rate of the calculation; the larger (>15) and lower (<3) values in the range failed to produce the desired result. We compared three fitness functions Equations 3.3-3.5: direct summation based on Equation 2.2, inverse summation, and inverse summation with a cross-difference term.

$$F = F_1 + F_2 \tag{3.3}$$

$$1/F = 1/F_1 + 1/F_2 \tag{3.4}$$

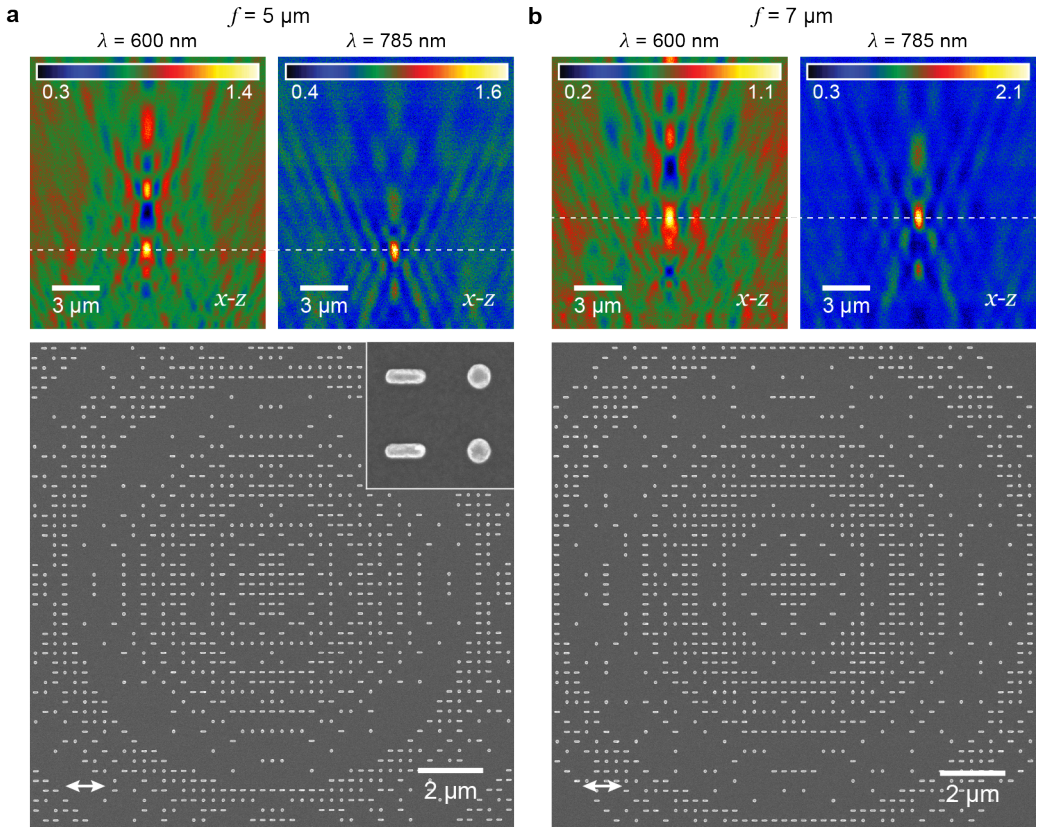

Figure 3.14. Multi-particle lattices designed by LEA can achieve the same focal distance at two wavelengths. (lower) SEM images and the far-field intensity profiles measured by confocal microscope at (left) $\lambda = 600$ nm and (right) $\lambda = 785$ nm corresponding to lattices optimized for focal distances of (**a**) $f = 5$ μm and (**b**) $f = 7$ μm.

$$1/F = 1/F_1 + 1/F_2 + 6|F_1 - F_2|/(F_1 + F_2)^2 \tag{3.5}$$

Figure 3.13 shows the map of the combined fitness functions at different F_1 and F_2 values. Equation 3.3 exhibited no preference to the solutions with balanced F_1 and F_2 values as long as their linear sum remained the same (Figure 3.13a). Consequently, the calculations conducted with this Equation 3.3 were prone to converge to a solution satisfying only one criterion. In contrast, we expected the inverse form to be biased towards balanced objective values because Equation 3.4 evaluated along contours of constant $F_1 + F_2$ always took the maximum value at the diagonal line, especially when the cross difference term was added (Figure 3.13b-c). Therefore, the LEA calculations using Equation 3.5 explored and preferred

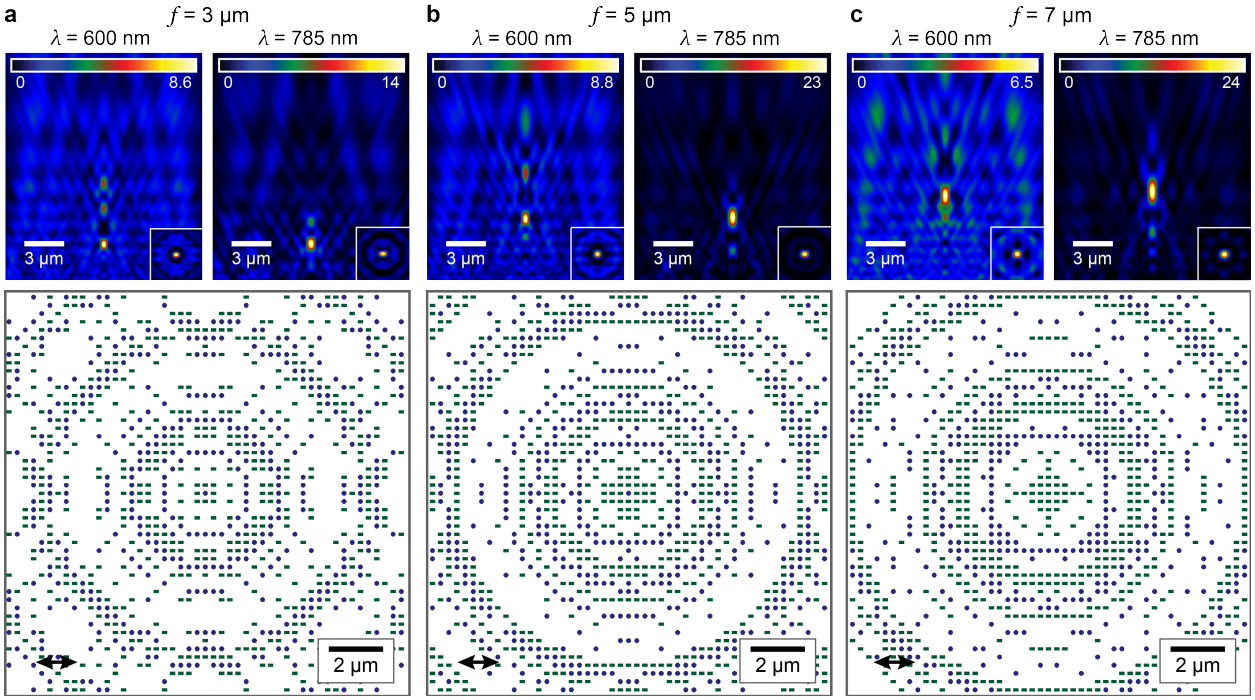

Figure 3.15. Multi-particle lattices designed by LEA can achieve the same focal distance at two wavelengths. (lower) Schemes and the far-field intensity profiles calculated by FDTD simulations at (left) $\lambda = 600$ nm and (right) $\lambda = 785$ nm corresponding to lattices for focal distances of (**a**) $f = 3$ μm, (**b**) $f = 5$ μm, and (**c**) $f = 7$ μm. Insets of upper profiles: x-y cross-sections (4 μm $\times$ 4 μm) depicting the light intensity map at focal planes.

the solution space around the $F_1 = F_2$ line more frequently than others and were more likely to reach the output with balanced achromatic focusing at the two wavelengths.

3.3.2. Achromatic focusing at two wavelengths

To shape the light effectively, we used a lattice based on two different NP shapes, where the two NPs had LSP resonances corresponding to the two target wavelengths, 600 and 785 nm, respectively. We also increased the grid size to 49 $\times$ 49 ($a_0 = 300$ nm) to provide more lattice sites for the particles. We tested the multiobjective LEA for achromatic lattice lens design at wavelengths $\lambda = 600$ and 785 nm using both NP1 and NP2. This Pareto optimization was a trade-off between the optimal solution for each objective function[48–50] and depended on lattice structures optimized for each particle shape. The

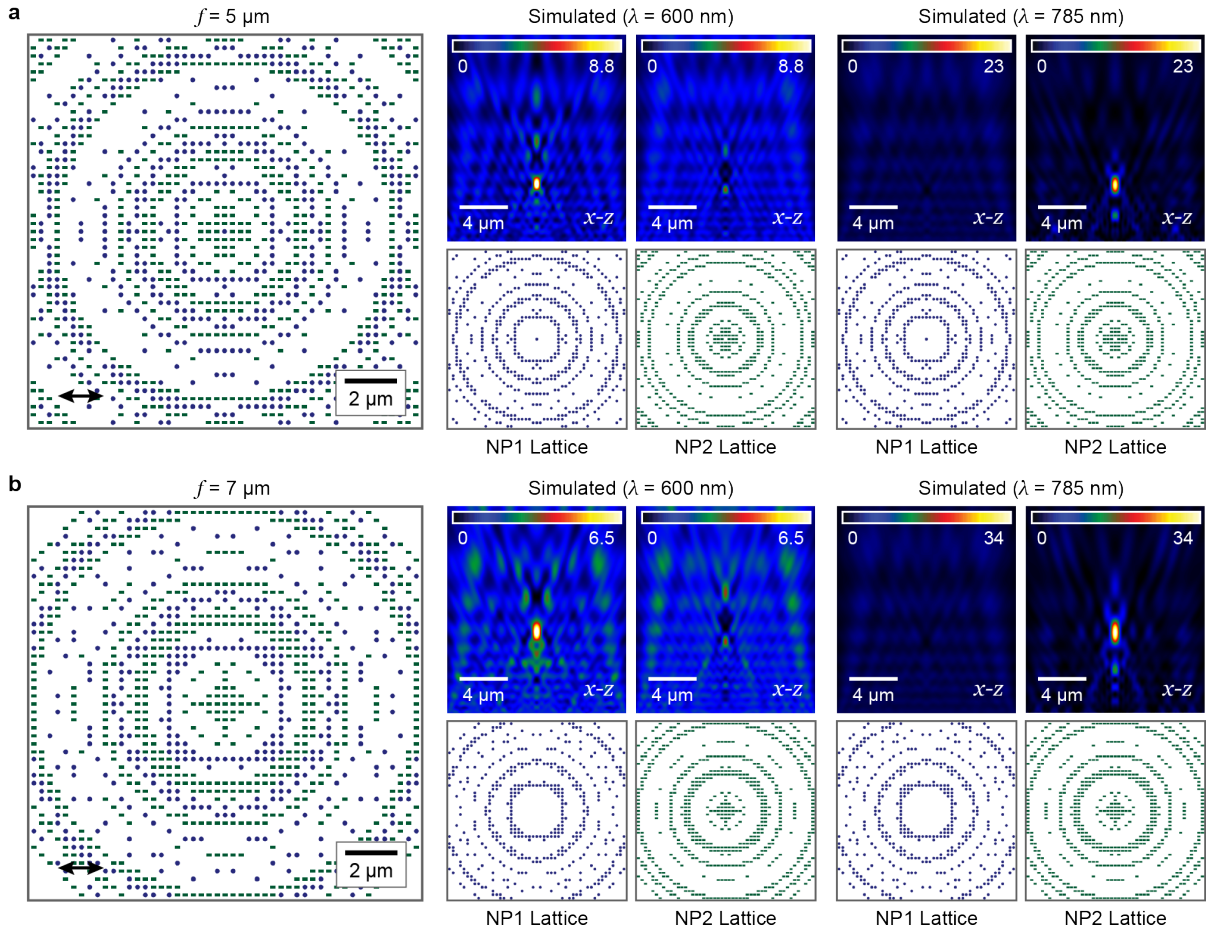

Figure 3.16. The patterns of NP1 and NP2 in the achromatic lenses contribute independently to the focusing at their LSP resonances. Far-field profiles contributed by NP1 and NP2 components of achromatic lattice lenses optimized for (**a**) $f = 5$ μm and (**b**) $f = 7$ μm.

lattice sites occupied by NP1 and NP2 in single-NP lenses overlapped (Figures 3.5–3.7), and so the key to solving the two-objective problem in multi-particle lattices was to resolve these conflicts at minimum cost to efficiency. To demonstrate reliability of the method, we solved for lattice structures targeting a range of focal distances, again from 3 to 7 μm.

Figure 3.14 shows the structures of achromatic lenses and the far-field light profiles they produced from collimated laser sources. The measured results verified the FDTD simulations (**Figure 3.15**). We

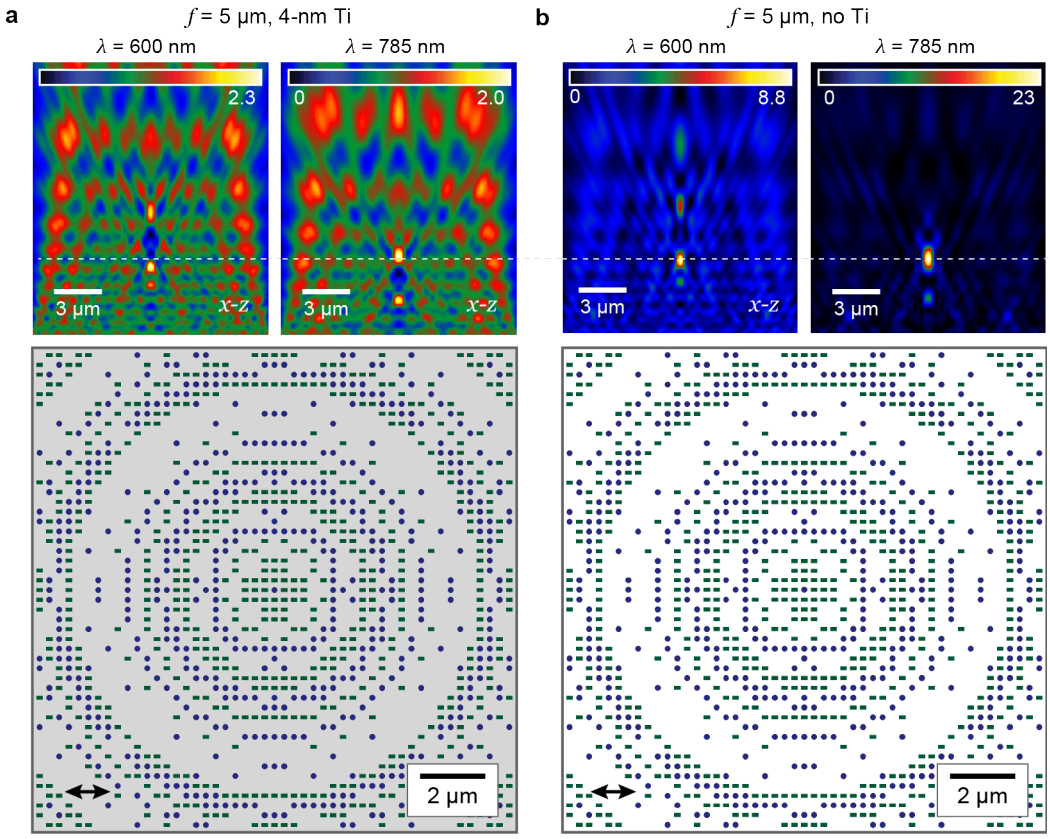

Figure 3.17. Decreased focusing efficiency of multi-wavelength lattice lenses caused by the 4-nm Ti conduction layer. Far-field profiles of biwavelength achromatic lattices lenses ($f = 5$ μm) with Au NPs patterned on (**a**) glass slide with 4-nm Ti conduction layer and (**b**) glass slide calculated by FDTD simulation.

also conducted electromagnetic simulations to show that NP1 and NP2 contributed independently to the focal points at the LSP wavelengths, 600 and 785 nm, respectively. We separated the two particles shapes from an achromatic lens into two lattices and calculated the light profiles by full FDTD simulations (Figure 3.16). As expected, the separated lattice of NP1 and NP2 could focus light to the desired location at their corresponding LSP resonances, 600 and 785 nm, respectively. However, the NP1 lattice lenses had much weaker interaction with light off-resonance at 785 nm, and vice versa for NP2 lattices at 600 nm. Therefore, the combined lattices of the two shapes exhibited the same focal distance at the two wavelengths.

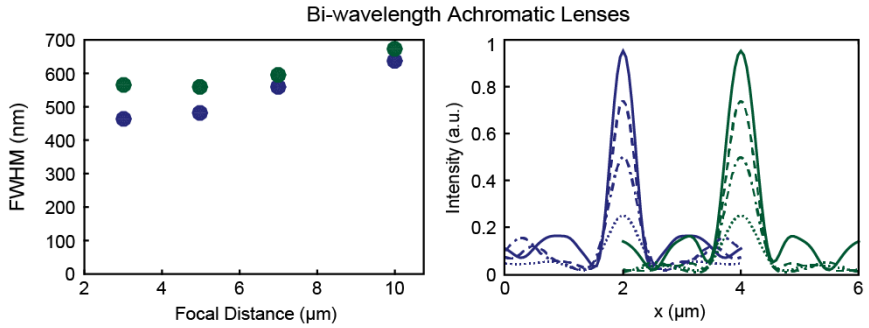

Figure 3.18. Optimized biwavelength NP lattice lenses can exhibit subwavelength focusing. Calculated full-width at half-maximum (FWHM) values and intensity profile across for lattices of NP1 and NP2 measured at $\lambda = 600$ nm (blue) and $\lambda = 785$ nm (green). Intensity profiles from lenses optimized for $f = 3$, 5, 7, and 10 μm are indicated by solid, dashed, dash-dot, and dotted lines, respectively.

Similar to previously reported 1D achromatic lenses,[67] the light profiles exhibited secondary focal points from the chromatic-shifted focal point optimized for the other wavelength. **Figure 3.17** depicts the performance degradation of the achromatic lenses caused by the Ti film, which resulted in a 10-fold decrease of focal intensity at the operational wavelength $\lambda = 785$ nm and also caused the secondary focal points to be as strong as the desired ones. Again, we used a 4-nm Ti layer in the model, although only 2 nm was deposited for EBL, because the FDTD calculations for the entire lattice using less than a 4-nm mesh size required intensive computation power. The Ti film lowered the electric field enhancement by LSP and broadened the resonance peak (Figure 3.6). Consequently, focal points contributed by different NP shapes had similar intensities, and hence the light profiles showed more than the desired single focal point (Figure 3.17a), similar to the experimentally measured result. Compared to the light profiles calculated without Ti film (Figure 3.17b), we also observed minor changes in focal lengths at both wavelengths. However, we did not observe this shift in experimental measurement with 2-nm Ti most likely since the deviation was too small compared to the instrument resolution of the confocal microscope.

We also conducted FWHM analysis of the focal points in the simulations for lattice lens designs achromatic focusing at two wavelengths. These extracted line profiles and the FWHM values showed that the achromatic lenses achieved subwavelength focusing because of their large NA (**Figure 3.18**).

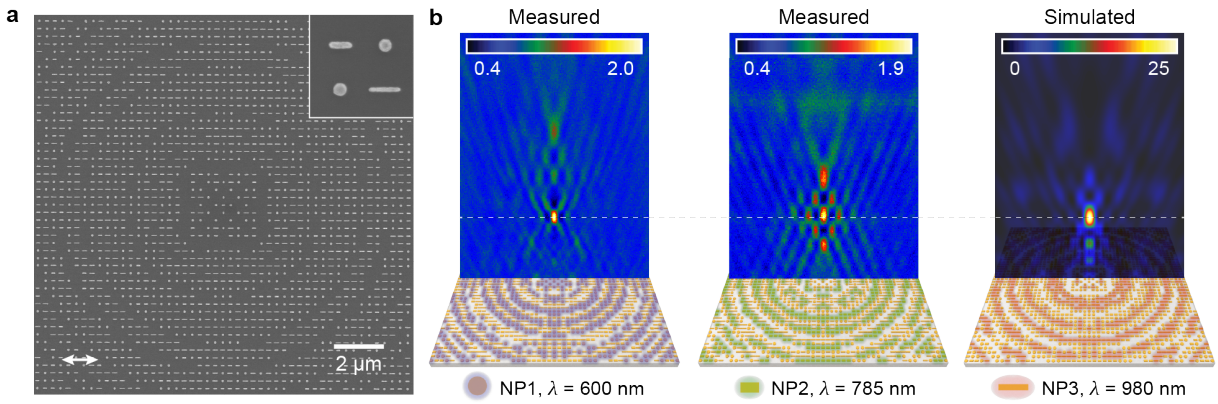

Figure 3.19. Achromatic focusing at up to three wavelengths can be achieved in multi-particle arrays. (**a**) Scheme indicating the structure of the achromatic lattice of three NPs optimized for a focal distance 5 μm. (**b**) Far-field profiles of the lattice structure in (a) measured at $\lambda = 600$ and 785 nm by scanning confocal microscope and calculated at $\lambda = 980$ nm by FDTD.

Similar to single-wavelength solutions, the spot size of achromatic lenses increased with focal distance as a result of decreasing NA.

3.3.3. Achromatic focusing at three wavelengths

Finally, we tested how the design principles of achromatic lattice lenses could be applied to a larger number of wavelengths. We realized achromatic focusing at three wavelengths ($\lambda = 600$, 785 and 980 nm) in lattices of NP1-NP3 with the fitness function redefined as Equation 2.3:

$$F^{-1} = \sum_{i=1\ldots n} {F_i}^{-1} + \frac{m}{2} \sum_i \sum_j |F_i - F_j|/(F_i + F_j)^2 \tag{3.6}$$

where F_i and F_j took values from the F_1-F_3, the fitness for the focusing at each wavelength. The m parameter was determined in a parameter sweep (1-20) to be 12, which produce the fastest convergence speed for the design of triwavelength lenses. **Figure 3.19** shows the structure and far-field profiles of an achromatic lens optimized for $f = 5$ μm. The simulated profile was shown for $\lambda = 980$ nm because the detector on the confocal microscope had poor sensitivity at long wavelengths. However, given that experimental results were in excellent agreement with simulations for the two lower operational

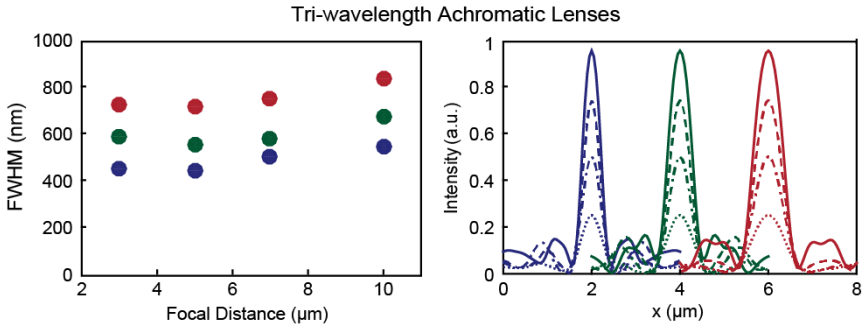

Figure 3.20. Optimized biwavelength NP lattice lenses can exhibit subwavelength focusing. Calculated full-width at half-maximum (FWHM) values and intensity profile across for lattices of NP1-NP3 measured $\lambda = 600$ nm (blue), $\lambda = 785$ nm (green) and $\lambda = 980$ nm (red). Intensity profiles from lenses optimized for $f = 3$, 5, 7, and 10 μm are indicated by solid, dashed, dash-dot, and dotted lines, respectively.

wavelengths and for nanohole lattice optics,[13] we expect the measured light profiles at $\lambda = 980$ nm would be similar to simulations.

Figure 3.21 presents the structures of achromatic lattices optimized by the LEA for other focal distances (f = 3-7 μm) and their focusing profiles calculated by FDTD at all three wavelengths. Interestingly, these lattices showed significantly larger site occupancy and achieved higher focusing intensity at 600 and 785 nm than the biwavelength achromatic lenses optimized for the same focal length. This improvement might result from additional control over phase provided by the third phase element. Both the simulated and measured profiles exhibited achromatic subwavelength focusing at all the three wavelengths (**Figure 3.20**). **Figure 3.22** shows the optical profiles of triwavelength achromatic lenses calculated for wavelengths in the range λ = 532-1080 nm, a range outside the intended working wavelength range. While the intensity varied significantly over this wavelength range, the changes of focal distances due to chromatic aberration were found to be less than 1.4 μm for the profiles simulated at all these wavelengths (**Figure 3.23**).

3.3.4. Performance analysis for multiobjective LEA

As a stochastic method,[42,43,49] the LEA is not guaranteed to produce the same optimized result every time, and its performance must be evaluated by repeated calculations. We conducted LEA calculations

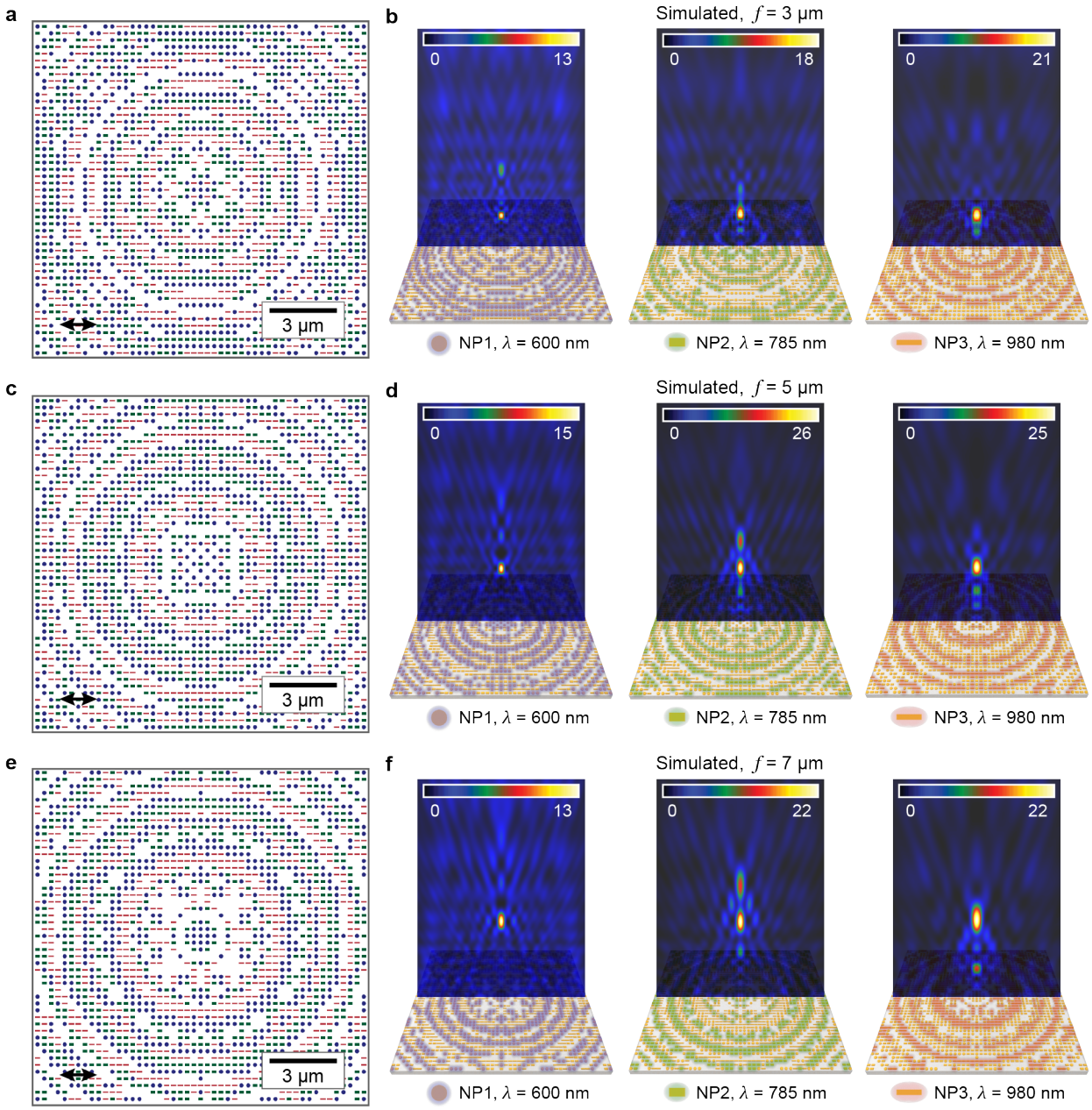

Figure 3.21. Achromatic focusing at up to three wavelengths can be achieved in multi-particle arrays. (**a**), (**c**), and (**e**) Scheme indicating the structure of the achromatic lattice of three NPs optimized for a focal distance f = 3, 5, and 7 μm, respectively. (**b**), (**d**), and (**f**) Far-field profiles of the lattice structure in (a) and (c) calculated by FDTD at $\lambda = 600$, 785 and 980 nm, respectively. Insets of upper profiles: x-y cross-sections (3 μm × 3 μm) depicting the light intensity map at focal planes.

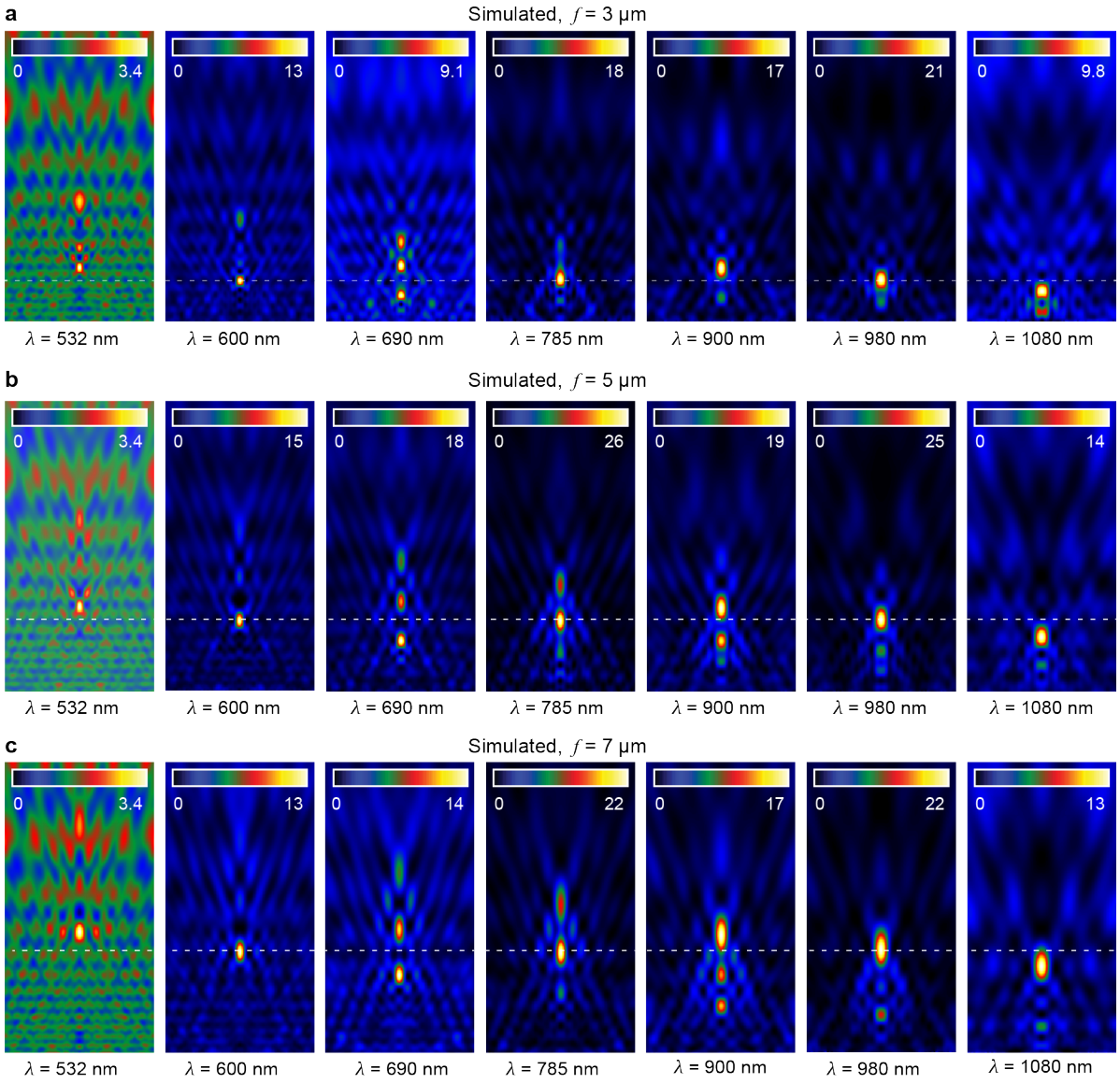

Figure 3.22. Far-field optical profiles evolution of achromatic lenses with wavelength. Far-field x-z light profiles of triwavelength achromatic lenses at wavelengths from $\lambda = 532$ nm to $\lambda = 1080$ nm calculated for objective focal distances of (**a**) $f = 3$ μm, (**b**) $f = 5$ μm, and (**c**) $f = 7$ μm. Width of the shown profiles were 10 μm.

for triwavelength achromatic lenses 16 times and summarized the locations and intensities of the focal points (**Figure 3.24**). The evolutionary algorithm reliably achieved similar performances over repeated runs, even though the calculations involved stochastic searching, for focal distances f = 3-7μm. The

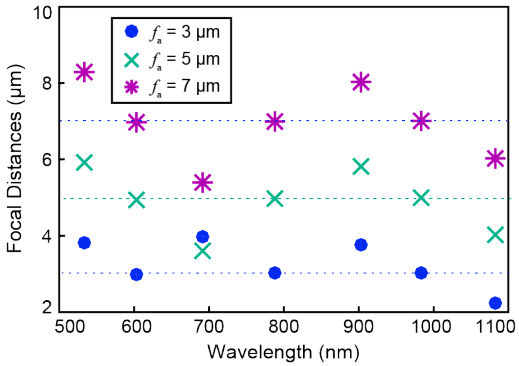

Figure 3.23. Focal distances of achromatic lenses at different wavelengths for triwavelength achromatic lattices.

calculations had smaller success rates for $f = 10$ μm most likely from the smaller NA, which limited the amount of light. With a 8-fold symmetry constraint on the lattice, near-optimal solutions were found within 500 iterations or by searching only 3×10^5 structures among the 4^{325} solutions (**Figure 3.25**). This convergence rate was remarkably less than three times longer than the single-wavelength optimizations which took approximately 200 iterations. We expect our highly-efficient design method to be applicable to a range of optical properties, such as simultaneously directing light to different regions and dynamically controlling light profiles with polarization.

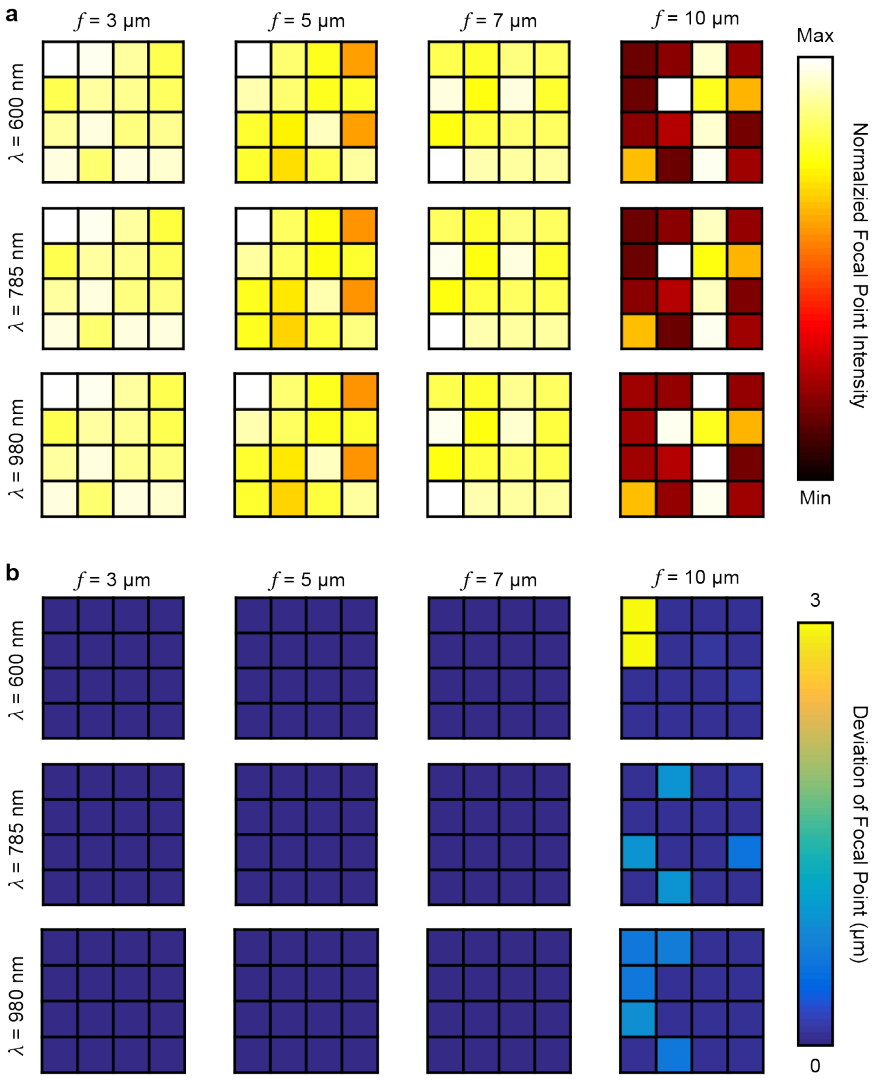

Figure 3.24. LEA performance on designing triwavelength achromatic lenses over 16 repetitions of calculations for focal distances of f = 3, 5, 7, and 10 μm. (**a**) The intensities were close to optimal values for all 16 repetitions when focal distance was between 3 and 7 μm, while the deviation was larger for $f = 10$ μm. (**b**) Desired focal points can be achieved for $f = 3$, 5, and 7 μm among all 16 repetitions when, while the deviation was larger for $f = 10$ μm. The focal point intensity values are normalized by the maximum intensity achieved in the repetitions at the wavelength and focal distance.

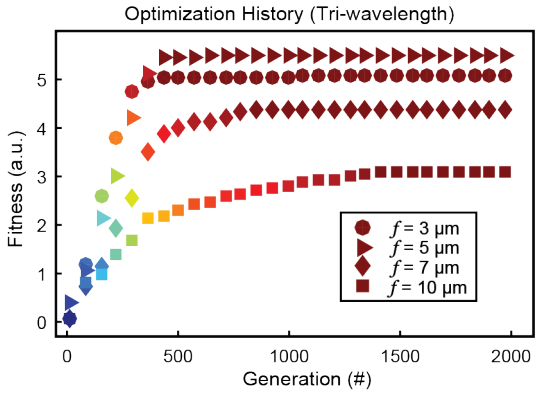

Figure 3.25. LEA fitness parameter as a function of generation number.

3.4. Summary of Multiwavelength AchromaticMetasurfaces by Evolutionary Design

In summary, I have demonstrated an evolutionary approach to design flat plasmonic optics from gold NPs. The NP lattice lenses achieved improved throughput compared with hole unit cells while maintaining the same level of focus precision. The tunability of LSP by particle size enables superb control over the spectral distribution of transmitted light and allows the design of structures that can operate over the visible to near-infrared wavelength range. Multiobjective optimization capabilities of the algorithm suppressed chromatic aberration at up to three wavelengths in multi-particle lattice lenses. I anticipate that chromatic control can be extended to even shorter lens wavelengths (200-500 nm) by using alternative plasmonic materials and can eventually result in broadband achromatic focusing. I expect the evolutionary-algorithm approach of nanostructure design will lead to advances in a variety of fields, from integrated optoelectronics to miniaturized optical interconnects to high-resolution optical microscopy.

3.5. METHODS

3.5.1. Finite-difference time-domain simulations

FDTD calculations based on commercial software (FDTD Solution, Lumerical Inc., Vancouver, Canada) were used to simulate the linear properties (far-field and near-field) of Au NPs. The optical constants of Au were taken from Johnson and Christy (400-1200 nm).[74] A uniform mesh size of 1 nm (4 nm) was imposed on Au NPs in simulations for a single particle or 5×5 arrays (33×33 and 49×49 lattice structures). The electric fields in x-y direction were recorded and exported by a frequency-domain monitor. The exported fields were imported as a single-wavelength source into a 15 μm × 15 μm × 22 μm simulation with a uniform mesh size of 50 nm to calculate the far-field light profiles. More details of the setup could be found in supporting information.

3.5.2. Fabrication of nanoparticle arrays

The NP array was fabricated with a standard electron beam lithography procedure. To eliminate charging of the electron beam on the insulating glass surface, 2 nm of Ti was deposited as a conduction layer with thermal evaporation. Then, e- beam resist (MicroChem PMMA A3 950k) (110 nm) was spin-coated on the slide (4000 rpm, 45 s). Patterns of lattice lenses were drawn in DesignCAD with BasicCAD scripts and written on the PMMA resist at 800 μC/cm^2 (30 kV and 40 pA). The patterns were developed for 75 s in 25% methyl isobutyl ketone (MIBK) diluted with isopropyl alcohol (IPA), 40-nm Au was deposited using a thermal evaporator, and then lift-off was performed in acetone to produce the NP arrays.

3.5.3. Confocal measurements of NP lattice lenses

Confocal Measurements of NP Lattice Lenses: A confocal scanning optical microscope (WITec alpha-300) was used to measure the light profiles generated from plane-wave light incident on the lattice lenses.[13,28] A fiber-coupled super continuum laser (Kaheras SuperK Power Plus) with an acousto-optic tunable filter (AOTF, Koheras Spectrack Dual NIR + 4×VIS) and collimator (Thorlabs F280FC-780) were used to generate the collimated incident beam. A polarizer (Thorlabs 10GL08) was used when linearly polarized

incident light was required. The lenses were measured in air by 100× air objective (Nikon Plan Fluor, NA = 0.90), and the transmitted photons were collected by a photomultiplier tube (PMT, Hamamatsu Photonics H8259-01). The PMT tube based on silicon had low sensitivity beyond 800 nm, and light profiles were measured only at $\lambda = 600$ nm and 785 nm but not at $\lambda = 980$ nm. The scan resolution was 50 nm using an integration time of 0.01 s/pixel for all measurements.

CHAPTER 4

Lattice-Resonance Metalenses for Fully Reconfigurable Imaging

This chapter describes a reconfigurable metalens system that can image at visible wavelengths based on arrays of coupled plasmonic nanoparticles. These lenses manipulated the wavefront and focused light by exciting surface lattice resonances that were tuned by patterned polymer blocks on single-particle sites. Predictive design of the dielectric nano-blocks was performed using an evolutionary algorithm to create a range of 3D focusing responses. For scalability, I demonstrated a simple technique for erasing and writing the polymer nanostructures on the metal nanoparticle arrays in a single step using solvent assisted nanoscale embossing. This reconfigurable materials platform enables tunable focusing with diffraction-limited resolution and offers prospects for highly adaptive, compact-imaging.

Referenced work: J. Hu, D. Wang, X. Ren, D. Bhowmik, T. Liu, D. Shi, M. P. Knudson, X. Ao, and T. W. Odom, "Lattice-Resonance Metalenses for Fully Reconfigurable Imaging." *submitted* **2019**

4.1. Introduction to Lattice Resonances and Reconfigurable Metalenses

This section introduces the emerging reconfigurable metasurfaces for imaging applications. Although metalenses can replace the functionalities of refractive optics in compact designs, these planar structures have fixed optical responses and cannot achieve adaptive imaing planes. Conventional imaging systems adjust focal planes and magnification by mechanical motion of lens elements, but devices constructed based on this strategy will have large thickness regardless of the lens thickness. Therefore, reconfigurable metalenses with tunable focal point positions are essential to realizing compact tunable imaging systems.

4.1.1. Metalenses for compact imaging devices

Metalenses are an emerging platform for compact optical elements[9,21] used in imaging devices, ranging from multifunctional endoscopes[75] to wide-angle cameras.[22] These planar lenses focus light by shaping the optical wavefront using subwavelength phase units and can achieve diffraction-limited imaging after aberration-corrected processes.[23,24,76] Metalenses cannot easily image complex three-dimensional (3D) objects[77,77,78] because adaptive focusing over multiple image planes is required, and metalenses typically exhibit fixed optical responses and feature resolution only within the depth of focus.[79] In addition, metalenses designed by wave-optics principles cannot produce multiple foci with arbitrary arrangements.[13,32] Therefore, next-generation metalenses will involve reconfigurable lensing and a design strategy that can enable multi-plane focusing.

4.1.2. Existing strategies to realize dynamics photonic devices

Active metalenses have been demonstrated by systems that respond to external stimuli. For example, when optical antennas are patterned on flexible substrates, the metalens focal lengths can be changed by mechanical stretching.[80–82] However, such long-range modulation strategies are limited to shifting a single focal point along the lens axis because all units are adjusted collectively; there is no tunability at the single-unit level. Fully-reconfigurable metasurfaces have been realized by laser writing on light-sensitive phase-change materials.[75] Constrained by intrinsic materials properties, these devices only operate in the near-infrared (NIR) range and rely on serial and time-consuming fabrication processes. A versatile

strategy for reconfigurable wavefront tuning in the visible and ultraviolet (UV) wavelength ranges is still needed.

Plasmonic nanoparticle (NP) arrays that support surface lattice resonances [83–85] (SLRs) are promising for reconfigurable metasurfaces in the visible range because these collective excitations show abrupt phase delays [86] at resonance and can be tuned by changing the dielectric environment. Moreover, the hybrid modes are tolerant to localized disorder and can be supported in structured infinite arrays with a fraction of the NPs removed. [87] This tolerance can imply that tailoring the wavefront phase between the lattice sites by removing the NPs or changing the refractive index to switch the SLR enhancements on and off in each lattice cells. In general, tuning dielectric environment is easier than changing the plasmonic phase elements and can be a simple strategy to realize tunable metasurfaces. Light focusing or steering by SLRs has not yet been reported because existing methods cannot tune the wavefront by adjusting the phase between adjacent NPs in the array.

4.1.3. Lattice evolution algorithm for designing metasurfaces on coupled nanoparticles

Previously, we have introduced a lattice evolution algorithm (LEA) that can design plasmonic metasurfaces by tailoring the arrangement of simple lattice unit shapes on a square grid. This method denotes the targeted focal point by a fitness function F and uses a genetic algorithm to solve for nanostructures to maximize F. [13] Using a multiobjective fitness function, this predictive algorithm can realize multiple focal points positioned on user-defined imaging planes. Importantly, the LEA can account for materials properties and plasmonic coupling using finite-difference time-domain (FDTD) simulations, which can calculate how the optical phase and intensity are tuned on coupled NP arrays by SLR excitations. [88] The LEA designs based on a square array also naturally allow lattice resonance excitations if the NPs in a uniform refractive index environment are used as the lattice units.

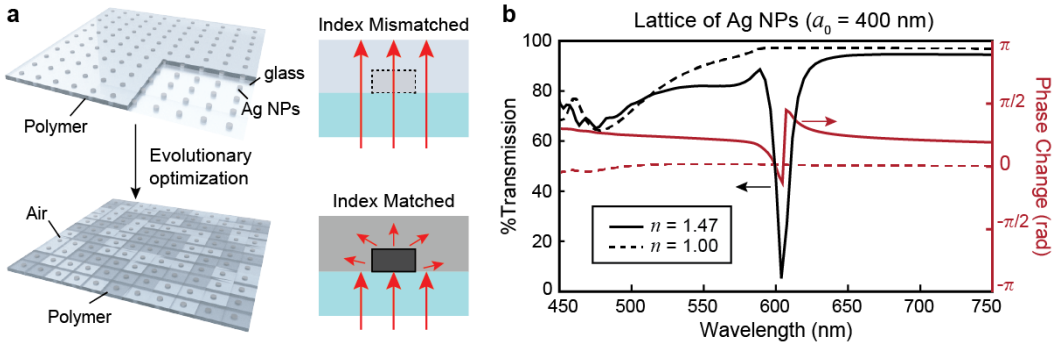

Figure 4.1. Metasurfaces can be enabled by localized modulation of lattice resonances on coupled plasmonic NPs (**a**) Scheme metasurface phase elements based on tuning surface lattice resonances (SLR) by superstrate dielectric environment. (**b**) Transmission spectrum and phase delay of Ag NP arrays in (solid line) uniform and (dashed line) nonuniform dielectric environment

4.2. Hybrid Lattice-Resonance Metalenses for 3D Imaging

This section demonstrate a metalens platform with unit-level tunability for programmable 3D imaging at visible wavelengths. The wavefront profiles for light focusing were achieved by tuning the SLR on an array of identical plasmonic NPs and a nanopatterned dielectric superstrate. By optimizing the superstrate pattern, the LEA could predict metalenses for any desired multi-plane lensing. This metasurface platform can be extended to wavelengths spanning the UV-NIR range by changing the lattice spacing and plasmonic materials. FDTD simulations showed that LEA-designed lenses at all these wavelengths realized subwavelength lensing with large NAs (short focal lengths). We also showed that the lattice resonance metasurfaces could form images in two planes simultaneously.

4.2.1. Tuning lattice resonances on coupled plasmonic nanopartice arrays

Figure 4.1a depicts our metalens architecture based on two types of phase elements arranged in a square lattice: (1) Ag NPs exposed to air, and (2) identical NPs covered by a thin dielectric block. With SLR excitations, this coupled plasmonic NP array exhibited optical field confinement and phase delays that were significantly more prominent on the NP units surrounded by dielectric compared to those in air. LEA was used to design SLR-metalens for targeted foci by tailoring the arrangement of the two building blocks. We demonstrate how surface lattice resonances (SLR) were tuned by the superstrate dielectric

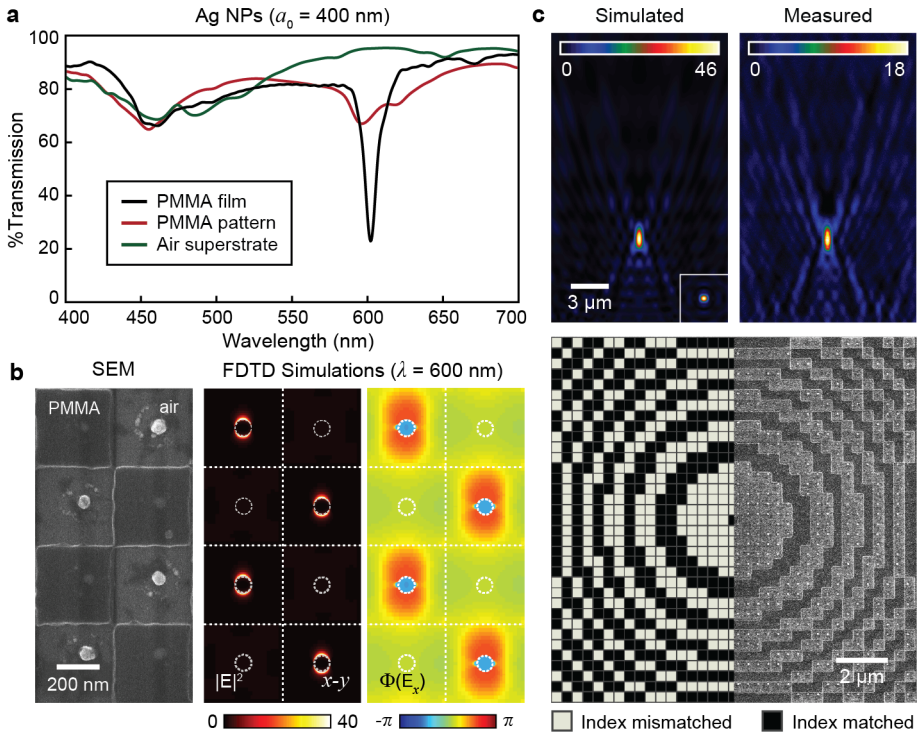

Figure 4.2. Optical wave-front can be tuned locally on strongly coupled plasmonic NP arrays. (**a**) Transmission spectra of Ag NP arrays in an infinite poly-(methylmethacrylate) (PMMA) thin film, random patch of PMMA, and air as superstrate dielectric environment. (**b**) (left) Scanning electron microscopy (SEM) images, near-field (middle) intensity profile and (right) phase map for PMMA patterns on a periodic NP array. (**c**) Simulated (upper left) and measured (upper right) light profiles obtained at a wavelength $\lambda = 600$ nm from metalenses structures (lower) optimized for a focal distance of $f = 7$ μm. Optical spectra and profiles were calculated by FDTD simulations. Insets of upper profiles in (c): x-y cross-sections (4 μm $\times$ 4 μm) depicting the light intensity map on the focal plane.

constants on arrays of Ag NPs ($a_0 = 400$ nm) on silica substrate ($n = 1.46$). **Figure 4.1b** shows the transmission spectra and phase delay calculated by FDTD simulations for this NP array with different superstrate refractive index. When covered by a dielectric layers with a $n = 1.47$ refractive index, these NPs exhibited a strong resonance with up to $\pi/2$ phase delay at the wavelength $\lambda = 600$ nm. In contrast, the NP lattice exposed to air experienced different index in the superstrate and substrate and showed negligible light extinction and phase delay. Both lattices showed a weak localized surface plasmon (LSP) resonance around $\lambda = 470$ nm intrinsic to the individual Ag NPs.

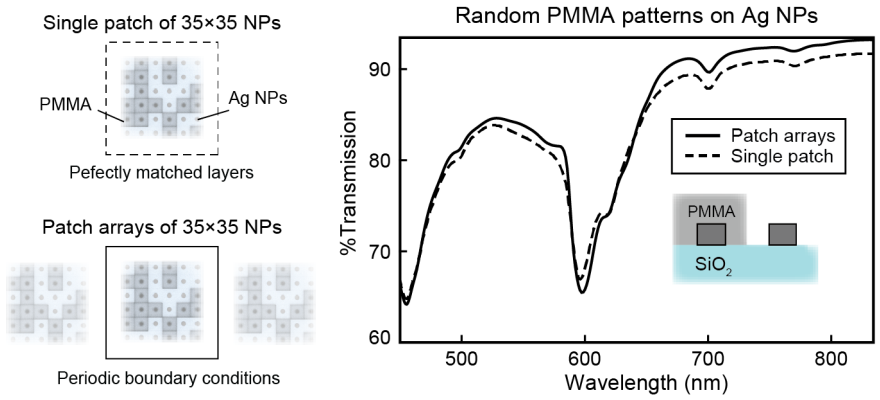

Figure 4.3. Lattice plasmon resonances can be excited on patches of coupled plasmonic NP arrays. The transmission spectra were calculated by FDTD simulations for (solid line) periodic arrays of 35×35 Ag NP patches simulated using periodic boundary conditions in the x/y directions and (dashed line) a single Ag NP patch simulated by absorbing perfectly matched layers. Both calculations had 60% particles randomly covered by PMMA blocks. The NPs had a diameter $d = 84$ nm and height $h = 50$ nm and were arranged in the lattice with spacing $a_0 = 400$ nm. The PMMA layer had a thickness $t = 140$ nm.

4.2.2. Subwavelength wavefront tuning by on plasmonic lattices with superstrate dielectrics

To demonstrate visible-range metalenses, we focused on the operating wavelength $\lambda = 600$ nm. The lattice units were realized by patterning polymethylmethacrylate (PMMA, index $n = 1.47$) on silica substrates with 2D Ag NP arrays (spacing $a_0 = 400$ nm, diameter $d = 84$ nm, and height $h = 50$ nm) for a SLR at $\lambda = 600$ nm. **Figure 4.2a** shows the transmission spectra of this NP array calculated by FDTD simulations with different superstrate dielectric environments. A strong and narrow SLR was observed from NPs in a PMMA film ($t = 140$ nm) at $\lambda = 600$ nm, but when the superstrate was air, only a weak localized surface plasmon resonance was supported. This resonance was maintained when the superstrate PMMA was patterned (red line). The SLR was maintained in both finite and periodic NP patches (35×35) covered by random PMMA blocks with $L = 400$ nm. The NP lattice with patterned PMMA blocks experienced a lower effective refractive index[89] with 40% NPs exposed to air and exhibited a 10-nm blue-shift in SLR wavelength compared to an array surrounded by a uniform PMMA film.

We further investigated the optical response of the Ag NPs in randomly patterned PMMA blocks in simulations using different boundary conditions. **Figure 4.3** shows the calculated transmission spectra

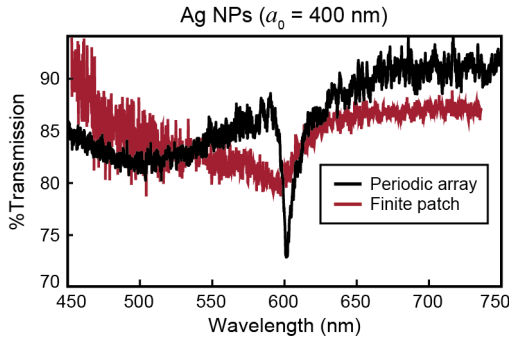

Figure 4.4. Measured transmission spectra for infinite Ag NP arrays on SiO_2 substrate with different superstrate index environments. The NPs had a diameter $d = 84$ nm and height $h = 50$ nm. The periodic NP array was measured with a spin-coated 140-nm PMMA film and the finite patch was patterned randomly by EBL.

of a 35×35 patch with 60% randomly selected NPs covered by PMMA blocks. In the FDTD setup, we simulated a single 35×35 NP patch using perfectly matched layers (PMLs) at all boundaries and patch arrays using periodic boundary conditions in x and y directions. In both setups, the SLR modes were maintained at $\lambda = 600$ nm but exhibited weaker intensity and broader FWHM compared to the Ag NPs in unpatterned PMMA. This simulation result confirmed that the SLR excitations were tolerance to localized index mismatches caused by patterning of the superstrate dielectrics.

Figure 4.4 showed the optical spectra for measured from a large-area periodic NP array in a PMMA film and a region of the array covered by random PMMA patterns. We measured the transmission of the periodic NP array fabricated on a SiO_2 substrate using a white-light laser source and a spectrometer. The patterned patch area was selectively measured by bright-field microscopy with slits and binning. This spectroscopy method[90] was intended for measuring dark-field scattering and exhibited large noises in bright-field transmission setups. The sharp resonance of the array and the broader resonance of the patch were both observed at $\lambda = 600$ nm and confirmed experimentally the SLR could be excited on a Ag NP lattice with patterned superstrate index.

Figure 4.2b shows a SEM image of PMMA blocks patterned on a 2D array of Ag NPs on a silica substrate and their simulated near-field electric field intensity and corresponding phase maps. Prominent electric field enhancement and phase delay were observed only on NPs surrounded by PMMA, whose

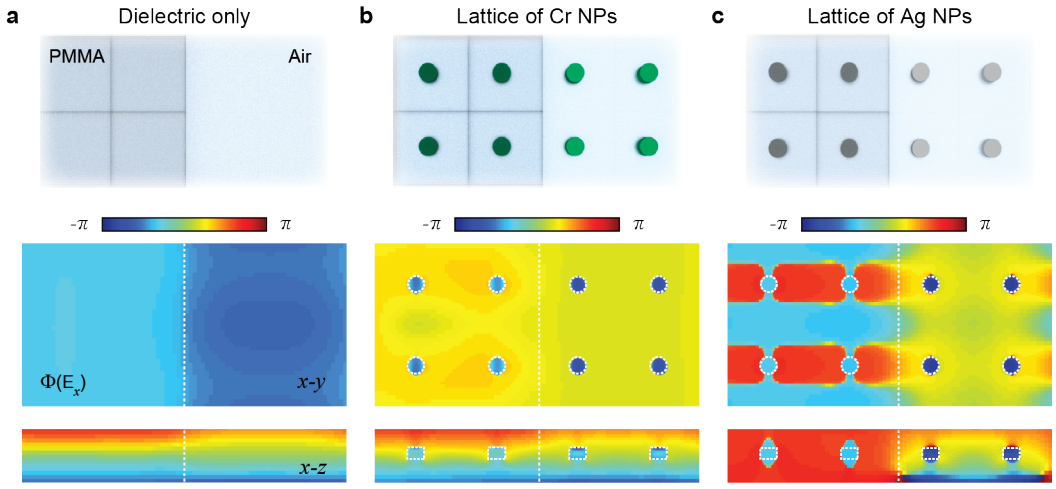

Figure 4.5. Lattice plasmon resonances can enhance the phase delay contrast induced by dielectric patterns. (Top) Schemes of dielectric and plasmonic patterns, wavefront phase mapping in (middle) x-y planes and (bottom) x-z planes calculated by FDTD simulations for (**a**) pure dielectric patterns, (**b**) Cr NPs, and (**c**) Ag NPs in the same refractive index environment. The dielectric patterns of PMMA and air are on silica substrate. The NP array spacing $a_0 = 400$ nm, height $h = 50$ nm, and diameter $d = 84$ nm. The spacing and diameter are optimized for periodic Ag NP arrays to produce a lattice resonance at wavelength $\lambda = 600$ nm.

index matched the silica. Therefore, optical phase can be tailored by SLRs at the single-unit cell level by patterned dielectrics. We also calculated the near-field phase profile of pure PMMA-air patterns in comparison with PMMA patterned on NP arrays made in plasmonic and non-plasmonic materials (**Figure 4.5**). The largest phase contrast between PMMA and air regions were observed on the Ag NPs array ($a_0 = 400$ nm) at their SLR resonance $\lambda = 600$ nm. Therefore, light steering and focusing in PMMA-AgNP lattices was contributed by both the phase delay by the dielectric structure and lattice plasmon enhancement.

4.2.3. Proof-of-concept metalenses by lattice resonance excitations

Figure 4.2c depicts a PMMA-Ag NP lattice lens (14 μm × 14 μm footprint) and far-field profiles optimized for $f = 7$ μm to achieve a high numerical aperture (NA = 0.71). The profile calculated by FDTD simulations showed a focal length and focus FWHM consistent with scanning confocal microscopymeasurements using a laser source at $\lambda = 600$ nm.[52] This metalens showed higher focal intensities than NP

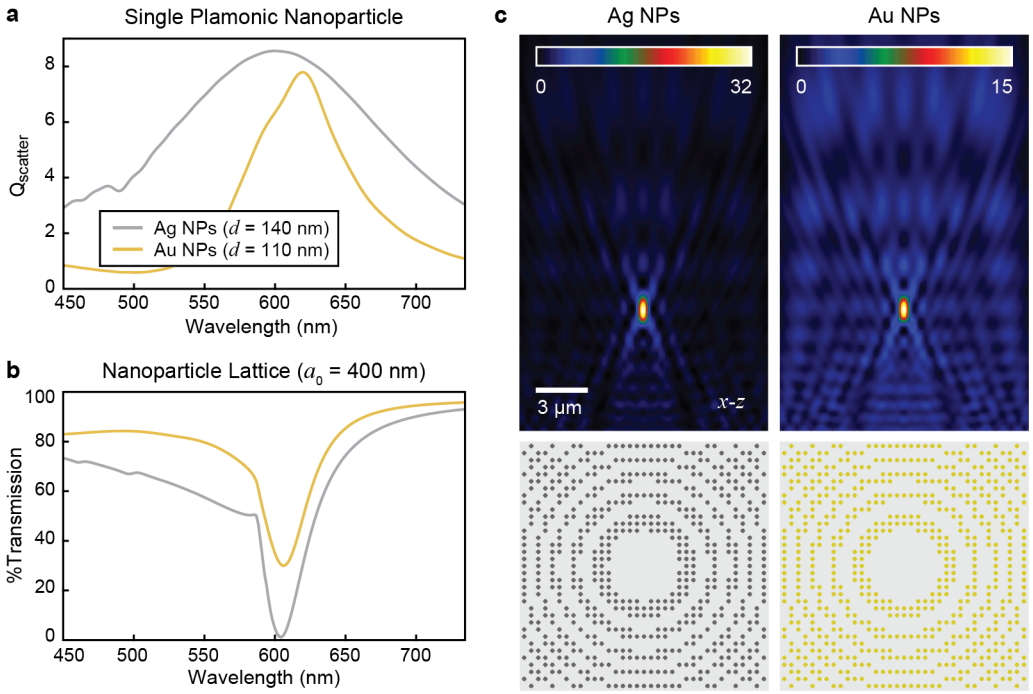

Figure 4.6. Lattice lenses based on localized surface plasmon resonances. (**a**) Single-particle scattering efficiency and (**b**) transmission spectrum of Ag ($d = 140$ nm) and Au ($d = 110$ nm) NP arrays ($a_0 = 400$ nm) with localized surface plasmon (LSP) resonance at $\lambda = 600$ nm in air calculated by FDTD simulations. (**c**) Schemes of lattice lenses based on localized surface plasmon resonances optimized by lattice evolution algorithm (LEA) for a focal length $f = 7$ μm and the corresponding far-field light profiles of (left) pure Ag NPs, and (right) Au NPs. Far-field optical profiles were calculated by FDTD at wavelength $\lambda = 600$ nm.

lenses based on localized surface plasmons in air with the same lattice spacing and focal length. The light focusing by LSP lattice lenses were evaluated by FDTD simulations using Ag and Au NPs in air. **Figure 4.6ab** shows the scattering and transmission spectra of the Ag and Au NPs optimized for a LSP resonance around $\lambda = 600$ nm. **Figure 4.6c** shows the LSP lens structures designed by LEA using these particles with a same $a_0 = 400$ nm spacing on silica substrate in air superstrate and the corresponding x-z light profile calculated by FDTD simulations. The SLR-metalenses realized focal intensity 44% larger than the Ag lattice and 207% than the Au lattice.

To verify the contribution of SLRs to lensing, we calculated focusing profiles of the same PMMA metalens pattern without plasmonic NPs using FDTD simulations. We used a metalens design for a focal

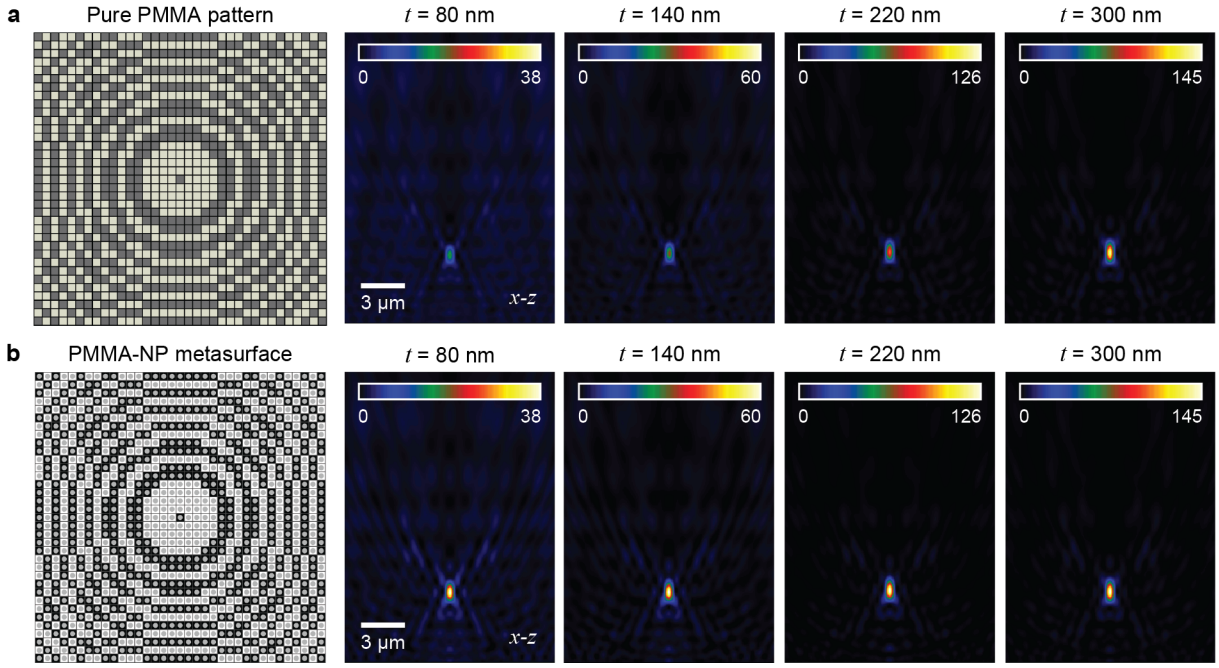

Figure 4.7. Lattice resonance excitations on Ag NP lattices can enhance focal efficiency. Schemes of plasmonic lattice lenses and the corresponding far-field light profiles of (**a**) pure PMMA patterns with a range of thicknesses and (**b**) the same pattern on arrays of Ag NPs calculated by FDTD simulations at wavelength $\lambda = 600$ nm. The NP array spacing $a_0 = 400$ nm, height $h = 50$ nm, and diameter $d = 84$ nm. The lens was designed for a focal length $f = 5$ μm by the LEA.

length of $f = 5$ μm by LEA simulations at $\lambda = 600$ nm. **Figure 4.7** shows the calculated focal intensities of the dielectric lens pattern with the PMMA thicknesses in the range $t = 80$-300 nm in comparison with the same designs with the Ag NP lattice. Compared with the PMMA-only structure, SLR lenses with the Ag NP array achieved a two-fold increase in focal intensity in a 140-nm thick device because of enhanced phase contrast. **Figure 4.8** further showed the focal profiles of single-focus ($f = 7$ μm) and two-foci metalenses based on a pure PMMA pattern ($t = 140$ nm), PMMA on Cr NPs, and PMMA on Ag NPs. The plasmonic NP array realized prominent enhancement over the dielectrics alone and the Cr NP in both lens designs. Therefore, the enhancement in focal intensity was contributed by the SLR sustained by the Ag NPs but not the diffraction mode effect by the lattice.

We also evaluated the chromatic aberration of the metalens designs in Figure 4.2c which exhibited a focal length $f = 7$ μm. **Figure 4.9** shows simulated results for the metalens at wavelengths in the

range λ = 580-640 nm. These far-field profiles showed a decrease in focal length as the wavelength of incident light increased due to chromatic aberration. We observed the largest focus intensity at $\lambda = 600$ nm because the NP array phase delay was maximized at this SLR wavelength.

4.2.4. Optical losses in experimental designs

The increase in focal intensity by Ag NPs predicted in simulations was less prominent in experiment because the fabricated devices were defective compared to the ideal structures in simulations. One structural factor was that the PMMA films prepared by spin-coating experimentally had air gaps around the NPs.[89] To isolate the effect of air gap on the lens performance, we compared PMMA patterns made on a flat silica substrate to the same pattern on arrays of silica NPs prepared by EBL and electron beam evaporation (**Figure 4.10a**). Without an air gap, the silica NPs, which had the same refractive index with the substrate, should have negligible effects on the focal intensity. **Figure 4.10bc** shows the lensing characteristics of PMMA patterns with and without the silica NPs measured by scanning confocal microscopy at $\lambda = 600$ nm. Because the incident light intensity varied slightly with time, we conducted multiple confocal measurements while alternating between the lens samples on the flat substrate and the silica NPs. We also fabricated multiple lenses on each sample and measured a different one each time to account for the sample-by-sample difference. The PMMA lenses on the flat substrate consistently showed larger focal intensity than the patterns on silica NPs and indicated that the air formed by spin-coating on structured surfaces compromised the focal intensity.

Arrays of Ag NPs also exhibited intrinsic non-radiative losses that could be increased by surface roughness and shape irregularity in the fabricated structures. **Figure 4.11** shows the x-z light profiles of a PMMA lens pattern in comparison with the same pattern on Ag NPs measured by scanning confocal microscopy. At the SLR (λ = 600 nm), these two lenses showed similar focal intensity because the SLR enhancement compensated for the losses in the NPs. At an off-resonance wavelength $\lambda = 550$ nm, lenses with plasmonic components showed 40% lower in focal intensity than the pure dielectric ones. The comparison justified our conclusion that the SLR contribution to light focusing was less prominent

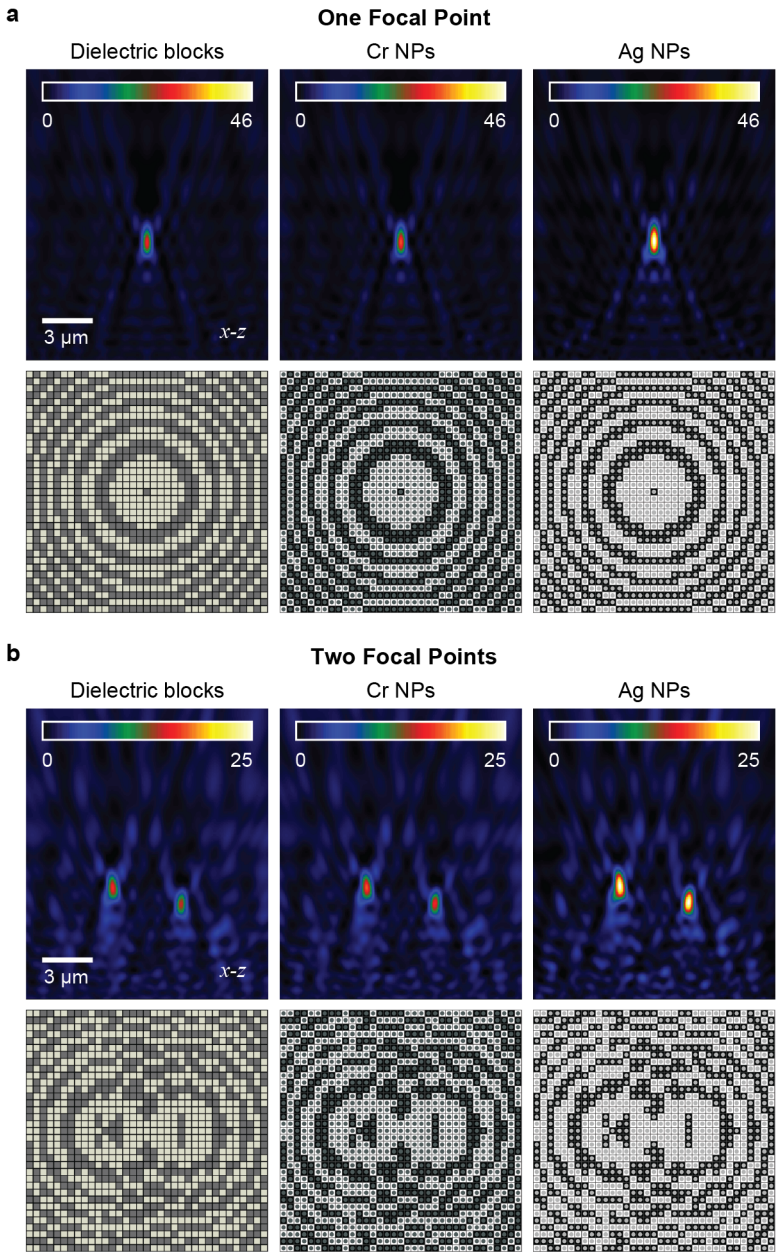

Figure 4.8. Plasmonic NPs can enhance the efficiency of optical focusing in dielectric patterns. Schemes of plasmonic lattice lenses and the corresponding far-field light profiles of (left) pure PMMA patterns, (middle) Cr NPs, and (right) Ag NPs in the same dielectric structures optimized for (**a**) a single focal point and (**b**) two focal points. The dielectric patterns on silica substrate consist of PMMA (dark) and air (bright). The NP array spacing $a_0 = 400$ nm, height $h = 50$ nm, and diameter $d = 84$ nm. Far-field optical profiles were calculated by FDTD simulations at wavelength $\lambda = 600$ nm. The metalens in (a) has a focal length of $f = 7$ μm. The focal points in (b) are at $x = \pm 2$ μm, $y = 0$, and $z = 6$, 7 μm.

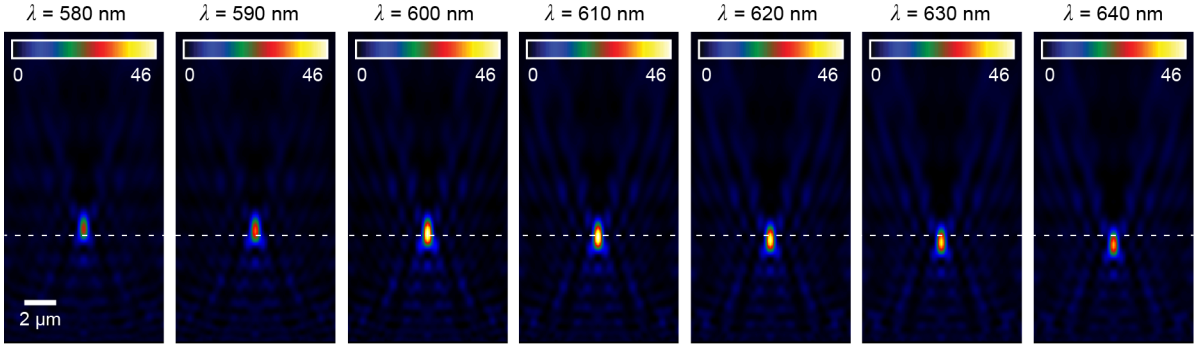

Figure 4.9. Chromatic aberration in lattice plasmon metalenses. Far-field x-z light profiles of SU-8 lenses at wavelengths from $\lambda = 580$ nm to $\lambda = 640$ nm calculated for objective focal distances of $f = 7$ μm.

in experimental measurements than simulation predictions due to the large losses in fabricated PMMA-AgNP metalenses.

We also evaluated how SLR intensity affected light focusing by metalenses. The SLR modes realized in experiments (Figure 4.4) realized narrow linewidths but were much lower in intensity compared to simulated spectra (Figure 4.1b). By increasing the height of the Ag NPs from 50 to 80 nm, we obtained a lattice mode with a strong, deep resonance comparable to the calculated transmission spectrum (**Figure 4.12a**). However, the measured SLR showed a linewidth more than 2 times broader than the simulated spectrum and indicated that the fabricated lattice exhibited larger losses.[91] (**Figure 4.12b**) shows the peak focal intensity achieved by PMMA metalenses patterned on Ag NPs and SiO_2 NPs measured by confocal microscopy at $\lambda = 600$ nm. Except for the third pair of measurements, the SLR metalenses realized larger focal intensity than the dielectric structures.

4.2.5. Multi-focal lensing by inverse fitness functions

The LEA can design metalenses for producing arbitrary numbers of foci with flexible spatial arrangements using the multiobjective fitness function previously introduced as Equation 2.3:

$$F^{-1} = \sum_{i=1\ldots n} {F_i}^{-1} + \frac{1}{2}\sum_i \sum_j |F_i - F_j|/(F_i + F_j)^2 \tag{4.1}$$

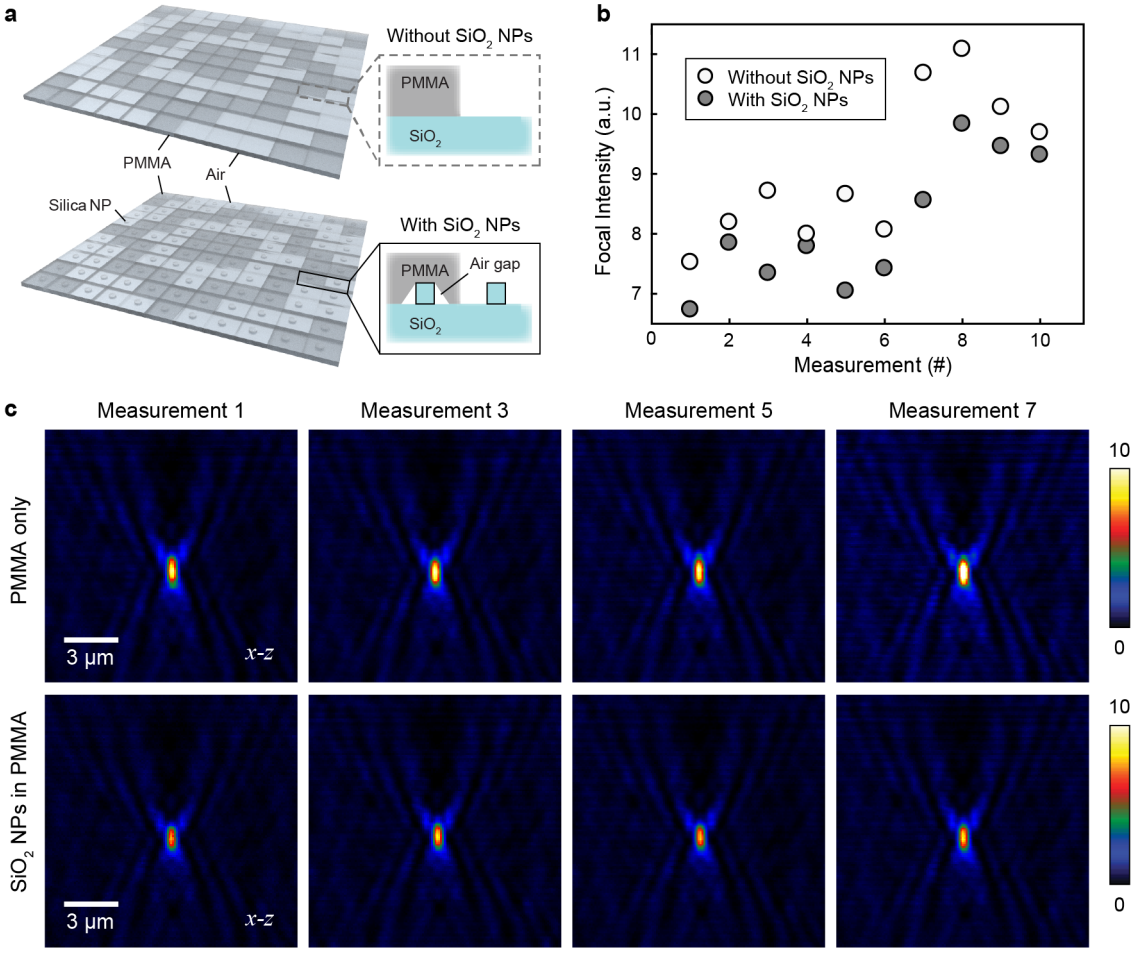

Figure 4.10. Air gaps around NPs lowers lens efficiency. (**a**) Schemes of lattice lenses consisting of (upper) pure dielectrics and (lower) dielectric blocks with silica NPs that produce air gaps in the spin-coating process. (**b**) Maximum focal intensity of the same lens design with and without silica NPs over 10 pairs of lens samples and (**c**) the x-z light profiles collected for some measurements. The NP array and PMMA block spacing $a_0 = 400$ nm, height $h = 50$ nm, and diameter $d = 84$ nm. The light profiles were measured by confocal microscopy at wavelength $\lambda = 600$ nm. The metalenses in (c) has a focal length of $f = 7$ μm.

where both F_i and F_j took values from F_1-F_n, which were the fitness values for each desired focus calculated by Equation 1.5:

$$F(\Delta f) = \frac{I}{\Delta f + c} \tag{4.2}$$

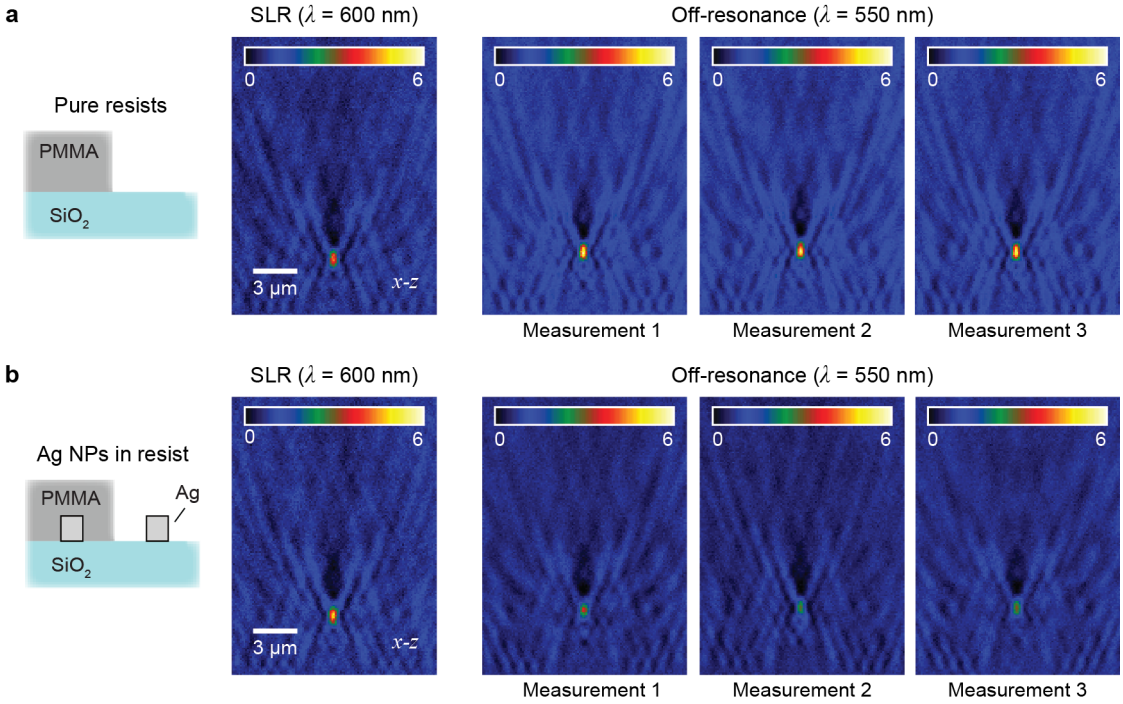

Figure 4.11. Lens efficiency degradation due to losses in experimentally fabricated plasmonic NPs. Comparison between measured x-z profiles of focal point for (**a**) pure PMMA metalenses and (**b**) lens structures patterned on arrays of Ag NPs at (left) the SLR wavelength $\lambda = 600$ nm and (right) an off-resonance wavelength $\lambda = 550$ nm with three repetitions.

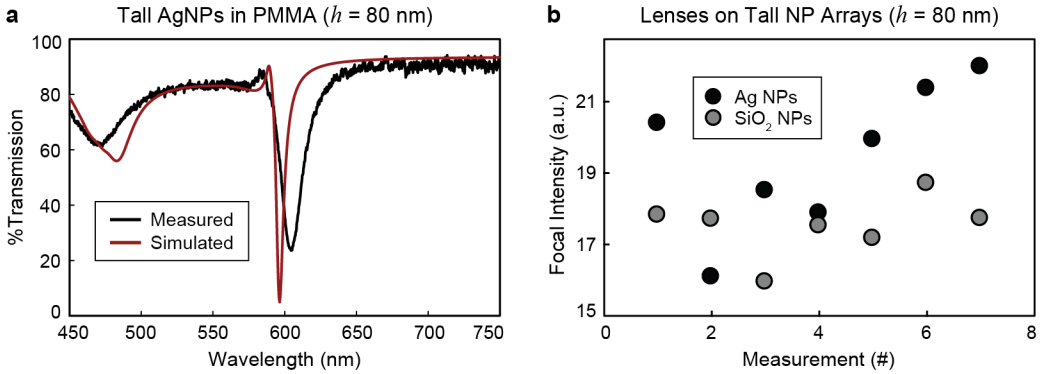

Figure 4.12. Performance evaluation for metalens patterned on tall NPs. (**a**) Transmission spectrum of Ag NP arrays with $h = 80$ nm measured by confocal microscopy measurements. The NP lattice has spacing $a_0 = 400$ nm and diameter $d = 84$ nm. (**b**) Maximum focal intensity of the same lens design with Ag and silica NPs over 7 pairs of lens samples characterized by confocal microscopy at $\lambda = 600$ nm.

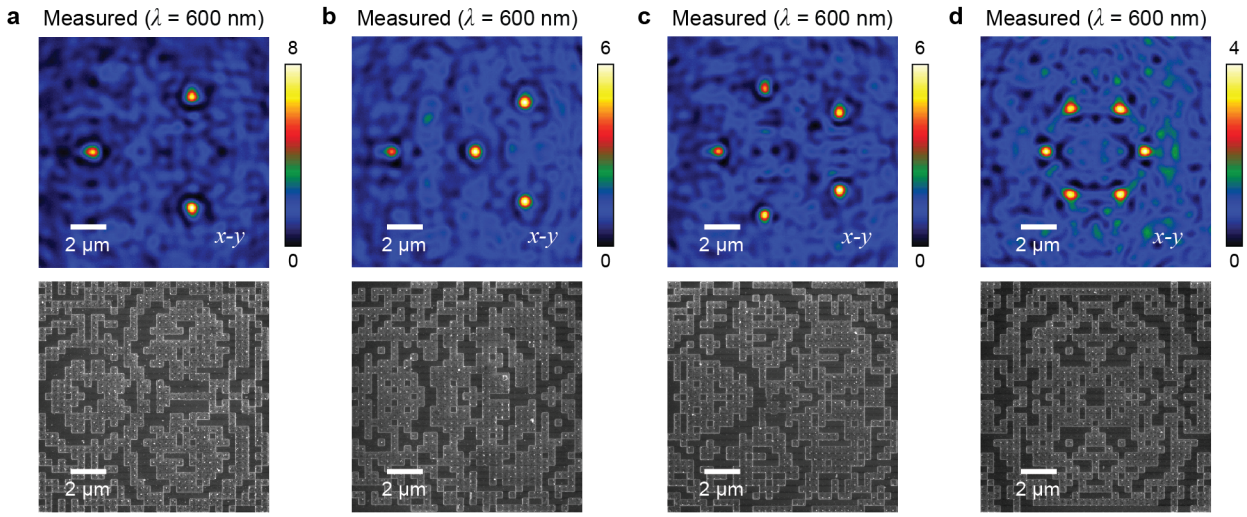

Figure 4.13. Lattice plasmon metasurfaces can produce multiple focal points that form arbitrary light profiles. (lower) SEM images of PMMA-NPs metasurfaces and (upper) the corresponding confocal microscopy images obtained at wavelength λ = 600 nm. (**a**) Three focal points separated from the lattice center by $r = 4$ μm on the $z = 7$ μm plane. (**b**) four focal points at x = -5 μm and 1 μm, $y = 0$ μm and $x = 4$ μm and $y = \pm 4$ μm on the $z = 9$ μm. (**c**) Five focal points separated from the lattice center by $r = 4$ μm on the $z = 7$ μm plane. (**d**) Six focal points separated from the lattice center by $r = 3$ μm on the $z = 7$ μm plane.

where F was the fitness value, I was the intensity at the desired focal point, Δf was the deviation between the desired and actual focal points, and c was a positive constant. (**Figure 4.13**) shows the SEM images of four representative multi-focal metalenses patterned in a PMMA layer on Ag NPs and their x-y light profiles measured by confocal microscopy in the $z = 7$ μm plane. The focal points showed balanced optical intensity for all the designs with 3-6 foci as predicted by the LEA regardless of their arrangements.

4.2.6. Lattice-resonance metalenses for ultraviolet to near-infrared wavelengths

This design is general and also applicable to UV-NIR regimes, where the SLR wavelength was tuned from 305 to 875 nm by varying the NP spacing from a_0 = 200 to 600 nm. **Figure 4.14** shows the lens structures for a single focal point at $f = 10$ μm designed at wavelengths λ = 305 nm (Al, a_0 = 200 nm), 450 nm (Al, a_0 = 300 nm), 735 nm (Au, a_0 = 500 nm), and 875 nm (Au, a_0 = 600 nm) on a

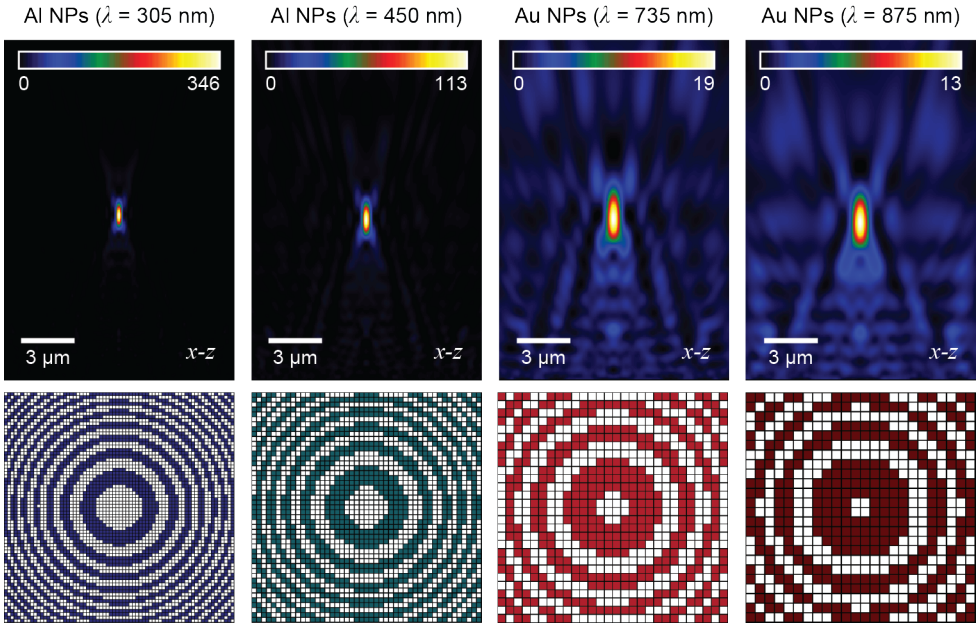

Figure 4.14. Reconfigurable metalenses can be designed for the ultraviolet (UV) to near-infrared (NIR) wavelength regimes. (lower) Schemes of metalens structures and (upper) the corresponding optical profiles calculated by FDTD for a focal point at $f = 10$ μm (from left to right) at wavelengths $\lambda = 305$ nm, 450 nm, 735 nm, and 875 nm. Lattices depicted from left to right consist of Al NPs ($a_0 = 200$ nm, $d = 36$ nm), Al NPs ($a_0 = 300$ nm, $d = 84$ nm), Au NPs ($a_0 = 500$ nm, $d = 106$ nm), and Au NPs ($a_0 = 600$ nm, $d = 140$ nm), respectively

14×14 μm^2 square area. As the wavelength was increased, the focal point broadened as the diffraction limit scaled linearly with the wavelength. Consequently, the maximum focal intensity also decreased at longer wavelengths because the same optical power was spread over a larger volume. **Figure 4.15** also showed the multi-focal metalenses designed at the wavelengths ranging from ultraviolet to near-infrared range.We also extracted the linear optical intensity profile and extracted the FWHM from the lens designs at different wavelengths (**Figure 4.16**). At all these wavelengths, the high NA designs with $f = 5$ and 7 μm realized subwavelength focusing. Metalenses with a single focal point showed diffraction-limited focusing at all these wavelengths (Figure 4.16). FDTD calculations also showed diffraction efficiencies up to 10% and 6% for lenses optimized for 305 and 450 nm and 4% for ones at 600, 735 and 875 nm (**Figure 4.17**).

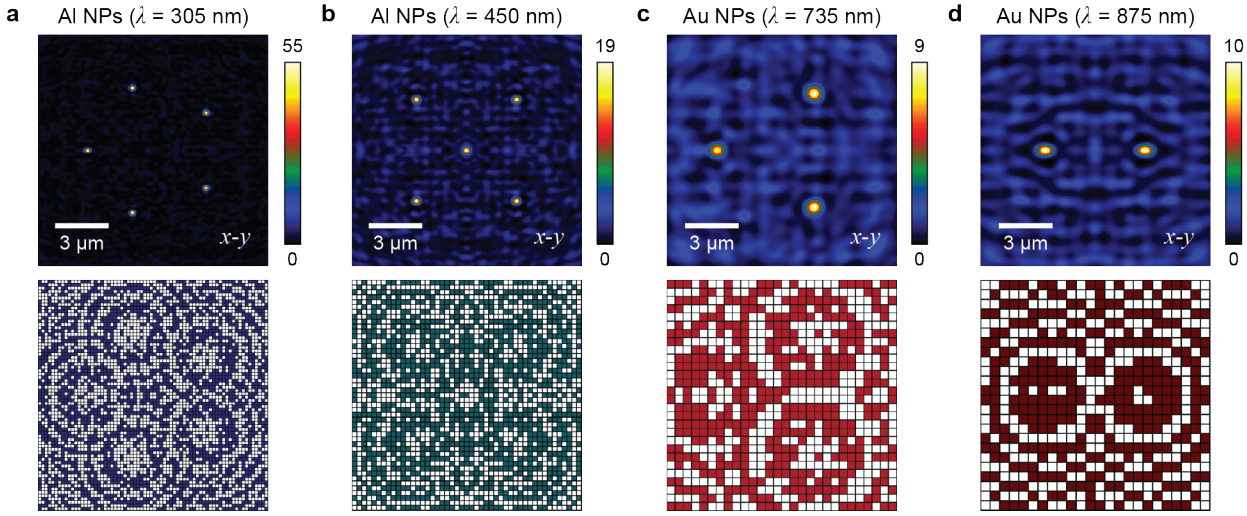

Figure 4.15. Reconfigurable lattice plasmon metasurfaces can be designed for the ultraviolet (UV) to near-infrared (NIR) wavelength regimes. (Lower) Schemes of metalens structures and (upper) the corresponding optical profiles calculated by FDTD for for obtaining (**a**) 5 focal points separated by $r = 4$ μm from the center on the $z = 7$ μm plane ($\lambda = 305$ nm), (**b**) 5 focal points ($x, y = 0$, $x, y = \pm 3$ μm) on the $z = 7$ μm plane ($\lambda = 450$ nm), (**c**) 3 focal points separated by $r = 4$ μm from the center on the $z = 9$ μm plane ($\lambda = 735$ nm), and (**d**) 2 focal points ($x = \pm 3$ μm, $y = 0$) at $z = 5$ μm plane. Lattices depicted in (a-d) consist of Al NPs ($a_0 = 200$ nm, $d = 36$ nm), Al NPs ($a_0 = 300$ nm, $d = 84$ nm), Au NPs ($a_0 = 500$ nm, $d = 106$ nm), and Au NPs ($a_0 = 600$ nm, $d = 140$ nm), respectively.

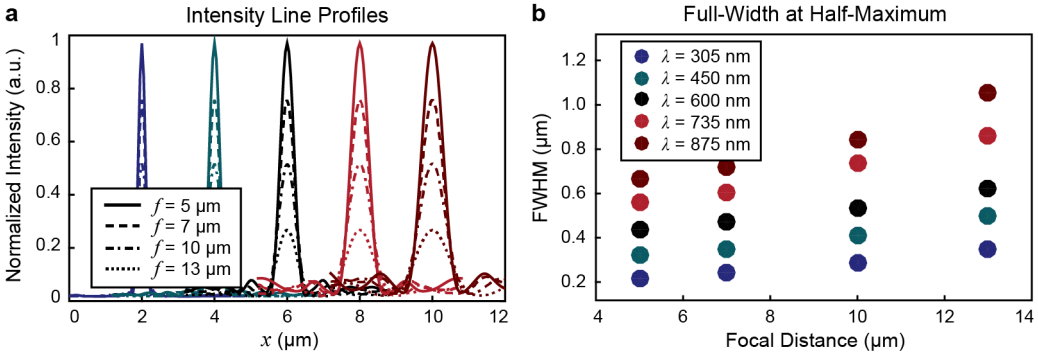

Figure 4.16. Optimized NP lattice lenses can exhibit subwavelength focusing. (**a**) Line profiles of focal points and the (**b**) full-width at half-maximum (FWHM) extracted for lenses designed for wavelengths $\lambda = 305$ nm (Al, $a_0 = 200$ nm), $\lambda = 450$ nm (Al, $a_0 = 300$ nm), $\lambda = 600$ nm (Ag, $a_0 = 400$ nm), $\lambda = 735$ nm (Au, $a_0 = 500$ nm), and $\lambda = 865$ nm (Au, $a_0 = 600$ nm).

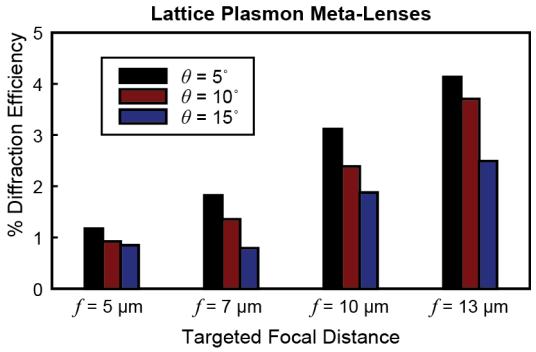

Figure 4.17. Diffraction efficiency of metalenses designed for wavelengths ranging from ultraviolet to near-infrared regimes. The metasurfaces with lattice constants a_0 = 200 nm, 300 nm, 400 nm, 500 nm, and 600 nm have operating wavelengths at $\lambda = 305$ nm, 450 nm, 600 nm, 735 nm, and 875 nm, respectively.

4.2.7. Imaging demonstration for lattice-resonance metalenses

To demonstrate the imaging capabilities of the SLR metalenses, we expanded the grid size of LEA calculations to 275 × 275 ($a_0 = 400$ nm) on a larger footprint (110 μm × 110 μm) to simplify alignment to the imaged objects. **Figure 4.18a** shows a scheme of the setup as a proof-of-concept test of imaging using an optical microscope with a CMOS detector. A white-light source controlled by a Kohler aperture was filtered to pass red light (600 ± 5 nm), which was then focused by the condenser to the object separated from the lenses by 250-μm silicone spacers. Monochromatic images produced by the metalens were collected by the objective lens and recorded by the camera. **Figure 4.18b** shows the fractal structure used as the object to characterize the resolving capabilities of the SLR metalenses for features ranging from 1 to 15 μm. **Figure 4.18c** shows the structure of the PMMA-Ag NP metalens (f = 160 μm and NA of 0.33) and the image formed. This metalens could resolve the 1-μm fractal features and confocal microscopy mapping of the focus profile also showed a FWHM of 0.94 µm, which was close to the diffraction limit of 0.91 µm (**Figure 4.21**).

The current lens designs were not corrected for spherical aberrations which reduced the sharpness of the images produced and limited resolution at off-normal incident angles. **Figure 4.19** shows the focal point profiles of two metalens designs while illuminated at off-normal angles calculated by FDTD simulations. The focal points shifted toward the lenses and broadened as incident angle increased over

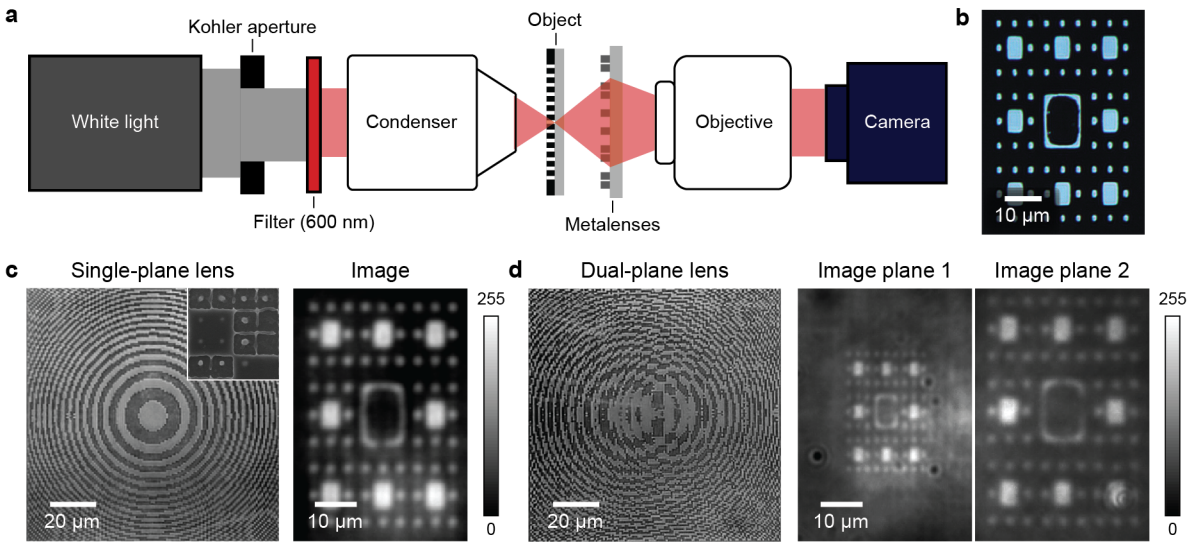

Figure 4.18. PMMA-NP metalenses for optical imaging of fractal patterns. (**a**) Scheme depicting the setup of imaging measurement. (**b**) Optical microscopy image for patterns of Sierpinski carpet on a 30-nm Cr film to be imaged. (left) Monochromatic optical microscopy images of PMMA-NP metalenses designed for (**c**) a single focus at $f = 160$ μm and (**d**) two foci at $f = 120$ and 160 μm with an in-plane shift $x = \pm 10$ μm and (right) the corresponding images formed on the image planes at $\lambda = 600$ nm, respectively. Images in (c) and (d) were auto-scaled by ImageJ in 8-bit gray scale. Insets in (c) show SEM images (1.6 μm × 1.6 μm) of PMMA patterns. The optical images produced by metalenses were captured by a monochromatic camera. The PMMA film (thickness $t = 100$ nm) were patterned by the EBL process on a periodic array of Ag NPs ($a_0 = 400$ nm, $h = 50$ nm, and $d = 84$ nm). The metalens had a numerical aperture NA = 0.33 (0.42) for focal length $f = 160$ μm (120 μm). The separation between the fractal object and the metalens was roughly 270 μm.

$\theta = 5°$. Also, the focal intensity decreased when illuminated at off-normal angles because (1) the focus FWHM increased and (2) the SLR wavelength shifted away from the imaging wavelength so the plasmonic enhancement decreased.

We designed the metalens for two focal points at (1) $f = 120$ μm, $x =$ -10 μm and (2) $f = 160$ μm, $x = 10$ μm. **Figure 4.18d** shows images of the same fractal pattern using a two-foci metalens with $f =$ 120 and 160 μm. This multi-focal lens produced two images with 0.8× and 1.45× the size of the object in $z = 215$ and 395 μm, respectively. The 0.8× (1.45×) image was defocused and indistinguishable from the background on z = 395 μm (215 μm) (**Figure 4.20**). Compared to images formed by a single focal lens, these images showed comparable resolution but lower brightness.

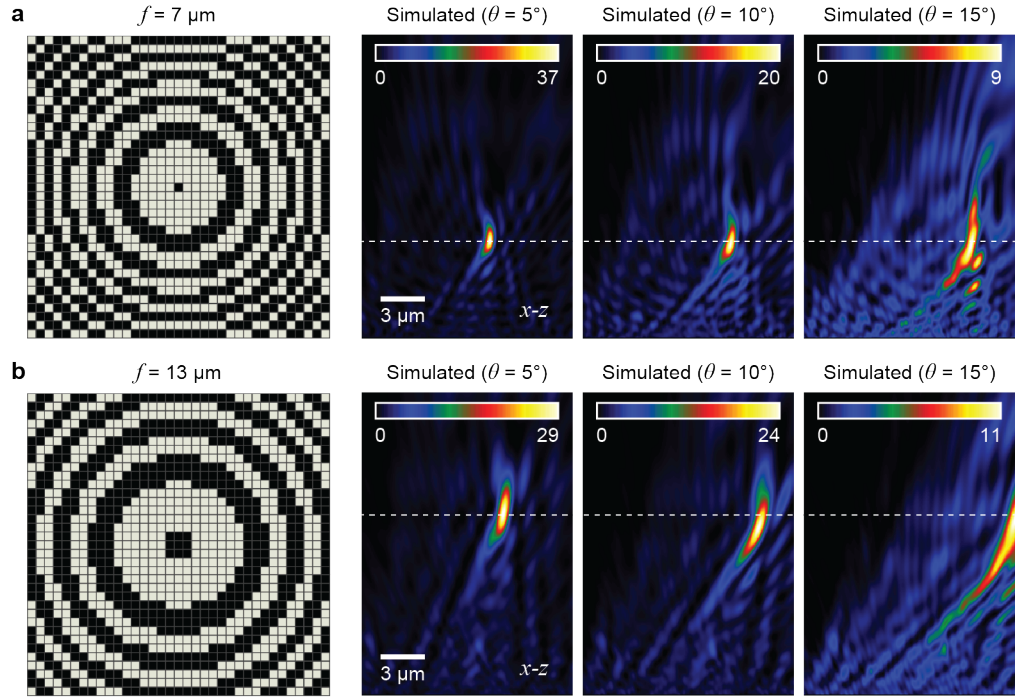

Figure 4.19. Metalenses can focus plane-wave light with off-normal incident angles. Schemes and the corresponding far-field light profiles of metalenses with focal distances (**a**) $f = 7$ μm and (**b**) $f = 13$ μm. The metalenses have a footpint of 14 μm $\times$ 14 μm. The x-z optical profiles were calculated by FDTD simulations at a wavelength $\lambda = 600$ nm.

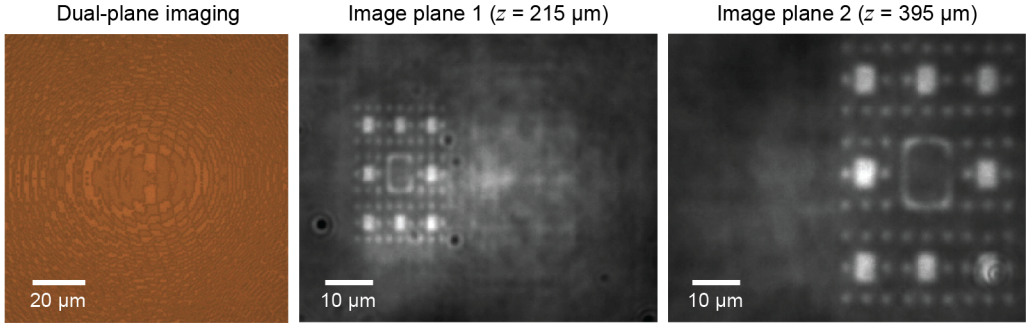

Figure 4.20. PMMA-NP metalenses for multi-plane imaging. (left) Optical microscopy images of the metalens optimized to have two foci at $f = 120$ and 160 μm with an in-plane shift $x = \pm 10$ μm. (Middle) The image formed by the focal point at $f = 120$ μm on the plane $z = 215$ μm at $\lambda = 600$ nm. (Right) The image formed by the focal point at $f = 160$ μm on the plane $z = 395$ μm. The separation between the fractal object and the metalens was roughly 270 μm.

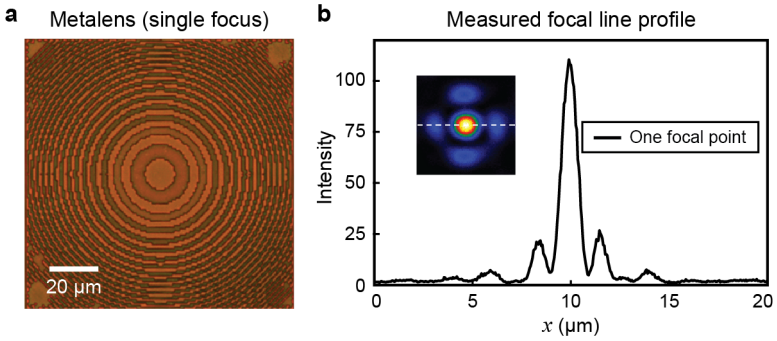

Figure 4.21. Lattice-resonance metalens for single point imaging. (**a**) Optical microscopy image of a single-focus metalens and (**b**) a focal point intensity line profile extracted from the confocal microscopy mapping. The lens was designed for $f = 160$ μm.

4.3. Reconfigurable Lensing by Solvent-Based Soft Lithography

This section demonstrate a scalable methods based on nanoscale embossing for adaptive imaging using a polymeric resist on arrays of plasmonic NPs. We realized large-area metalens reconfiguration by reforming the dielectric blocks on the plasmonic NP surface with solvent-assisted nanoscale embossing (SANE). SANE could reversibly switch the substrate between two (or more) lens designs with no observable degradation in feature quality. Finally, we showed adaptive lensing by evolving a SLR metalens sequentially from a single- to multi-focal point configurations during the same experiment. **Figure 4.22** depicts a scheme of our SLR metalens that can be reconfigured by SANE. This method allows customization of metalenses for both single- and multi-plane imaging, without requiring additional materials or fabrication of separate devices for each property.

4.3.1. Large-area patterning of metalenses by nanoscale embossing

To scale their production, we developed a process to pattern metalenses by SANE. This method could transfer LEA-optimized patterns into polymer blocks from PDMS masks, which were wet with dimethylformamide (DMF) and then placed into conformal contact with the polymer film. We used SU-8 epoxy (Micro Chem, $n = 1.59$) as the superstrate material because of high optical transparency and solubility in DMF. We also switched the substrate material from fused silica to glass ($n = 1.52$) to minimize the index mismatch with the SU-8. **Figure 4.23a** shows the preparation steps for soft PDMS masks for

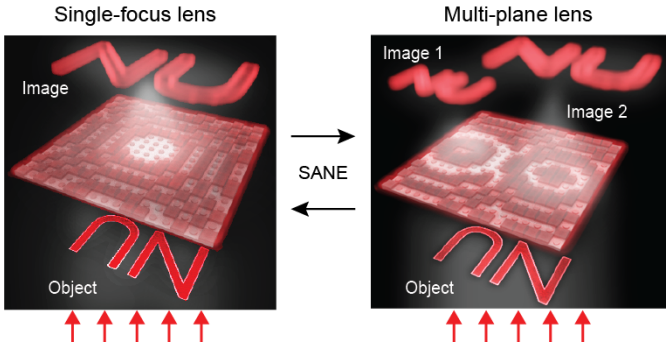

Figure 4.22. Lattice resonances enabled reconfigurable metalenses for imaging. Reconfigurable metalenses for tunable multi-plane imaging enabled by solvent-assisted nanoscale embossing (SANE).[14]

SANE, including (1) creating Cr lens patterns in pre-patterned Cr holes by electron-beam lithography; (2) transferring the structures into Si by dry etching; and (3) molding PDMS stamps against the Si templates. The initial Cr patterns were transferred into micron-scale trenches in PDMS surfaces that functioned as solvent reservoirs and facilitated uniform SU-8 distribution across the sample. Because SU-8 has a higher index than PMMA, we reduced the NP size to 66 nm to keep the SLR wavelength at $\lambda = 600$ nm. We modeled the optical response of the Ag NPs in randomly patterned SU-8 blocks by FDTD simulations. The SANE patterning process left residual films around the Ag NPs and the film thickness was comparable to the NP height. **Figure 4.24** shows the calculated transmission spectra of a 35×35 patch with 60% randomly selected NPs covered by SU-8 blocks. The SLR in SU-8 exhibited comparable to PMMA-AgNPs but smaller FWHM because the reduced NP diameter.

Figure 4.23b shows optical microscopy images of the initial Cr template with 25-μm holes, the Si master, and the lens array in an SU-8 film. In *ca.* 45 minutes, SANE produced metalens arrays over cm^2 areas while patterning subwavelength phase blocks of SU-8. Although the NPs were not always centered within SU-8 blocks, FDTD calculations indicated that the SLR metasurface optical responses were robust to both translational and rotational misalignments between the NP lattice and SU-8 patterns (**Figure 4.25**).

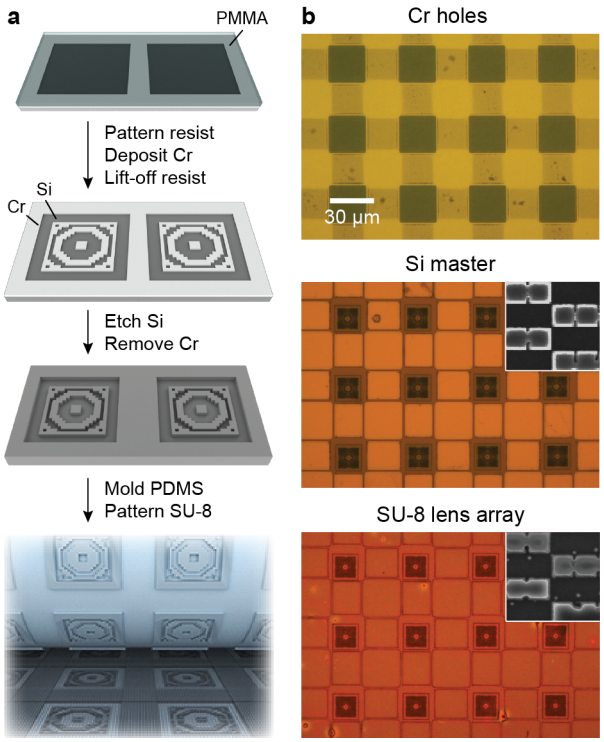

Figure 4.23. Solvent-assisted nanoembossing can pattern metasurfaces over large areas. (**a**) Scheme depicting the preparation of polydimethylsiloxane (PDMS) masks with metasurface patterns and the parallel reconfiguration process. (**b**) Optical microscopy images of (upper) Cr templates, (middle) Si masters, and (lower) patterned SU-8 (on Ag NPs) of metalens arrays with $f = 7$ μm on a 14 μm $\times$ 14 μm footprint. Insets in (b) show SEM images (1.6 μm $\times$ 1.6 μm) of the Si template and the SU-8 patterns on the NPs.

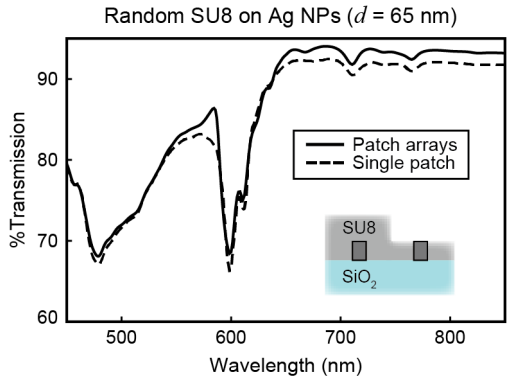

Figure 4.24. Lattice plasmon resonances can be excited on finite patches of Ag NPs in SU8 thin films.

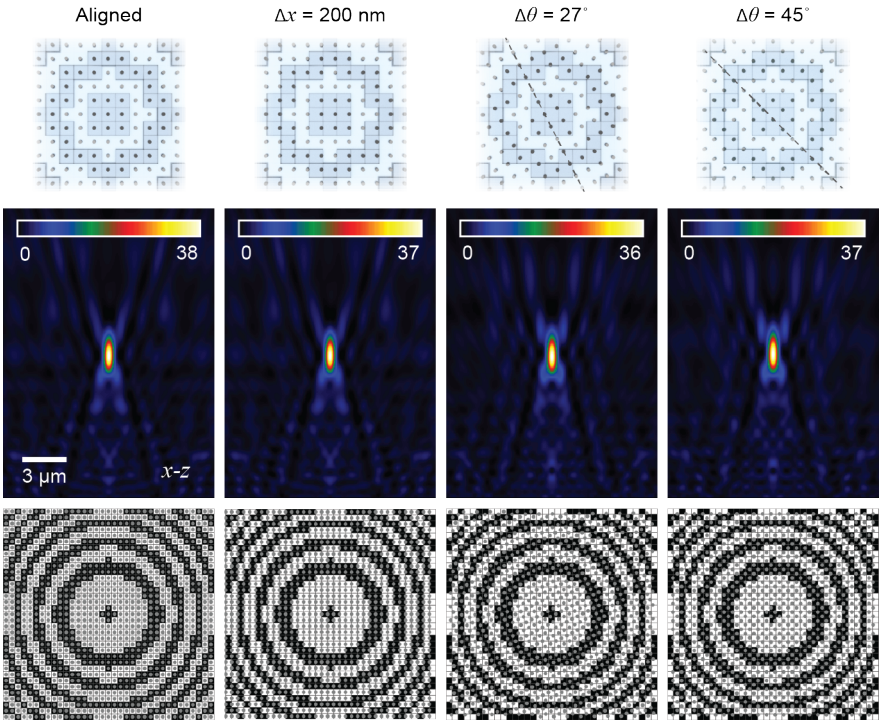

Figure 4.25. Single-focal metalens designs can tolerate translational and rotational misalignment between dielectric patterns and NP lattices. Schemes of plasmonic lattice lenses and the corresponding far-field light profiles of designs (f = 10 μm) with perfect alignment, lateral misalignment of Δx = 200 nm, rotational misalignment of $\Delta\theta = 27°$, and $\Delta\theta = 45°$. The optical profiles were calculated by FDTD simulations at λ = 600 nm. The NP array spacing a_0 = 400 nm, height h = 40 nm, and diameter d = 84 nm.

4.3.2. Multicycle reversible switching between metalens configurations

SANE was also used to reconfigure SLR-metalenses by erasing existing patterns with solvent and defining new features with single-step embossing. **Figure 4.26a** demonstrates switching between two metasurface configurations using two PDMS masks, where mask 1 (M1) and mask 2 (M2) had lens patterns for three and four foci, respectively, in the z = 7 μm plane. Optical microscopy images revealed that SANE could completely remove the existing dielectric metasurfaces and form a new pattern with high fidelity. Using alignment makers, we further confirmed that the polymer patterns and metalenses can be erased by the embossing process before forming new patterns in a single SANE step. **Figure 4.27** shows the optical microscopy image of metalens patterns on the same SU8-AgNP substrate before and after SANE

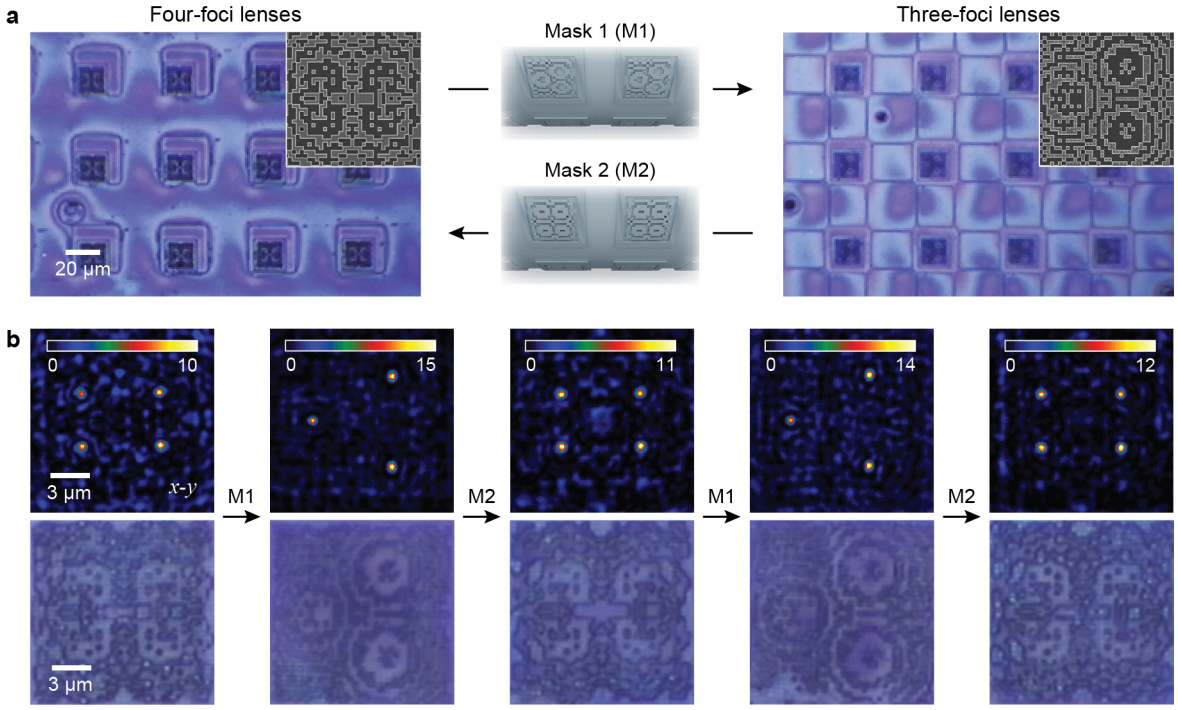

Figure 4.26. SANE can reconfigure metalenses in parallel. (**a**) Optical microscopy images depicting two microlens arrays that could be converted reversibly. (**b**) (lower) Optical microscopy images of lattice resonance metasurfaces and (upper) the corresponding confocal microscopy images ($\lambda = 600$ nm). The lattices were optimized to produce (cycles 1, 3, and 5) four focal points at $x = \pm 3$ μm, $y = \pm 2$ μm, and $z = 7$ μm and (cycles 2 and 4) three focal points separated from the lattice center by $r = 4$ μm at $z = 5$ μm plane. The insets in (a) showed the SEM images of the patterns on Si master.

patterning. A tape was placed on the back of the silica slide as a position marker. Comparison between the two images showed that SANE could erase the existing patterns completely before transferring the new patterns.

Figure 4.26b shows metalens structures and their far-field light profile from the same NP substrate at five consecutive SANE steps. The SU-8-Ag NP lenses maintained light profiles with comparable focal intensities after sequential reconfigurations. **Figure 4.28** shows SEM images for metalens designs after 10 cycles of embossing. These lens patterns showed no structural defects and demonstrated the robustness of our reconfiguration method. This multi-step tuning process showed the robustness of our reconfiguration strategy based on the materials-conserving embossing process that exhibited no SU-8 lost

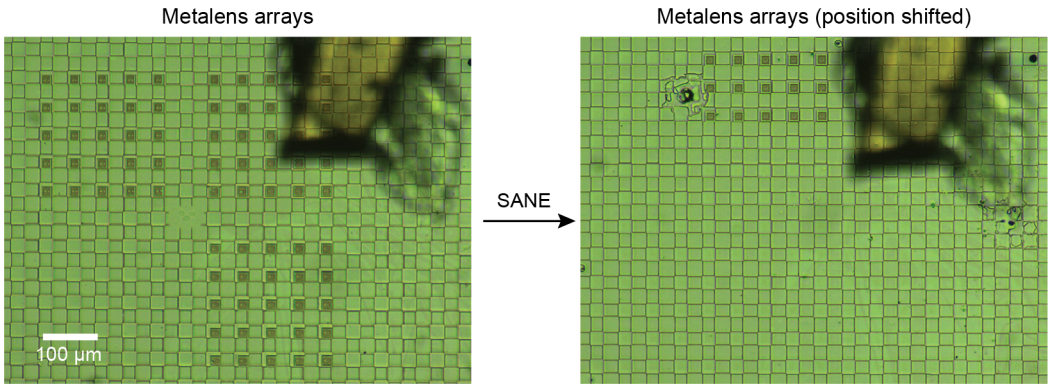

Figure 4.27. Single-step erase and write of SU-8 patterns by SANE. Optical microscopy images of a SU8-NP substrate with metalens arrays before and after a SANE patterning step. The SANE process erased existing patterns completely and formed new metalenses with nanoscale feature resolution.

from the sample. Although each SANE step required 45 minutes for the solvent to evaporate, this process can be shortened by heating the substrate during patterning.

4.3.3. Reconfigurable metalenses for adaptive imaging

Finally, we showed how tunable SLR-metalenses could be used for reconfigurable imaging. To accommodate the 110-μm imaging lenses, we re-designed the Cr reservoir patterns with 125-μm square holes with additional 15-μm square holes added in between to reduce PDMS collapse[92] during the SANE process (Figure 4.29b). To pattern arrays of metalenses for imaging, we prepatterned hierarchical square Cr holes (125×125 μm^2 and 15×15 μm^2) on a silicon substrate (**Figure 4.29a**). The arrays of metalenses with a 110×110 μm^2 footprint were patterned in the 125×125 μm^2 holes by EBL, Cr deposition, and deep reactive-ion etching (**Figure 4.29b**). The metalens patterns were transferred to the SU-8 superstrate layer by the SANE process using a PDMS mask molded on the silicon template (**Figure 4.29c**).

We designed metalenses for two and four focal points for multi-focal imaging (**Figure 4.30a,c**). We also measured the focal points light profiles in the x-y plane at z = 160 μm and the line intensity profiles across the focal points (**Figure 4.30b,d**). **Figure 4.31** shows the evolution of a SU-8 surface from a single-focus lens to two- and four-foci metasurfaces and the resulting optical images. We realized

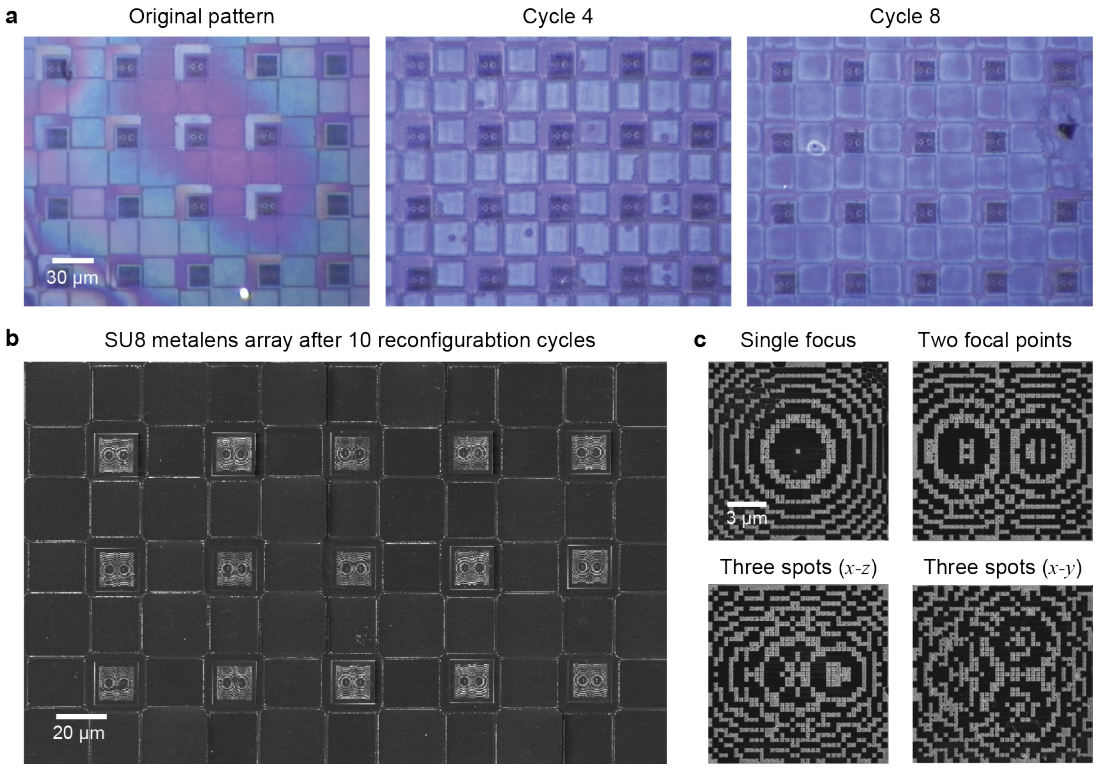

Figure 4.28. SU-8 patterns after cycles of reconfiguration. (**a**) Optical microscopy images of a original 2-foci lens array patterned on SU8-AgNP substrate and the reconfigured pattern in cycles 4 and 8. (**b**) The SEM image of the 2-foci lens array after 10 patterning cycles and (**c**) the zoomed-in images for four lens designs after 10 reconfiguration processes.

on-demand generation of a single image or multiple images from a micron-size object ("NU") at programmable locations by reconfiguring the same plasmonic NP array. Compared with single- focal-point lenses, images produced by multi-focal metalenses had reduced clarity because the foci deviating from the optical axis had smaller NA and therefore larger FWHM (**Figure 4.30**). The light spots in the four-foci lenses exhibited elliptical shapes because of the difference in NA along the short and long axes of the foci.

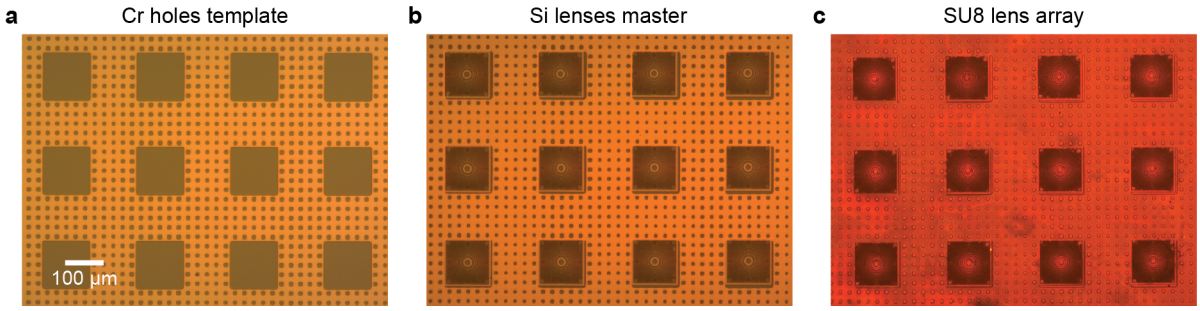

Figure 4.29. Optical microscopy images of (**a**) prepatterned Cr templates, (**b**) fabricated Si master and (right) SU-8 patterns of metalens arrays on a 110 μm $\times$ 110 μm footprint. The larger square holes were 125 μm in size and had a spacing of 250 μm. The smaller square holes were 15 μm in size and had a spacing of 25 μm.

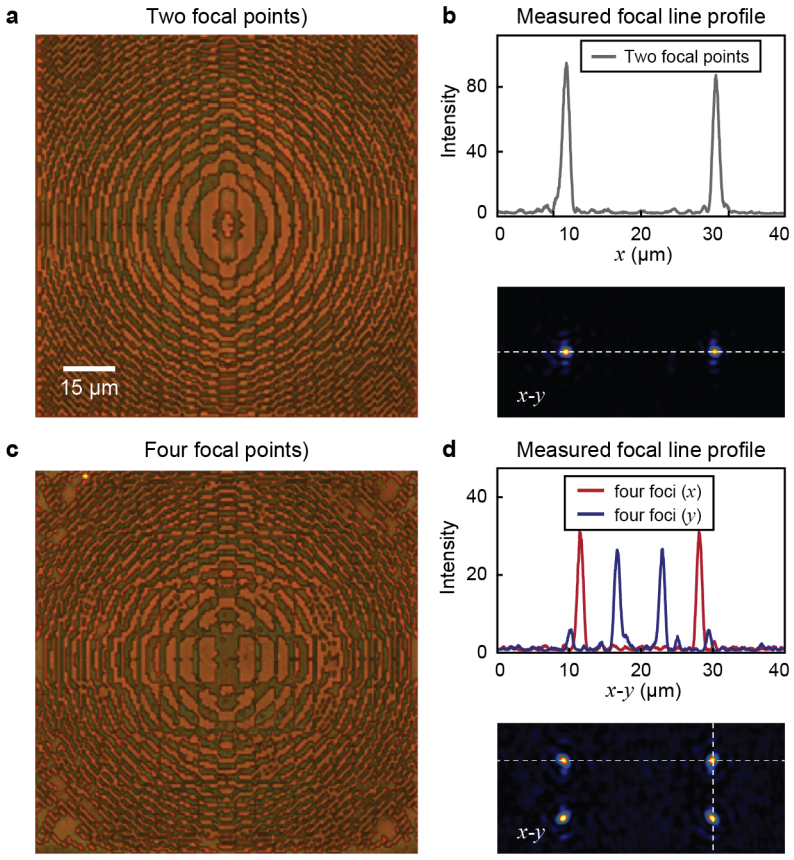

Figure 4.30. Lattice-resonance metalenses for multi-focal imaging. Optical microscopy images of (**a**) two focal points ($x = \pm 10$ μm, $y = 0$), and (**c**) four focal points ($x = \pm 10$ μm, $y = \pm 4$ μm) on the $f = 160$ μm plane at $\lambda = 600$ nm and (**b**, **d**) their corresponding intensity line profiles extracted from the confocal microscopy mapping.

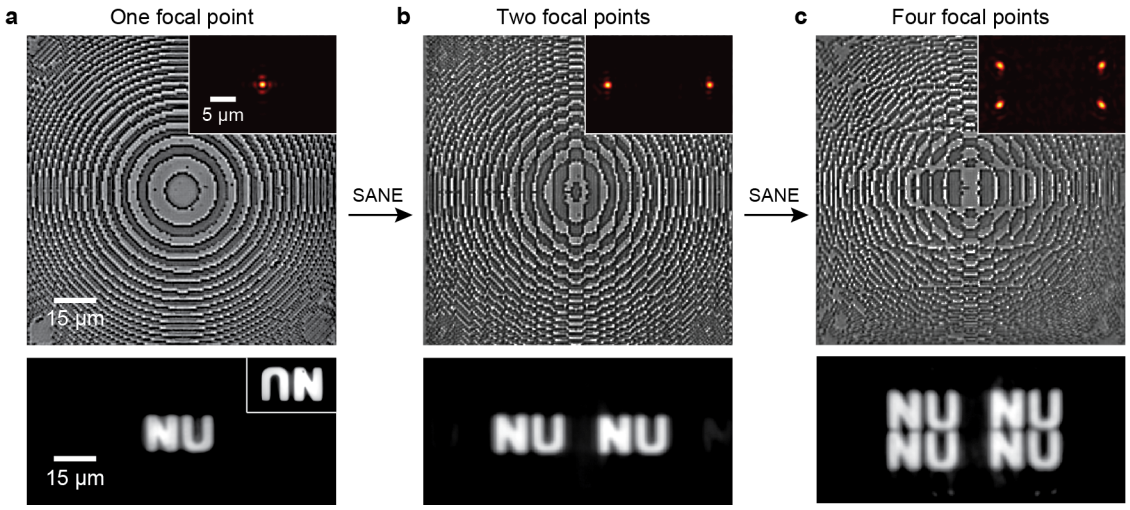

Figure 4.31. Single to multi-focal imaging by reconfigurable NP metalenses. (upper) Structures of SU-8 metasurface patterns for (**a**) one focal point, (**b**) two focal points ($x = \pm 10$ μm, $y = 0$), and (**c**) four focal points ($x = \pm 10$ μm, $y = \pm 4$ μm) on the $f = 160$ μm plane at $\lambda = 600$ nm and (lower) the corresponding optical images of "NU" produced. The optical images were captured by a monochromatic camera. The microlens SU-8 patterns ($t = 190$ nm) were reconfigured by SANE on a periodic array of Ag NPs.

4.4. Summary of Reconfigurable Metalenses on Coupled Plasmonic Aanoparticle Arrays

I demonstrate fully-reconfigurable metalenses on a 2D NP lattice for 3D imaging at visible wavelengths. By tailoring SLR-enhanced optical field intensity on the NP lattice with superstrate index patterns, we manipulated the wavefront for light focusing and achieved metalens designs that could produce images on multiple planes concurrently. I further showed adaptive imaging by evolving metalenses from a single focus to multi-focal configurations in a high-throughput patterning process. Overall, control of light by SLR resonances offers a strategy to realize versatile, dynamic metasurfaces based on rapid, subwavelength structural changes. The combination of this tunable platform with predictive design will open new prospects for developing compact imaging systems and optoelectronics devices.

4.5. METHODS

4.5.1. Finite-difference time-domain simulations

Calculations based on commercial software (FDTD Solution, Lumerical Inc., Vancouver, Canada) were used to simulate the linear properties (far-field and near-field) of coupled plasmonic NPs. The optical constants of Ag were obtained from a reported Kramers-Kronig analysis based on absorptivity measurements.[45] The dielectric properties of PMMA and SU-8 photoresist were taken from ellipsometry measurements and imported to the materials database of Lumerical FDTD. In calculations of periodic Ag NP arrays, a mesh-override size of 2 nm was imposed on the single NP and periodic boundary conditions were used in x-y directions. A uniform mesh of 6 nm was imposed on NPs for simulations of the full SLR-metalens structures (35×35 NP patch). The electric fields in x-y directions were recorded and exported by a frequency-domain monitor. The exported fields were imported as a single-wavelength source into a 15 μm × 15 μm × 30 μm simulation with a uniform mesh size of 50 nm to calculate the far-field light profiles.

4.5.2. Lattice evolution algorithm calculations

The LEA was implemented with object-oriented programming to solve for focal points with arbitrary spatial arrangements. The LEA started with a population of random structures represented by binary strings of 1 (a NP surrounded by dielectrics) and 0 (the identical NP exposed to air). With an inverse-form fitness function defined based on the target foci, the method iteratively constructed the next generation by giving the structures with larger fitness values a larger change to survive and duplicate. The algorithm terminated and exported the optimized the lattice when the optimal fitness value stayed constant for 30 generations. To account for materials properties and plasmonic coupling, the electric field components of light transmitted by the two types of unit cells were calculated by FDTD simulations with periodic boundary condition and exported into text files for LEA calculations. The fitness was evaluated by linearly superimposing the field components contributed by each lattice unit.

4.5.3. Fabrication of coupled nanoparticle arrays

Ag NP arrays were fabricated over cm^2-scale areas using Au nanohole arrays as deposition masks. To prepare the Au masks, a PDMS mask with lines (lattice spacing $a_0 = 400$ nm) was used in phase-shifting photolithography.[93] Photoresist posts with diameter $d = 80$ nm were prepared on Si (100) wafers by exposing line PDMS masks twice for 1.5 s at a 90° angle. After a thin layer of Cr (10 nm) was deposited and lift-off of photoresist posts, cylindrical pits (diameter 80 nm, depth 200 nm) were produced in Si using Cr holes as the mask by deep reactive ion etching. Au nanohole arrays were then produced by depositing a 100-nm layer of Au and etching of the Cr sacrificial layer. Au nanohole arrays were floated onto substrates (treated by oxygen plasma) as deposition masks. A deposition of 50-nm Ag and removal of the Au mask by tape resulted in periodic arrays of Ag NPs on silica substrate. A 5-nm conformal coating of alumina on the NPs was deposited by atomic layer deposition.

4.5.4. Superstrate resist film preparation

We prepared 140-nm PMMA films by spin-coating PMMA 950 a3 (MicroChem) at 4000 rpm for 45 s and baking at 180 °C for 90 s. To prepare a 160-nm SU-8 film, we diluted 1 g of SU-8 2010 (MicroChem) in 11 g of cyclopentanone, spin-coated at 3000 rpm for 45 s, and baked at 95 °C for 2 min.

4.5.5. Confocal measurements of NP lattice lenses

A confocal scanning optical microscope (WITec alpha-300) was used to measure the light profiles generated from plane-wave light incident on the lattice lenses. A fiber-coupled super continuum laser (Koheras SuperK Power Plus) with an acousto-optic tunable filter (AOTF, Koheras Spectrack Dual NIR + 4xVIS) and collimator (Thorlabs F280FC-780) were used to generate the collimated incident beam. A polarizer (Thorlabs 10GL08) was used when linearly polarized incident light was required. The lenses were measured in air by 100× air objective (Nikon Plan Fluor, NA = 0.90), and transmitted photons were collected by a photomultiplier tube (PMT, Hamamatsu Photonics H8259-01). The scan resolution was 50 nm using an integration time of 0.01 s/pixel for all measurements.

References

[1] Wave Optics, chapter 2, pages 41–79 John Wiley & Sons, Ltd**2001**.

[2] Electromagnetic Optics, chapter 5, pages 157–192 John Wiley & Sons, Ltd**2001**.

[3] Miller, O. E.; McLeod, J. H.; Sherwood, W. T., Thin sheet plastic fresnel lenses of high aperture. *Journal of the Optical Society of America* **1951**, *41* (11), 807–815.

[4] Sierra, C.; Vázquez, A. J., High solar energy concentration with a fresnel lens. *Journal of Materials Science* **2005**, *40* (6), 1339–1343.

[5] Sinzinger, S.; Testorf, M., Transition between diffractive and refractive micro-optical components. *Applied Optics* **1995**, *34* (26), 5970–5976.

[6] Yang, J.; Xu, S.; Zhang, J.; Wu, W.; Lu, H.; Huang, J.; Chen, D., Perfect shuffle transform based on subwavelength binary blazed grating. **2015**.

[7] Yu, N.; Genevet, P.; Kats, M. A.; Aieta, F.; Tetienne, J.-P.; Capasso, F.; Gaburro, Z., Light propagation with phase discontinuities: Generalized laws of reflection and refraction. *Science* **2011**, *334* (6054), 333–337.

[8] Ni, X.; Ishii, S.; Kildishev, A. V.; Shalaev, V. M., Ultra-thin, planar, babinet-inverted plasmonic metalenses. *Light: Science & Applications* **2013**, *2*, e72.

[9] Khorasaninejad, M.; Chen, W. T.; Devlin, R. C.; Oh, J.; Zhu, A. Y.; Capasso, F., Metalenses at visible wavelengths: Diffraction-limited focusing and subwavelength resolution imaging. *Science* **2016**, *352* (6290), 1190–1194.

[10] Yu, N.; Aieta, F.; Genevet, P.; Kats, M. A.; Gaburro, Z.; Capasso, F., A broadband, background-free quarter-wave plate based on plasmonic metasurfaces. *Nano Letters* **2012**, *12* (12), 6328–6333. PMID: 23130979.

[11] Ni, X.; Kildishev, A. V.; Shalaev, V. M., Metasurface holograms for visible light. *Nature Communications* **2013**, *4*, 2807.

[12] Zheng, G.; MÃ¼hlenbernd, H.; Kenney, M.; Li, G.; Zentgraf, T.; Zhang, S., Metasurface holograms reaching 80% efficiency. *Nature Nanotechnology* **2015**, *10*, 308–312.

[13] Huntington, M. D.; Lauhon, L. J.; Odom, T. W., Subwavelength lattice optics by evolutionary design. *Nano Letters* **2014**, *14* (12), 7195–7200. PMID: 25380062.

[14] Lee, M. H.; Huntington, M. D.; Zhou, W.; Yang, J.-C.; Odom, T. W., Programmable soft lithography: Solvent-assisted nanoscale embossing. *Nano Letters* **2011**, *11* (2), 311–315. PMID: 20687596.

[15] Sonneveld, P.; Swinkels, G.; van Tuijl, B.; Janssen, H.; Campen, J.; Bot, G., Performance of a concentrated photovoltaic energy system with static linear fresnel lenses. *Solar Energy* **2011**, *85* (3), 432 – 442.

[16] Fujita, T.; Nishihara, H.; Koyama, J., Blazed gratings and fresnel lenses fabricated by electron-beam lithography. *Optics Letters* **1982**, *7* (12), 578–580.

[17] Haruna, M.; Takahashi, M.; Wakahayashi, K.; Nishihara, H., Laser beam lithographed micro-fresnel lenses. *Applied Optics* **1990**, *29* (34), 5120–5126.

[18] Ni, X.; Emani, N. K.; Kildishev, A. V.; Boltasseva, A.; Shalaev, V. M., Broadband light bending with plasmonic nanoantennas. *Science* **2012**, *335* (6067), 427–427.

[19] Li, Z.; Palacios, E.; Butun, S.; Aydin, K., Visible-frequency metasurfaces for broadband anomalous reflection and high-efficiency spectrum splitting. *Nano Letters* **2015**, *15* (3), 1615–1621. PMID: 25664815.

[20] Gao, S.; Yue, W.; Park, C.-S.; Lee, S.-S.; Kim, E.-S.; Choi, D.-Y., Aluminum plasmonic metasurface enabling a wavelength-insensitive phase gradient for linearly polarized visible light. *ACS Photonics* **2017**, *4* (2), 322–328.

[21] Khorasaninejad, M.; Zhu, A. Y.; Roques-Carmes, C.; Chen, W. T.; Oh, J.; Mishra, I.; Devlin, R. C.; Capasso, F., Polarization-insensitive metalenses at visible wavelengths. *Nano Letters* **2016**, *16* (11), 7229–7234. PMID: 27791380.

[22] Arbabi, A.; Arbabi, E.; Kamali, S. M.; Horie, Y.; Han, S.; Faraon, A., Miniature optical planar camera based on a wide-angle metasurface doublet corrected for monochromatic aberrations. *Nature Communications* **2016**, *7*, 13682.

[23] Wang, S.; Wu, P. C.; Su, V.-C.; Lai, Y.-C.; Hung Chu, C.; Chen, J.-W.; Lu, S.-H.; Chen, J.; Xu, B.; Kuan, C.-H.; Li, T.; Zhu, S.; Tsai, D. P., Broadband achromatic optical metasurface devices. *Nature Communications* **2017**, *8*, 187.

[24] Wang, S.; Wu, P. C.; Su, V.-C.; Lai, Y.-C.; Chen, M.-K.; Kuo, H. Y.; Chen, B. H.; Chen, Y. H.; Huang, T.-T.; Wang, J.-H.; Lin, R.-M.; Kuan, C.-H.; Li, T.; Wang, Z.; Zhu, S.; Tsai, D. P., A broadband achromatic metalens in the visible. *Nature Nanotechnology* **2018**, *13*, 227.

[25] Arbabi, A.; Horie, Y.; Bagheri, M.; Faraon, A., Dielectric metasurfaces for complete control of phase and polarization with subwavelength spatial resolution and high transmission. *Nature Nanotechnology* **2015**, *10*, 937.

[26] Wu, P. C.; Tsai, W.-Y.; Chen, W. T.; Huang, Y.-W.; Chen, T.-Y.; Chen, J.-W.; Liao, C. Y.; Chu, C. H.; Sun, G.; Tsai, D. P., Versatile polarization generation with an aluminum plasmonic metasurface. *Nano Letters* **2017**, *17* (1), 445–452. PMID: 27935318.

[27] Wang, B.; Dong, F.; Li, Q.-T.; Yang, D.; Sun, C.; Chen, J.; Song, Z.; Xu, L.; Chu, W.; Xiao, Y.-F.; Gong, Q.; Li, Y., Visible-frequency dielectric metasurfaces for multiwavelength achromatic and highly dispersive holograms. *Nano Letters* **2016**, *16* (8), 5235–5240. PMID: 27398793.

[28] Gao, H.; Hyun, J. K.; Lee, M. H.; Yang, J.-C.; Lauhon, L. J.; Odom, T. W., Broadband plasmonic microlenses based on patches of nanoholes. *Nano Letters* **2010**, *10* (10), 4111–4116. PMID: 20839781.

[29] Fourier Optics, chapter 4, pages 108–156 John Wiley & Sons, Ltd**2001**.

[30] Yu, N.; Capasso, F., Flat optics with designer metasurfaces. *Nature Materials* **2014**, *13*, 139.

[31] Gordon, R.; Brolo, A. G.; McKinnon, A.; Rajora, A.; Leathem, B.; Kavanagh, K. L., Strong polarization in the optical transmission through elliptical nanohole arrays. *Physical Review Letters* **2004**, *92*, 037401.

[32] Kildishev, A. V.; Boltasseva, A.; Shalaev, V. M., Planar photonics with metasurfaces. *Science* **2013**, *339* (6125).

[33] Babicheva, V. E.; Kinsey, N.; Naik, G. V.; Ferrera, M.; Lavrinenko, A. V.; Shalaev, V. M.; Boltasseva, A., Towards cmos-compatible nanophotonics: Ultra-compact modulators using alternative plasmonic materials. *Optics Express* **2013**, *21* (22), 27326–27337.

[34] Li, W.; Guler, U.; Kinsey, N.; Naik, G. V.; Boltasseva, A.; Guan, J.; Shalaev, V. M.; Kildishev, A. V., Refractory plasmonics with titanium nitride: Broadband metamaterial absorber. *Advanced Materials 26* (47), 7959–7965.

[35] Guler, U.; Shalaev, V. M.; Boltasseva, A., Nanoparticle plasmonics: going practical with transition metal nitrides. *Materials Today* **2015**, *18* (4), 227–237.

[36] Naik, G. V.; Shalaev, V. M.; Boltasseva, A., Alternative plasmonic materials: Beyond gold and silver. *Advanced Materials 25* (24), 3264–3294.

[37] Gui, L.; Bagheri, S.; Strohfeldt, N.; Hentschel, M.; Zgrabik, C. M.; Metzger, B.; Linnenbank, H.; Hu, E. L.; Giessen, H., Nonlinear refractory plasmonics with titanium nitride nanoantennas. *Nano Letters* **2016**, *16* (9), 5708–5713. PMID: 27494639.

[38] Guler, U.; Ndukaife, J. C.; Naik, G. V.; Nnanna, A. G. A.; Kildishev, A. V.; Shalaev, V. M.; Boltasseva, A., Local heating with lithographically fabricated plasmonic titanium nitride nanoparticles. *Nano Letters* **2013**, *13* (12), 6078–6083. PMID: 24279759.

[39] Pors, A.; Bozhevolnyi, S. I., Gap plasmon-based phase-amplitude metasurfaces: material constraints. *Optical Materials Express* **2015**, *5* (11), 2448–2458.

[40] Murai, S.; Fujita, K.; Daido, Y.; Yasuhara, R.; Kamakura, R.; Tanaka, K., Plasmonic arrays of titanium nitride nanoparticles fabricated from epitaxial thin films. *Opt. Express* **2016**, *24* (2), 1143–1153.

[41] Fellows, M. R.; Fomin, F. V.; Lokshtanov, D.; Rosamond, F.; Saurabh, S.; Villanger, Y., Local search: Is brute-force avoidable? *Journal of Computer and System Sciences* **2012**, *78* (3), 707 – 719. In Commemoration of Amir Pnueli.

[42] Marler, R.; Arora, J., Survey of multi-objective optimization methods for engineering. *Structural and Multidisciplinary Optimization* **2004**, *26* (6), 369–395.

[43] Fonseca, C. M.; Fleming, P. J., Genetic algorithms for multiobjective optimization: Formulationdiscussion and generalization. In Proceedings of the 5th International Conference on Genetic Algorithms Morgan Kaufmann Publishers Inc., San Francisco, CA, USA**1993** pages 416–423.

[44] Reed, J. M.; Ferdinandus, M. R.; Kinsey, N.; DeVault, C.; Guler, U.; Shalaev, V. M.; Boltasseva, A.; Urbas, A., Transient nonlinear refraction measurements of titanium nitride thin films. In 2016 Conference on Lasers and Electro-Optics (CLEO), **2016** pages 1–2.

[45] Guo, S. . .; Ding, X. J. . .; Zhang, J. Z. . .; Hu, Z. G. . .; Ji, X. L. . .; Wu, L. C. . .; Song, Z. T. . .; Chu, J. H. . ., Intrinsic evolutions of dielectric function and electronic transition in tungsten doping ge2sb2te5 phase change films discovered by ellipsometry at elevated temperatures. *Applied Physics Letters* **2015**, *106* (5), 052105.

[46] Huntington, M. D.; Engel, C. J.; Hryn, A. J.; Odom, T. W., Polymer nanowrinkles with continuously tunable wavelengths. *ACS Applied Materials & Interfaces* **2013**, *5* (13), 6438–6442. PMID: 23758140.

[47] Rioux, D.; Vallières, S.; Besner, S.; Muñoz, P.; Mazur, E.; Meunier, M., An analytic model for the dielectric function of au, ag, and their alloys. *Advanced Optical Materials* **2014**, *2* (2), 176–182.

[48] Sarkar, D.; Modak, J. M., Pareto-optimal solutions for multi-objective optimization of fed-batch bioreactors using nondominated sorting genetic algorithm. *Chemical Engineering Science* **2005**, *60* (2), 481 – 492.

[49] Murata, T.; Ishibuchi, H., Moga: Multi-objective genetic algorithms. **1995** page 289.

[50] Lin, J., Multiple-objective problems: Pareto-optimal solutions by method of proper equality constraints. *IEEE Transactions on Automatic Control* **1976**, *21* (5), 641–650.

[51] Ali, M. Y.; Hung, W.; Yongqi, F., A review of focused ion beam sputtering. *International Journal of Precision Engineering and Manufacturing* **2010**, *11* (1), 157–170.

[52] Verslegers, L.; Catrysse, P. B.; Yu, Z.; White, J. S.; Barnard, E. S.; Brongersma, M. L.; Fan, S., Planar lenses based on nanoscale slit arrays in a metallic film. *Nano Letters* **2009**, *9* (1), 235–238. PMID: 19053795.

[53] Timilsina, R.; Tan, S.; Livengood, R.; Rack, P. D., Monte carlo simulations of nanoscale focused neon ion beam sputtering of copper: elucidating resolution limits and sub-surface damage. *Nanotechnology*

2014, *25* (48), 485704.

[54] Pakpum, C.; Pussadee, N., Deep reactive ion etching of alumina titanium carbide using chlorine-based plasma. *Surface and Coatings Technology* **2016**, *306*, 194 – 199. The 19th International Conference on Surface Modification of Materials by Ion Beams [SMMIB2015].

[55] Xie, W.; Dai, Y.; Wang, R.; Sumathy, K., Concentrated solar energy applications using fresnel lenses: A review. *Renewable and Sustainable Energy Reviews* **2011**, *15*, 2588–2606.

[56] Xie, W.; Dai, Y.; Wang, R., Thermal performance analysis of a line-focus fresnel lens solar collector using different cavity receivers. *Solar Energy* **2013**, *91*, 242 – 255.

[57] Kodate, K.; Tokunaga, E.; Tatuno, Y.; Chen, J.; Kamiya, T., Efficient zone plate array accessor for optoelectronic integrated circuits: design and fabrication. *Applied Optics* **1990**, *29* (34), 5115–5119.

[58] Davis, A.; C. Bush, R.; C. Harvey, J.; F. Foley, M., P-95: Fresnel lenses in rear projection displays. *Sid Symposium Digest of Technical Papers* **2001**, *32*, 934– 937.

[59] Ferstl, M.; Frisch, A.-M., Static and dynamic fresnel zone lenses for optical interconnections. *Journal of Modern Optics* **1996**, *43* (7), 1451–1462.

[60] Millán, M. S.; Otón, J.; Pérez-Cabré, E., Dynamic compensation of chromatic aberration in a programmable diffractive lens. *Optics Express* **2006**, *14* (20), 9103–9112.

[61] Arieli, Y.; Ozeri, S.; Eisenberg, N.; Noach, S., Design of a diffractive optical element for wide spectral bandwidth. *Optics Letters* **1998**, *23* (11), 823–824.

[62] Márquez, A.; Iemmi, C.; Campos, J.; Yzuel, M. J., Achromatic diffractive lens written onto a liquid crystal display. *Optics Letters* **2006**, *31* (3), 392–394.

[63] Millán, M. S.; Otón, J.; Pérez-Cabré, E., Chromatic compensation of programmable fresnel lenses. *Optics Express* **2006**, *14* (13), 6226–6242.

[64] Jiang, Z. H.; Yun, S.; Lin, L.; Bossard, J. A.; Werner, D. H. a., Tailoring dispersion for broadband low-loss optical metamaterials using deep-subwavelength inclusions. *Scientific Reports* **2013**, *3* (3), 1571.

[65] Farmahini-Farahani, M.; Mosallaei, H., Birefringent reflectarray metasurface for beam engineering in infrared. *Optics Letters* **2013**, *38* (4), 462–464.

[66] Khorasaninejad, M.; Chen, W. T.; Oh, J.; Capasso, F., Super-dispersive off-axis meta-lenses for compact high resolution spectroscopy. *Nano Letters* **2016**, *16* (6), 3732–3737. PMID: 27119987.

[67] Aieta, F.; Kats, M. A.; Genevet, P.; Capasso, F., Multiwavelength achromatic metasurfaces by dispersive phase compensation. *Science* **2015**, *347* (6228), 1342–1345.

[68] García, J. A. M.; Mena, A. J. G., Optimal distributed generation location and size using a modified teaching–learning based optimization algorithm. *International Journal of Electrical Power and Energy Systems* **2013**, *50*, 65 – 75.

[69] Ishii, S.; Shalaev, V. M.; Kildishev, A. V., Holey-metal lenses: Sieving single modes with proper phases. *Nano Letters* **2013**, *13* (1), 159–163.

[70] Wu, D.; Wu, S.-Z.; Niu, L.-G.; Chen, Q.-D.; Wang, R.; Song, J.-F.; Fang, H.-H.; Sun, H.-B., High numerical aperture microlens arrays of close packing. *Applied Physics Letters* **2010**, *97* (3), 031109.

[71] Myers, B. D.; Dravid, V. P., Variable pressure electron beam lithography (vp-ebl): A new tool for direct patterning of nanometer-scale features on substrates with low electrical conductivity. *Nano Letters* **2006**, *6* (5), 963–968.

[72] Muskens, O. L.; Bachelier, G.; Fatti, N. D.; Vallée, F.; Brioude, A.; Jiang, X.; Pileni, M.-P., Quantitative absorption spectroscopy of a single gold nanorod. *The Journal of Physical Chemistry C* **2008**, *112* (24), 8917–8921.

[73] Knight, M. W.; King, N. S.; Liu, L.; Everitt, H. O.; Nordlander, P.; Halas, N. J., Aluminum for plasmonics. *ACS Nano* **2014**, *8* (1), 834–840. PMID: 24274662.

[74] Johnson, P. B.; Christy, R. W., Optical constants of the noble metals. *Physical Review B* **1972**, *6*, 4370–4379.

[75] Pahlevaninezhad, H.; Khorasaninejad, M.; Huang, Y.-W.; Shi, Z.; Hariri, L. P.; Adams, D. C.; Ding, V.; Zhu, A.; Qiu, C.-W.; Capasso, F.; Suter, M. J., Nano-optic endoscope for high-resolution optical coherence tomography in vivo. *Nature Photonics* **2018**, *12*, 540–547.

[76] Groever, B.; Chen, W. T.; Capasso, F., Meta-lens doublet in the visible region. *Nano Letters* **2017**, *17* (8), 4902–4907. PMID: 28661676.

[77] Yang, W.; eun Kang Miller, J.; Carrillo-Reid, L.; Pnevmatikakis, E.; Paninski, L.; Yuste, R.; Peterka, D., Simultaneous multi-plane imaging of neural circuits. *Neuron* **2016**, *89* (2), 269 – 284.

[78] Abrahamsson, S.; Chen, J.; Hajj, B.; Stallinga, S.; Katsov, A. Y.; Wisniewski, J.; Mizuguchi, G.; Soule, P.; Mueller, F.; Darzacq, C. D.; Darzacq, X.; Wu, C.; Bargmann, C. I.; Agard, D. A.; Dahan, M.; Gustafsson, M. G. L., Fast multicolor 3d imaging using aberration-corrected multifocus microscopy. *Nature Methods* **2012**, *10*, 60–63.

[79] Dalgarno, P. A.; Dalgarno, H. I. C.; Putoud, A.; Lambert, R.; Paterson, L.; Logan, D. C.; Towers, D. P.; Warburton, R. J.; Greenaway, A. H., Multiplane imaging and three dimensional nanoscale particle tracking in biological microscopy. *Optics Express* **2010**, *18* (2), 877–884.

[80] Ee, H.-S.; Agarwal, R., Tunable metasurface and flat optical zoom lens on a stretchable substrate. *Nano Letters* **2016**, *16* (4), 2818–2823. PMID: 26986191.

[81] Kamali, S. M.; Arbabi, E.; Arbabi, A.; Horie, Y.; Faraon, A., Highly tunable elastic dielectric metasurface lenses. *Laser & Photonics Reviews* **2016**, *10* (6), 1002–1008.

[82] She, A.; Zhang, S.; Shian, S.; Clarke, D. R.; Capasso, F., Adaptive metalenses with simultaneous electrical control of focal length, astigmatism, and shift. *Science Advances* **2018**, *4* (2).

[83] Zou, S.; Janel, N.; Schatz, G. C., Silver nanoparticle array structures that produce remarkably narrow plasmon lineshapes. *The Journal of Chemical Physics* **2004**, *120* (23), 10871–10875.

[84] Kravets, V. G.; Schedin, F.; Grigorenko, A. N., Extremely narrow plasmon resonances based on diffraction coupling of localized plasmons in arrays of metallic nanoparticles. *Physical Review Letters* **2008**, *101*, 087403.

[85] Auguié, B.; Barnes, W. L., Collective resonances in gold nanoparticle arrays. *Physical Review Letters* **2008**, *101*, 143902.

[86] Kravets, V. G.; Schedin, F.; Jalil, R.; Britnell, L.; Gorbachev, R. V.; Ansell, D.; Thackray, B.; Novoselov, K. S.; Geim, A. K.; Kabashin, A. V.; Kabashin, A. V., Singular phase nano-optics in plasmonic metamaterials for label-free single-molecule detection. *Nature Materials* **2013**, *12*, 304—-309.

[87] Schokker, A. H.; Koenderink, A. F., Statistics of randomized plasmonic lattice lasers. *ACS Photonics* **2015**, *2* (9), 1289–1297.

[88] Zhou, W.; Odom, T. W., Tunable subradiant lattice plasmons by out-of-plane dipolar interactions. *Nature Nanotechnology* **2011**, *6*, 423—-427.

[89] Khlopin, D.; Laux, F.; Wardley, W. P.; Martin, J.; Wurtz, G. A.; Plain, J.; Bonod, N.; Zayats, A. V.; Dickson, W.; Gérard, D., Lattice modes and plasmonic linewidth engineering in gold and aluminum nanoparticle arrays. *J. Opt. Soc. Am. B* **2017**, *34* (3), 691–700.

[90] Choo, P.; Hryn, A. J.; Culver, K. S.; Bhowmik, D.; Hu, J.; Odom, T. W., Wavelength-dependent differential interference contrast inversion of anisotropic gold nanoparticles. *The Journal of Physical Chemistry C* **2018**, *122* (47), 27024–27031.

[91] Yang, A.; Hryn, A. J.; Bourgeois, M. R.; Lee, W.-K.; Hu, J.; Schatz, G. C.; Odom, T. W., Programmable and reversible plasmon mode engineering. *Proceedings of the National Academy of Sciences* **2016**, *113* (50), 14201–14206.

[92] Huang, Y. Y.; Zhou, W.; Hsia, K. J.; Menard, E.; Park, J.-U.; Rogers, J. A.; Alleyne, A. G., Stamp collapse in soft lithography. *Langmuir* **2005**, *21* (17), 8058–8068. PMID: 16089420.

[93] Huntington, M. D.; Odom, T. W., A portable, benchtop photolithography system based on a solid-state light source. *Small 7* (22), 3144–3147.

APPENDIX A

Vita

HU, JINGTIAN

(217) 979-9186 • jingtianhu@gmail.com

EDUCATION

Northwestern University — GPA: 3.80
Ph.D. in Material Science and Engineering — *2019 (expected)*

University of Illinois at Urbana-Champaign — GPA: 3.95
Bachelor of Science in Material Science and Engineering — *2013*

RESEARCH EXPERIENCE

Graduate research assistant: the Odom group, Northwestern University (2013-present)

- Computational design plasmonic lattice lenses for multi-wavelength achromatic focusing
- Evolutionary design and prototyping of single-crystalline titanium nitride nanostructures for miniaturized optical devices
- Design of reconfigurable metasurfaces in coupled plasmonic nanoparticle arrays

Undergraduate research assistant: Ferguson lab, University of Illinois at Urbana-Champaign (2012)

- "Global graph matching by nonlinear manifold learning"

Undergraduate research assistant: James Economy research group, University of Illinois at Urbana-Champaign (2010-2011)

- "Designing ion-exchange polymeric adsorption materials for water purification"

RESEARCH INTEREST

Ultrathin achromatic optical components; light-tunable catalytic metal nanoparticle metal-organic framework; computational design of nanophotonic structures using unconventional plasmonic materials; reconfigurable optical metasurfaces; optoelectronic devices in harsh environment; dynamic nonlinear optical responses; deep learning analysis of plasmonic nanoparticle probes

CONFERENCE PRESENTATIONS

Evolutionary Design and Prototyping of Crystalline Titanium Nitride Metasurfaces, *Materials Research Society (MRS)*, oral 2016, November 27-December 01, Boston, USA.

Achromatic Plasmonic Lattice Optics by Evolutionary Design, *Materials Research Society (MRS)*, oral 2016, November 28-December 02, Boston, USA.

PUBLICATIONS

"Lattice-Resonance Metalenses for Fully Reconfigurable Imaging" **J. Hu**, D. Wang, D. Bhowmik, T. Liu, S. Deng, M.P. Knudson, X. Ao, and T.W. Odom (Submitted)

"Spatially Defined Molecular Emitters Coupled to Plasmonic Nanoparticles " J. Liu, W. Wang, D. Wang, **J. Hu**, W. Ding, R.D. Schaller, G.C. Schatz and T.W. Odom, *PNAS* (In revision)

"Wavelength-Dependent Differential Interference Contrast Inversion of Anisotropic Gold Nanoparticles" P. Choo, A.J. Hryn, K.S. Culver, D. Bhowmik, **J. Hu**, and T.W. Odom, *J. Phys. Chem. C* **2018**, 122, 27024-27031

"Monolithic Polymer Nanoridges with Programmable Wetting Transitions" W-K. Lee, W-B. Jung, D. Rhee, **J. Hu**, Y-A.L. Lee, C. Jacobson, H-T. Jung, and T.W. Odom, *Adv. Mater.* **2018**, 30, 1706657

"Evolutionary Design and Prototyping of Single Crystalline Titanium Nitride Lattice Optics" **J. Hu**, X. Ren, A. N. Reed, T. Reese, D. Rhee, B. Howe, L. J. Lauhon, A. M. Urbas, and T. W. Odom, *ACS Photonics* **2017**, 4, 606–612

"Programmable and reversible plasmon mode engineering" A. Yang, A. J. Hryn, M. R. Bourgeois, W. K. Lee, **J. Hu**, G. C. Schatz and T.W. Odom, *Proc. Natl. Acad. Sci.* **2016**, 113, 14201–14206

"Plasmonic Lattice Lenses for Multiwavelength Achromatic Focusing" **J. Hu**, C. H. Liu, X. Ren, L. J. Lauhon and T.W. Odom, *ACS Nano* **2016**, 10, 10275–10282

"Global graph matching by nonlinear manifold learning" **J. Hu** and A.L. Ferguson, *Intell. Data Anal.* **2016**, 20, 637-654

"Interactions of Cr(VI) with hybrid anion exchange/porous carbon fibers in aqueous solution at neutral pH" W. Zheng, **J. Hu,** E. Diesel, Z. Wang, Z. Zheng, C. Ba, J. Langer and J. Economy, *Chem. Eng. J.* **2016**, 287, 54-61

"Activated carbon fiber composites for gas phase ammonia adsorption" W. Zheng, **J. Hu,** S. Rappeport, Z. Zheng, Z. Wang, Z. Han, J. Langer and J. Economy, *Microporous and Mesoporous Mater.* **2016**, 234, 146-154

"Controlled Three-Dimensional Hierarchical Structuring by Memory-Based, Sequential Wrinkling" W. K. Lee, C. J. Engel, M. D. Huntington, **J. Hu,** and T. W. Odom, *Nano Lett.* **2015**, 15, 5624–5629

"Synthesis of porous carbon fibers with strong anion exchange functional groups**"** W. Zheng, **J. Hu,** Z. Han, Z. Wang, Z. Zheng, J. Langer and J. Economy**,** *Chem. Commun.* **2015**, 51, 9853-9856

PRESS RELEASES

“Unconventional TiN nanohole arrays bring new dynamic to plasmonic metamaterials”, *MRS Bulletin News*, March 3rd, 2017

“Computational and patterning approaches to realize metasurfaces in novel plasmonic materials”, *Nanowerk News*, January 27th, 2017

“Ultra-thin achromatic lenses optimized by an evolutionary algorithm”, *Nanowerk News*, October 28th, 2016

HONORS AND LEADERSHIP

Outstanding Researchers of International Institue for Nanotechnology	Fall 2017
Predictive Science & Engineering Design Fellowship	Spring 2016
Hierarchical Materials Cluster Program Fellowship	Winter 2015
Lucille and Charles Wert Scholars	Spring 2013
John Menees Library Award	Spring 2011
Alfred W. Allen Awards	2010- 2012

TECHNICAL SKILLS

Microfabrication and nanofabrication: focused ion beam milling, photolithography, electron beam lithography, solvent-assisted nanoscale embossing, wet etching, reactive-ion etching, template stripping, and thermal evaporation

Microscopy: scanning electron microscopy, environmental scanning electron microscopy, atomic force microscopy, and scanning confocal microscopy

Data Analysis & Processing: MATLAB, Microsoft Excel, Adobe Photoshop and Illustrator

Programming Languages: C++, Python, Java, C, and Fortran

3D Modeling & Data Visualization: Blender and Paraview

Computational Methods: PyTorch for deep learning, Finite-Difference Time-Domain (FDTD) simulations for optical simulation, Abaqus and Deal.II finite element for mechanical simulation, and genetic algorithm for optimizations

TEACHING EXPERIENCE

Teaching assistant for MSE 304 (University of Illinois at Urbana-Champaign)	Spring 2013
Teaching assistant for MSE 404 (Northwestern University)	Winter 2017
Teaching assistant for MSE 351-2 (Northwestern University)	Spring 2017

REFERENCE CONTACTS

Prof. Teri W. Odom
Charles E. and Emma H. Morrison Professor of Chemistry
Chair, Department of Chemistry and
Professor of Materials Science and Engineering,
Northwestern University
Executive Editor, ACS Photonics
Email: todom@northwestern.edu
Phone: 847-491-7674

Prof. Wei Chen
Wilson-Cook Professor in Engineering Design
Department of Mechanical Engineering,
Northwestern University
Email: weichen@northwestern.edu
Phone: 847-491-7019

Prof. Andrew L. Ferguson
Institute of Molecular Engineering,
University of Chicago
Email: andrewferguson@uchicago.edu
Phone: 217-300-2354

Dr. Weihua Zheng
Vice Present of Engineering, Serionix, Inc.,
60 Hazelwood Drive, Champaign, IL 61820
Email: wzheng@serionix.com
Phone: 217-819-0349